X-692-71-95
PREPRINT

HYDROMAGNETIC WAVES AND DISCONTINUITIES IN THE SOLAR WIND

L. F. BURLAGA

MARCH 1971

GODDARD SPACE FLIGHT CENTER
GREENBELT, MARYLAND

X-692-71-95
Preprint

HYDROMAGNETIC WAVES AND DISCONTINUITIES IN THE SOLAR WIND

By

L. F. Burlaga

March 1971

Goddard Space Flight Center

Greenbelt, Maryland

CONTENTS

CONTENTS (Continued)

HYDROMAGNETIC WAVES AND DISCONTINUITIES IN THE SOLAR WIND

I. Introduction

Studies of the interplanetary medium have produced results of astrophysical and geophysical significance. During the past ten years it has also become possible to treat the interplanetary medium as a laboratory sample of a cosmic plasma. One of the major results of these experimental investigations is the demonstration that hydromagnetic theory is applicable to this tenuous plasma. Of course, fluid processes represent only a subset of the great wealth of phenomena occurring and one must remember that the applicability of hydromagnetic theory is limited. Moreover, these limitations are presently the subject of great interest, and the transport parameters remain to be determined by the development of an appropriate kinetic theory. But the applicability of hydromagnetic theory to the solar wind is very extensive nevertheless. While the current trend in the literature emphasizes the limitations of the fluid theory, this review emphasizes its positive results.

Various modifications of the hydromagnetic theory for a single species fluid having an isotropic pressure have been made for specific solar wind problems. We shall develop a general form of hydromagnetic theory appropriate for the solar wind, and we shall show how the various special theoretical results can

be unified and systematically derived from this general formulation. We shall also show how solar wind plasma and magnetic field observations support and can be organized by this theory. The emphasis is thus on the basic theoretical and experimental results and relations between them. For this reason, complex, non-reproducible phenomena and descriptive results very specific to the solar wind are not discussed. Likewise, theoretical work which has no present connection with observations is not reviewed.

II. Summary of Solar Wind Properties.

Since there exist good recent reviews of the observation material, (Axford, 1968; Hundhausen, 1968, 1970; Ogilvie, 1970; Scarf, 1970; Vasyliunas, 1971) we shall not go into great detail in the description of specific experiments and their results. The aim of this section is to provide the reader with a condensed summary of those properties presently established together with the necessary references to the papers which give the detailed information not presented here.

An exhaustive review of experimental methods, drawing attention to the important conversion of engineering quantities (count rates, currents, etc.) to physical quantities (temperature, densities, etc.) characteristic of the particle distribution functions has been published by Vasyliunas (1971). As he points out, a basic task of particle experiments is the determination of the properties of the plasma by the enumeration of the distribution function by counting particles

present in various parts of velocity and configuration space. The results, though always an approximation, represent the essential features of $f(r, v, t)$, defined such that $f\,dr\,dv$ is the probability of finding a particle in $dr\,dv$ at time t.

In the fluid description of the plasma, it is considered as a conducting fluid, whose motion and properties (for example transport properties) are modified by the presence of electric and magnetic fields. The state of this fluid at a given time is specified by the parameters, density, bulk speed etc. The evaluation of these quantities in terms of the distribution function is covered in many textbooks (for example Boyd and Sanderson, 1969), where it is shown that

$$n(r, t) = \int f(r, v, t)\, dv \tag{2.1}$$

$$u(r, t) = \frac{1}{n} \int v\, f\, dv \tag{2.2}$$

$$\underset{\approx}{T}(\underset{\sim}{r}, t) = \frac{\underset{\approx}{P}}{3 n k} \tag{2.3}$$

where $\underset{\approx}{P}$ is the pressure tensor, defined in terms of the second velocity moment of f.

We now discuss the observed properties of the plasma particles in terms of these quantities. For this purpose it is important to introduce the idea of scales

of length (or time). The idea of "macroscale," "mesoscale" and "microscale," introduced by Burlaga and Ness (1968) and discussed further by Burlaga (1969) has been successfully used to classify and interpret data, a length being convertible to the corresponding time by dividing by a representative bulk speed. The mesoscale deals with lengths of $\lesssim$1AU and the microscale with lengths of $\lesssim$0.01 AU respectively (see Figure 1). It is clear that mesoscale changes in the fluid parameters are indicative of changes in the flow field on a large scale. Microscale changes reflect the passage past a given observatory of waves, discontinuities or rapid changes. Examples of such effects will be discussed later at length.

Observations of fluid quantities on the macroscale show that while there is considerable variability, the bulk speed is seldom below 300 km sec^{-1} and the low speeds are between 300 and 350 km sec^{-1}. At these times the temperature is about 3×10^4 °K, so the flow is supersonic, with Mach number of order ten. For these conditions, referred to as the "quiet solar wind" and usually used to compare with theoretical predictions at 1AU, the density is $\approx$ 8 cm^{-3}. At other heliocentric distances, between say 0.25 AU and 5-10 AU, the flow speed is predicted to remain closely constant, the density decreases as $1/r^2$, and the temperature decreases as r increases at a rate whose details depend upon the heat conductivity of the plasma. It is expected to be somewhat slower than the adiabatic rate. Relatively little observational material has been presented about conditions at heliocentric distances other than 1 AU.

The proton temperature is anisotropic about the direction of the interplanetary magnetic field, $T_{\parallel}/T_{\perp}$ being 2:1, which is less than would be expected from the Coulomb collision length in the medium alone.

The electron density is such as to preserve charge neutrality, and electrons convected at the same bulk speed as the protons. The measured electron temperature is essentially constant at a value of 1 to 1.5 $\times 10^5$°K, with an anisotropy about the field direction of $\lesssim 1.2$. This means that the electron distribution function is quasi-stationary in time, and that the flow of the electron gas is subsonic, since the electron thermal speed is several thousand km/sec.

At the present time the density, temperature and its anisotropy, the bulk speed and heat flux have all been established for both protons and electrons at 1AU. These values for the quiet solar wind as defined above are given in Table I. The values of some derived quantities are also given.

The value of $\beta \equiv nk(T_i + T_e)/(B^2/8\pi)$, in the solar wind at IAU is typically close to unity. Other species of particles exist in the solar wind. Extensive observations show a highly variable admixture of helium. If one disregards the short periods when the proportion of helium to hydrogen exceeds 10%, which seem to be associated with solar activity, we see that one can generally neglect the presence of this second species. The ratio of the helium thermal energy density to that of the

Table I

Observed and Calculated Properties in the Quiet Solar Wind

Observed	
Flow speed	320 km sec^{-1}
Proton and Electron density	8 cm^{-3}
Proton Temperature	4×10^4 °K
Proton Thermal Anisotropy Ratio	1.9
Electron Temperature	$1\text{-}1.5 \times 10^5$ °K
Electron Thermal Anisotropy Ratio	1.1
Magnetic Field	5γ
Proportion of Helium (n_α/n_p)	0.05
Heat Conduction Flux (total)	0.01 erg cm^{-2} sec^{-1}
Calculated	
Proton flux	2×10^8 cm^{-2} sec^{-1}
Kinetic Energy Flux	0.22 erg cm^{-2} sec^{-1}
Kinetic Energy density	7×10^{-10} erg cm^{-3}
Proton Thermal Energy Density	6×10^{-11} erg cm^{-3}
Electron Thermal Energy Density	1.5×10^{-10} erg cm^{-3}
Magnetic Field Energy Density	10^{-10} erg cm^{-3}
B_i	~0.3
B_e	~1.0
Variability at 1 AU	
Flow Speed	275-800 km/sec^{-1}
Density	~1.0 to ~50 cm^{-3}
Proton Temperature	$< 3 \times 10^4$ to 5×10^5 °K
Proton Thermal Anisotropy Ratio	1 to 3.0
Electron Temperature	1 to 2×10^5 °K
Proportion of He (n_α/n_p)	0.01 to 0.20
Helium/Hydrogen Bulk Speeds	< 5%

hydrogen is 0.2; that of the two kinetic energy fluxes is 0.2, but since the bulk speeds seem always to be equal within the accuracy of observation (a few percent) the principal effect of the helium is to increase the fluid particle density and pressure. The possible effects of the admixture of a second species on the stability of the plasma seem not to be important in the fluid approximation, (Fredericks and Scarf, 1965). The other species recently detected in the solar wind at quiet times are present in such small amounts that their effect is probably negligible.

(Bame et. al., 1970). We are dealing with a multi-component, anisotropic, collisionless plasma, with supersonic protons and subsonic electrons, which has $\beta \approx 1$.

III. Basic Equations

A. Discussion. As shown above, the general equations for fluid motions in the solar wind must include the magnetic field, the particle anisotropies, and the different species. There are 5 transport equations (conservation of mass (1), momentum (3), and energy (1)) for each species and those are coupled with one another and with the equations for the current and magnetic field. Because of the complexity of this system, it has not been studied in its general form. Two approximations are commonly used: (1) a single fluid approximation, obtained by averaging over particle species, which is valid for an anisotropic, hydromagnetic fluid; and a 2-fluid model for an isotropic fluid with $B = 0$. The 2-fluid model was developed for investigations of macroscale solar wind properties. The results of this paper are related to the single fluid approximation.

B. Single-Fluid Approximation

1. Conservation of mass. Averaging the mass conservation equations for each species gives

$$\frac{\partial \rho}{\partial t} + \nabla \cdot (\rho v) = 0, \tag{3.1}$$

where

$$\rho \equiv \sum m_i n_i \tag{3.2}$$

and

$$v \equiv \frac{1}{\rho} \sum m_i n_i u_i; \tag{3.3}$$

here m_i is the particle mass, n_i is the density of particles of species i given by (2.1), and u_i is the average speed of species i given by (2.2).

2. Conservation of momentum. For the solar wind, the momentum equation is

$$\frac{\partial}{\partial t} (\rho v) + \nabla \cdot (\underset{\approx}{P} + \underset{\approx}{P}_{em} + \rho v v) = 0 \tag{3.4}$$

where $\underset{\approx}{P}_{em}$ is Maxwell's stress tensor,

$$\underset{\approx}{P}_{em} = \delta_{ij} \frac{B^2}{8\pi} - \frac{B_i B_j}{4\pi} \tag{3.5}$$

and $\underset{\approx}{P}$ is the mechanical stress tensor summed over particle species, which can be written in the form

$$\underset{\approx}{P} = \sum_k \left[(p_{k\parallel} - p_{k\perp}) \frac{B_i B_j}{B^2} + p_{k\perp} \delta_{ij} \right], \tag{3.6}$$

where $p_{k\perp}$ is the pressure of the kth species perpendicular to $\underset{\sim}{B}$,

$$p_{k\perp} = n_k m_k \int w_{k\perp} w_{k\perp} f \, dv \tag{3.7}$$

and $p_{k\parallel}$ is the pressure parallel to $\underset{\sim}{B}$,

$$p_{k\parallel} = n_k m_k \int w_{k\parallel} w_{k\parallel} f \, dv; \tag{3.8}$$

where

$$w_k \equiv v_k - u_k \tag{3.9}$$

One might add a viscosity term to $\underset{\approx}{P}$, but it seems to be negligible for macro-scale processes in the solar wind. Putting (3.5) and (3.6) into (3.4) gives

$$\frac{\partial (\rho v)}{\partial t} + \nabla \cdot \left[\rho v v + \underset{\approx}{I} \left(\sum p_{k\perp} + \frac{B^2}{8\pi} \right) - \frac{B B}{4\pi} \xi \right] = 0 \tag{3.10}$$

where

$$\xi \equiv 1 - \frac{\sum_k (p_{k\parallel} - p_{k\perp})}{(B^2/4\pi)} \tag{3.11}$$

Noting that

$$\frac{\partial (\rho v)}{\partial t} + \nabla \cdot (\rho v v) = \rho \frac{dv}{dt}$$

and using the condition $\nabla \cdot B = 0$, one gets from (3.10)

$$\rho \frac{d v}{d t} = - \nabla \left(\sum_k p_{k\perp} + \frac{B^2}{8\pi} \right) - \frac{(B \cdot \nabla) B}{4\pi} \xi, \qquad (3.12)$$

if $\xi \approx$ constant. This equation with $\xi = 1$ was first derived by Parker (1957) from particle orbit theory. Clearly, ξ is a measure of the anisotropy, being 1 for an isotropic plasma and <1 for an anisotropic plasma with $p_{\parallel} > p_{\perp}$. Note that the anisotropy enters only in the $(B \cdot \nabla) B$ term. Since $(B \cdot \nabla) B$ is proportional to the curvature of the field lines, it is clear that the anisotropy directly affects the motions if and only if the field lines bend.

Equations (3.10) and (3.12) are fluid equations, and they imply a collective interaction of the fluid particles. For motions normal to $\underset{\sim}{B}$ this is caused by the magnetic field; collisions are not necessary. This was shown by Burgers (1960), Chandrasekhar (1960), and Whang (1970), who obtained (3.10) for $v_{\perp}$ for a collisionless plasma. For motions along B there must be collective plasma interactions if the motions are to be fluid-like. These motions are not yet fully understood. It is possible that on some scales one should use a kinetic equation for motions along $\underset{\sim}{B}$, rather than (3.10).

3. Frozen-Field Condition. Assuming infinite electrical conductivity and neglecting the effects at ion and electron inertia, one has $E = -v \times B/c$, where c is the speed of light. In this case v and B are related by the equation

$$\frac{\partial B}{\partial t} = \nabla \times (v \times B) \qquad (3.13)$$

This is essentially the same as a form of the Beltrami equation for vorticity in a non-viscous, incompressible medium (Serrin, 1959, page 151), and it implies that the lines of force (or vortex lines in the case of the Beltrami equation) are "frozen" to the fluid. It was first discussed by Alfven (1943).

4. Closure. For many purposes, it is not necessary to consider higher moments of the distribution function. However, the conservation of mass and momentum equations ((3.1) and (3.12)) and the frozen-field equation, (3.13), give only 7 equations whereas there are 9 unknowns (v, B, ρ, $p_\perp$ and $p_\parallel$). Thus, 2 additional equations are needed to obtain a closed set of equations describing the plasma motions.

For macroscale studies, it is customary to assume isotropy ($\xi = 1$), which reduces the number of variables to 8. Then only one additional equation is needed, and it is customary to use the adiabatic approximation $p = A(S)\,\gamma$ which gives a relation between the pressure and density which is valid for constant entropy, S. In the kinetic theory of gases it is shown that $\gamma = (N + 2)/N$ where N is the number of degrees of freedom. The application of this equation to the solar wind has no theoretical or experimental justification, but it is obviously mathematically convenient.

Another means of closing the equations, which is sometime applied to the solar wind when discussing problems involving anisotropy, is the method of Chew, Goldberger and Low (1956). Their closure equations are

$$\frac{d}{dt}\left(\frac{p_\perp}{\rho B}\right) = 0 \tag{3.14}$$

and

$$\frac{d}{dt}\left(\frac{p_\parallel B^2}{\rho^3}\right) = 0 \tag{3.15}$$

These equations assume no heat flux, but can be extended for a constant heat flux. The CGL closure equations were derived on the assumption that $\beta \equiv n k T / (B^2/8\pi) \ll 1$. This assumption is not applicable to the solar wind.

We shall close the system with the following equations

$$p_{k\perp} = A_{k\perp} \rho_k^{\gamma_\perp} \tag{3.16}$$

$$p_{k\parallel} = A_{k\parallel} \rho_k^{\gamma_\parallel} \tag{3.17}$$

The appropriate values for $\gamma_\perp$ and $\gamma_\parallel$ are unknown. An obvious choice for microscale processes where the field is relatively orderly is $\gamma_\perp = 2$ (because there are 2 degrees of freedom normal to B) and $\gamma_\parallel = 3$ (because there is obviously just one degree of freedom along B). We cannot exclude the possibility that compressions along B are isothermal since the conductivity along B is high, especially for electrons ($p \propto \rho$); in this case $\gamma_\parallel = 1$ rather than 3. One should also consider the possibility that γ depends on the scale, since on a large scale the field is more disordered (perhaps turbulent) than on a small scale. These are problems for future work.

5. Energy Equation. The forms of energy to be considered to drive the microscale processes in the solar wind are the kinetic or streaming energy, the parallel and perpendicular thermal energy and the magnetic energy. Let

$$\epsilon = \frac{p_{\parallel}}{2} + p_{\perp}. \tag{3.18}$$

The energy flux is

$$F = \left(\frac{\rho v^2}{2} + \epsilon\right) v + \underset{\approx}{P} : v + S + q \tag{3.19}$$

where S is the Poynting flux

$$S = -\frac{(v \times B) \times B}{4\pi} c \tag{3.20}$$

and q is the heat flux

$$q \equiv \sum \frac{n_i M_i}{2} \int d v \, w_i^2 \, w_i \, f. \tag{3.21}$$

The heat flux, q, has been neglected in most of the dynamical studies of microscale processes, but this assumption has not been justified experimentally and there are recent studies which indicate that electron heat fluxes may be very significant under some circumstances (Burlaga et al., 1970, Hundhausen and Montgomery, 1970).

The conservation of energy is expressed by the equation

$$\frac{\partial \epsilon}{\partial t} + \nabla \cdot \underset{\sim}{F} = 0 \tag{3.22}$$

6. Remarks on Velocities. It is important to distinguish the various velocities which are used above. The basic equations involve the center of mass velocity, v, which is a momentum average over the particle species, viz., as $\rho v = \Sigma n_i m_i u_i$. Here ρ is the average density, $\rho = \Sigma n_i m_i$, and u_i is the average flow velocity of the ith species,

$$u_i = \frac{n_i}{n} \int v_i \, f \, dv_i \tag{3.23}$$

where v_i is a point in the velocity space of the ith species. The momentum tensor, given by (3.6), and the heat conduction vector, given by (3.21), involve the thermal velocity measured relative to the center of mass velocity, i.e., $w_i = v_i - v$. This presents a problem since in practice one would usually determine $\underset{\sim}{P}$ and q for each species separated, by integrating over the thermal speed $w_i' = v_i - u_i$, measured relative to u_i. Since particles of all species are frozen to the lines of force, they should all move normal to B with the same velocity, i.e., $v_{\perp_i} = v_\perp$, but there seems to be no reason why different species could not move parallel to B with different speeds. However, observations (Ogilive et al., (1968); Robbins et al., 1970) indicates that in the solar wind the α's and protons have essentially the same mean speed (within 10 km/sec), and the

nean speed of the electrons does not significantly effect v because of the small electron to proton mass ratio, so for most purposes we can set $v \approx u_i$ for solar wind particles, in which case $w_i' \approx w_i$.

V. WAVES

A. Introduction. Although the theory for hydromagnetic waves in an isotropic fluid is given in many texts, the theory for an anisotropic, multifluid, collisionless plasma is not well known, and differs from the isotropic theory in some important respects. Since the anisotropic theory is the relevant one for the solar wind, we develop it in some detail. We shall consider a number of special cases which show the basic physical properties of the waves. The general situation is discussed briefly at the end of this section.

One can distinguish 3 classes of waves:

$$1. \quad v_{\parallel} \neq 0, \quad v_{\perp} = 0 \tag{4.1}$$

$$2. \quad v_{\parallel} = 0, \quad v_{\perp} \neq 0 \tag{4.2}$$

$$3. \quad v_{\parallel} \neq 0, \quad v_{\perp} \neq 0 \tag{4.3}$$

Here, and in what follows in this section, v is the perturbation velocity due to the wave.

B. Waves with $v_{\parallel} \neq 0$, $v_{\perp} = 0$. In this case, the oscillations are only along the magnetic field. Equation (3.13) shows that $\partial B / \partial t = 0$ for such waves, i.e.,

they involve no variations B. Since B = constant and $p_\perp$ is also constant, the linearized form of (3.10) gives

$$\rho \frac{\partial v_\parallel}{\partial t} = - \nabla_\parallel \left(\sum p_{k\parallel} \right) = \sum c_k^2 \nabla_\parallel \rho_k \tag{4.4}$$

where $c_\parallel^2 \equiv \partial p_{k\parallel} / \partial_{\rho k}$ is the speed of sound of the kth species. If $p_k = A \rho_k \gamma$, then $c_k^2 = \gamma_k T_k / m_k$. Let

$$c_\parallel^2 \equiv \rho^{-1} \sum_k (c_{k\parallel}^2 \rho_k). \tag{4.5}$$

For a plasma consisting of electrons and protons,

$$c_\parallel^2 = \frac{\gamma_+ T_\parallel^+ + \gamma_- T_\parallel^-}{m_+}. \tag{4.6}$$

If $c_\parallel$ is a constant, then (4.4) and the continuity equation give

$$\frac{\partial^2 v_\parallel}{\partial t^2} - c_\parallel^2 \nabla_\parallel^2 v_\parallel = 0 \tag{4.7}$$

This is an equation for sound waves propagating along $\underset{\sim}{B}$ with speed $c_\parallel^2$. The wave is illustrated in Figure 2a.

The existence of acoustic waves in a collisionless plasma is somewhat paradoxical. However, such waves (ion acoustic waves) are predicted by collisionless theory and are expected to propagate with little attenuation when $T_e >> T_i$. The restoring force is provided by an electrostatic effect.

Such waves have not been identified in the solar wind, and their coupling with other modes (assuming ion acoustic waves do propagate) is poorly understood. Such waves do not appear in Whang's model for flow past the moon since he assumes that particle motions along $\underset{\sim}{B}$ are governed by orbit theory rather than by the flow equations.

C. Waves with $v_\perp = 0$, $v_\parallel \neq 0$. The equation of motion (3.12) can be written

$$\rho \frac{d v}{d t} = G + M \tag{4.8}$$

where

$$G \equiv - \nabla \left(\sum P_{kl} + \frac{B^2}{8 \pi} \right) \tag{4.9}$$

and

$$M = - \frac{\xi}{4 \pi} (B \cdot \nabla) B. \tag{4.10}$$

Clearly, G is due to gradients in the total perpendicular pressure. M is caused by the tension in the magnetic field lines, which is non-zero if and only if the field lines are curved. Note that the anisotropy appears only in M. We can distinguish 3 cases, shown in Table II. (Bear in mind that we are assuming $v_\parallel = 0$. Also note that we are using the terms magnetoacoustic and fast wave in a limited sense.) Now, consider each of these cases in turn.

Table II

	G	M
Alfven wave	0	$\neq 0$
Magneto acoustic wave	$\neq 0$	0
Magneto "fast wave"	$\neq 0$	$\neq 0$

1. Alfren wave ($G = 0$, $M \neq 0$; $v_{\parallel} = 0$). In this case there are no pressure gradients so n, T, and $\underset{\sim}{B}$ are constant, but the magnetic field lines oscillate like waves on a string. Let us choose a coordinate system such that $\hat{z}$ is along $\hat{k}$ and take the perturbations along $\hat{y}$: $\delta B \equiv b(z)\,\hat{y}$, $\delta \underset{\sim}{v} \equiv v(z)\,y$ (see Figure 3). Consider the case when B is parallel to $\hat{k}$. The force equation (3.12) gives for a homogeneous plasma

$$\rho \frac{\partial v_{\perp}}{\partial t} = \left(\xi \frac{B}{4\pi}\right) \frac{\partial b}{\partial z}. \tag{4.11}$$

This implies that δB is parallel to δv. The frozen-field condition, gives

$$\frac{\partial b}{\partial t} = B \frac{\partial v}{\partial z} \tag{4.12}$$

Combining these two equations gives the wave equation

$$\frac{\partial^2 b}{\partial t^2} = \left(\frac{B^2}{4\pi\rho}\xi\right) \frac{\partial^2 b}{\partial z^2} \equiv V_A' \frac{\partial^2 b}{\partial z^2} \tag{4.13}$$

Thus, the waves move with the speed V_A' along B. Assuming perturbations of the form $b_0 \exp[i(kz - \omega t)]$, we obtain the dispersion equation

$$\omega^2 - V_A'^2 k^2 = 0 \tag{4.14}$$

Note that the speed of the waves is affected by the anisotropy; the larger the anisotropy, the slower the wave, all other things being equal. Clearly, the waves

will propagate only if V_A is positive. For an isotropic plasma, $\xi = 1$ and $V_A' = V_A$, which is the familiar result from magnetohydrodynamic theory.

From the frozen-field equation (3.13)

$$\frac{\partial b}{\partial t} = - V_A' \frac{\partial b}{\partial z} \tag{4.15}$$

which with (4.12) gives

$$b = - \frac{B}{V_A'} v. \tag{4.16}$$

This can be written.

Unti and Neugebauer (196) searched for sinusoidal Alfven waves in the solar wind using magnetic field and plasma data from Mariner II. One result is given in Figure 4. This shows **B** (smoothed by a 19 point running average) in a coordinate system for which the minimum field fluctuation was in the xy plane and the average field along z, the bulk speed of the plasma is also shown. One sees a nearly sinusoidal, plane polarized wave with ∂**B** strongly correlated with V and δ**B** normal to **B**. Using the measured B and n to compute δv they found good agreement with the measured bulk speed perturbations (Figure 5), suggesting that (4.17) is satisfied. The initial density measurements, computed on the assumption of a strictly radial bulk velocity, did not satisfy the condition n = constant, necessary for an Alfven error, (in fact the density was strongly correlated with V (Figure 5) but this was probably an instrumental effect.

and the dispersion equation is

$$\omega^2 - k_z^2 V_A'^2 \cos^2 \theta = 0. \tag{4.20}$$

This is the only mode that can propagate in an incompressible hydromagnetic fluid.

Using an iteration technique, Unti and Neugebauer showed that the observations were consistent with the condition n = constant (see Figure 5).

Unti and Neugebauer (1968) searched for sinusoidal Alfven waves in the solar wind using magnetic field and plasma data from Mariner II. One result is given in Figure 4. This shows B (smoothed by a 19 point running average) in a coordinate system for which the minimum field fluctuation was in the xy plane and the average field along z, the bulk speed of the plasma is also shown. One sees a nearly sinusoidal, plane polarized wave with δB strongly correlated with V and δB normal to B. Using the measured B and n to compute $\delta \underset{\sim}{v}$ they found good agreement with the measured bulk speed perturbations (Figure 5), suggesting that (4.17) is satisfied. The initial density measurements, computed on the assumption of a strictly radial bulk velocity, did not satisfy the condition n = constant, necessary for an Alfven wave, (in fact the density was strongly correlated with V (Figure 5) but this was probably an instrumental effect.

Belcher et al. (1969) reported that correlation coefficients >.8 in absolute value between the radial component of the interplanetary magnetic field and solar wind speed were found at least 30% of the time in the 5 months of data from Mariner 5. They argued that these are due to large amplitude, aperiodic Alfven waves because: (1) the correlation is consistent with (4.17), (2) the density was not correlated with the field changes, (3) the value of B/V_A computed from plots of b versus V agrees with that given by (4.17) with $\xi = 1$ (see Figure 6a), and (4) the fluctuations δB tended to be normal to B (see Figure 6b). They also found that essentially all of the waves were propagating away from the sun, irrespective of the direction of the interplanetary magnetic field. This is evidence for the existence of Alfven waves in the solar wind and suggests the relatively common occurrence of such waves on a scale of several hours or more.

Coleman (1966) had previously noted a high value for the coherence he obtained from the cross spectrum for V and B , and he noted that the phase difference at a particular frequency obtained from the cross spectra for V and B was $\sim 180°$ when B was away from the sun and $\sim 0°$ when B was toward the sun. These evidently correspond to the results seen by Belcher et al. (1969), expressed in a different form. Coleman concluded that fast waves or Alfven waves (or both) were present, but he could not distinguish between the two. A more detailed account of this work also does not give positive evidence for Alfven waves (Coleman, 1967).

2. Magneto Acoustic Wave ($G \neq 0$, $M = 0$; $V_{\parallel} = 0$). While the Alfven waves propagate along $\mathbf{B}$ because of the tension in the field lines, the restoring force for these magneto acoustic waves arises from the compression of ρ and $\mathbf{B}$, and the wave propagates normal to $\underset{\sim}{B}$ (see Figure 2b). Taking $M = (\underset{\sim}{B} \cdot \nabla_{\perp})\, \mathbf{B} = 0$ (i.e., assuming the field lines do not bend) and $\mathbf{B} = (B_0 + b_z)\,\hat{z}$, the linearized form of (3.12) becomes

$$\rho \frac{\partial v}{\partial t} = - \nabla_{\perp} \left(\sum p_{i\perp} \right) + \frac{B}{4\pi} \frac{\partial b_z}{\partial x} \tag{4.21}$$

for a wave propagating along $\hat{x}$. The elements of the wave are shown in Figure 7. The frozen-in condition (3.13) gives

$$\frac{\partial b_z}{\partial t} = - B \frac{\partial V_x}{\partial x} \tag{4.22}$$

Operating on (4.22) by $\partial / \partial t$ and using the continuity equation gives

$$\frac{\partial^2 b_z}{\partial t^2} - (c_{\perp}^2 + V_A^2) \frac{\partial^2 b_z}{\partial x^2} = 0 \tag{4.23}$$

where

$$c_{\perp}^2 = \rho^{-1} \sum c_{i\perp}^2 \rho_i \quad \text{and} \quad c_{i\perp}^2 \equiv \frac{\partial p_{i\perp}}{\partial \rho_i} \tag{4.24}$$

Thus, the wave propagates along $\hat{x}$ with the speed

$$V_{MA}^2 = c_{\perp}^2 + V_A^2 \tag{4.25}$$

The dispersion equation is

$$c^2 - k_x^2 (c_\perp^2 + V_A^2) = 0 \qquad (4.26)$$

Burlaga (1968) has presented evidence for a magneto acoustic wave in the Pioneer 6 magnetometer data of Ness. This is shown in Figure 8 together with Pioneer 6 plasma data from the MIT probe. One sees sinusoidal oscillations in $|B|$, but none in B/B, as expected for a magneto acoustic wave. The plasma density and temperature should oscillate in phase with B. The density is given in Figure 8 to the nearest integer, reflecting the accuracy; this is not adequate to show the small oscillations that are expected. The temperature measurements suggest a maximum at the time of maximum compression, but they are not accurate enough to establish this with certainty. Note that to resolve these waves with a plasma probe it would be desirable to measure at least 2 spectra per minute, and since $\Delta n/n \approx \Delta B/B \approx .1$, the density should be measured with a relative uncertainty appreciably less than 10%.

3. "Fast Waves" ($G \neq 0$, $T \neq 0$; $v_\parallel = 0$). In this case both tensile and compressive stresses are active, but there are no displacements along $\underset{\sim}{B}$. Let $\hat{x}$ be along δv and take $\hat{k}$ and δB in the $\hat{x} - \hat{z}$ plane, (see Figure 9). The procedure of the preceding 2 sections gives the following equation

$$\frac{\partial^2 b_x}{\partial t^2} - (c_\perp^2 + V_A^2) \frac{\partial^2 b_x}{\partial x^2} - V_A'^2 \frac{\partial^2 b_x}{\partial z^2} = 0 \qquad (4.27)$$

and a similar equation for v_x. The dispersion equation is

$$\omega^2 - (c_\perp^2 + V_A^2)\, k_x^2 - V_A'^2\, k_z^2 = 0. \tag{4.28}$$

Clearly, the mode is related to the Alfven wave and the magneto acoustic wave discussed above.

If the compression is adiabatic with an adiabatic exponent $\gamma = 2$, then $p_{i\perp} = A_i\, \rho_i^2$ and $c_\perp^2 = 2\, \rho^{-1} \Sigma\, p_{i\perp}$ and (4.28) can be written

$$\omega^2 - a^2\, k_z^2 - b^2\, k_x^2 = 0 \tag{4.29}$$

where

$$a^2 \equiv \left(\frac{B^2}{4\pi} + 2\, p_\perp\right)\Big/\rho = V_A^2 + \frac{(p_\perp - p_\parallel)}{\rho} \tag{4.30}$$

and

$$b^2 \equiv \left(\frac{B^2}{4\pi} + 2\, p_\perp\right)\Big/\rho = V_A^2 + \frac{2\, p_\perp}{\rho} \tag{4.31}$$

Equation (4.29) is precisely the equation derived by Whang (1971) for a guiding center plasma.

Let the angle between $\hat{k}$ and B be θ. Then $k_y^2 = k^2 \sin^2\theta$ and $k_z^2 = k^2 \cos\theta$, and the dispersion equation (4.28) has the form

$$\omega^2 - k^2\, [(c_\perp^2 + V_A^2) - (c_\perp^2 + V_A^3\, (1 - \xi))\, \cos^2\theta] = 0 \tag{4.32}$$

This reduces to the dispersion equations derived above for Alfven waves and magneto sonic waves when $\theta = 0$ and $\pi/2$ (equations (4.20) and (4.26)), respectively.

Evidence for this type of wave was given by Whang and Ness (1970). They point out that the moon will generate such waves when the solar wind moves past it, as a result of the different magnetic permeability of the moon and the solar wind. The waves will form an elliptical Mach cone with the long axis perpendicular to the average field direction and the short axis along B_0, as a result of the asymmetry of the hodograph corresponding to (4.32). Crossings of the cone were identified in the magnetic field data from Explorer 35, as described by Whang and Ness (1970), and they obtained the Mach cone cross-section shown in Figure 10. It is an ellipse whose ratio of major and minor axes is in agreement with the fast wave theory given above. Michel (1967) had earlier predicted an elliptical Mach cone on the basis of a qualitative extension and application of ordinary, isotropic gas dynamics.

4. Coupling Between the Fast Wave and the Alfven wave. We have shown that a "fast" wave can propagate with $\hat{k}$, δB and δv in the x-z plane. This becomes an Alfven wave when $\hat{k}$ is along B and a magneto acoustic wave when $\hat{k}$ is normal to B. In addition, an Alfven wave can propagate along $\hat{k}$, with δv and δB along $\hat{y}$, normal to the x-y plane. Thus in general both types of waves can propogate simultaneously. Their hodographs are shown in Figure 11.

In the linear approximation, the fast wave and the Alfven wave are uncoupled and propagate independently. The fast mode causes oscillations in the intensity of B. Both the fast mode and the Alfven mode cause fluctuations in the direction of $\mathbf{B}$; in general, these polarization of these oscillators will be elliptical.

Burlaga found a wave in the Pioneer 6 data which has the characteristics just described (Figure 12). Again, however, the observations were not complete enough or accurate enough to verify the theory just presented.

The fast wave and Alfven wave in Figure 11 are uncoupled on the linear approximation. However, if the amplitudes of the oscillations are large, one must consider the effect of higher order terms. If the term of second order in b_y^2 is not discarded in the compressive term of the force equation (3.12), one gets

$$\frac{\partial^2 b_x}{\partial t^2} - (c_I^2 + V_A^2) \frac{\partial^2 b_x}{\partial x^2} - V_A'^2 \frac{\partial^2 b_x}{\partial z^2} = V_A^2 \frac{\partial^2 (b_y^2)}{\partial x^2} \tag{4.33}$$

which reduces to (4.27) when the term in b_y^2 is small. Thus the fast wave, which was confined to the x-z plane, can couple with the Alfven wave that has perturbations along $\hat{y}$, through the non-linear term on the RHS of (4.33). Kawashima (1969) first noted this (but there are some minor errors in his equation corresponding to (4.33)). He suggested that magneto acoustic waves are produced by non-linear Alfven waves in this way in the solar wind.

The power observed in the compressive waves is always lower than that in Alfven waves for frequencies in the range 10^{-5} to 10^{-2} Hz (e.g. Coleman, 1966) which is consistent with Kawashima's theory. Clearly, the coupling should be larger the larger the amplitude of the Alfven waves. Thus, the theory implies that the proportion of compressive waves to be large when the amplitude of the fluctuations is large. Kawashima used Ness' IMP 2 observations to show that this is the case (Figure 13).

5. Firehose Instability. The dispersion equation for Alfven waves (4.14) shows that waves grow with time (ω is imaginary) when $\xi < 0.$, i.e., when

$$\frac{\sum_i (p_{i\parallel} - p_{i\perp})}{B^2/(8\pi)} < 2 \qquad (4.34)$$

Parker (1957) was the first to suggest that this instability might occur in the solar wind. He derived an equation which is the same as 4.34 with i = 1, i.e., he considered protons only.

Kennell and Scarf (1968) pointed out that electrons should also be considered, and they obtained (4.34) with i = 2. Kennel and Scarf derived their result from the Boltzman equation. They wrote (4.34) in the form

$$2 - \beta_+ A_+ - \beta_- A_- < 0 \qquad (4.35)$$

where

$$\beta \pm \equiv \frac{P_{\parallel \pm}}{B^2/(8\pi)} \tag{4.36}$$

and

$$A_{\pm} \equiv \frac{T_{\parallel}^{\pm} - T_{\perp}^{\pm}}{T_{\parallel}^{\pm}} \tag{4.37}$$

The growth rate for the firehose instability is characterized by γ where

$$\left(\frac{\gamma}{V_A\, k}\right)^2 = |\xi| \tag{4.38}$$

Eviatar and Shultz (1970) found that the growth rate is so large in the solar wind that one would not expect to find

$$(B^2/8\pi)^{-1} \sum_i (P_{i\parallel} - P_{i\perp}) > 2.1.$$

in the solar wind, i.e., the firehose instability, would limit the thermal anisotropy. This raises the question, Does the anisotropy ever get large enough in the solar wind for the firehose instability to grow, or does some other mechanism destroy the anisotropy first?

There is no unambiguous evidence for the existence of the firehose instability in the solar wind at 1 AU. Scarf et. al. (1967) using average values for the solar wind parameters, concluded that (4.34) for protons is not satisfied, so the firehose instability is not expected to develop. Kennel and Scarf (1968) argued that protons alone cannot cause instability. But they argue that since the field is

disordered the electrons must be sufficiently hot and anisotropic that (4.34) is satisfied (assuming that the firehose instability is the cause of the fluctuations).

The most recent report of measurements by the Los Alamos group (Hundhausen et. al., 1970) gives $T^+_{max}/T^+_{min} = 1.9$, $T^+_{average} = 7.2 \times 10^4$ °K, and $n_{average} = 7.7\ cm^{-3}$. The electron temperature seems to be essentially constant, $T_e \sim (1.5 \pm .5) \times 10^5$ °K, as discussed in Section II, and the best measurements of the electron anisotropy give $.1 \lesssim (T^-_{\|} - T^-_{\perp})/T^-_{\|} \lesssim .2$. The average field is typically $\sim 6\gamma$. These numbers give $2 - \beta_+ \times A_+ - \beta_- \times A_- = .8$, so again one concludes that the firehose is not normally operative unless the electron anisotropy is larger than the current measurements indicate. One factor has still been left out – the α particles; but their anisotropy would have to be very large to have a significant effect, since their density is relatively low.

Eviatar and Shultz (1970) used Vela data to compute $\beta_{\|} - \beta_{\perp}$ for a single 5-hour period. The results (Figure 14) show that (4.34) was not satisfied for that period.

Burlaga et. al. (1969) considered the possibility that the instability might develop in some regions but not in others. They identified very quiet and very disturbed one hour intervals in the Explorer 34 magnetic field data (Figure 15) and computed β^+ for each of the intervals using the plasma and magnetic field data from that spacecraft. These intervals tended to be isolated, indicating that the disturbances were highly localized. They found that β^+ tended to be high for the

disturbed intervals, but low for the quiet intervals, which is, of course, what (4.34) would imply. Assuming that $.1 \lesssim (T_{\|}^{-} - T_{\perp}^{-})/T_{\|}^{-} \lesssim .2$, they found that $A^{+} + KA^{-} \lesssim 1.5$, where $K \equiv T^{-}/T^{+}$, so the instability condition (4.34), which can be written $\beta^{+}(A^{+} + KA^{-}) < 2$ is satisfied only if $\beta > 1.3$. Figure 15 shows that in fact the largest percentage of very disturbed intervals did occur when $\beta > 1.3$. Thus, there is evidence that necessary conditions for the firehouse instability do occur occasionally. However, there were very disturbed conditions when β^{+} was less than 1; in fact the most probable β^{+} for the disturbed intervals was .7. The most probable value of β^{+} for the Explorer 34 data ($\beta_{MP}^{+} = .3$) is appreciably less than that found by Neugebauer and Snyder (1967). The differences could be due to a systematic error in the Explorer 34 density measurements; but the absolute accuracy of density determination was estimated to be ±20% (Ogilvie et al. (1967), and this is consistent with other observations (Burlaga and Ogilvie, 1970; Gilbert, Private Communications.)

Summarizing, the firehose instability probably does occasionally occur in isolated intervals where β^{+} is large and possibly for most "very disturbed intervals", but it does not seem to be the primary cause of the fluctuations that are typically observed. Clearly, more measurements are needed.

Belcher and Davis (1971) reported a poor correlation between β^{+} and σ_{S1} the square root of the 3-hour average of the 168.75 sec minute total variance in field components. They considered this to be in conflict with the results of

Burlaga et al. (1969). There is no conflict, however. σ_{s1} is not a good measure of the type of high frequency fluctuations in the magnitude and direction of B studied by Burlaga et al..

D. $v_{\parallel} \neq 0$, $v_{\perp} \neq 0$ (General MHD Dispersion Equation). We have been discussing various special cases of low frequency, long wavelength waves. In general, all of the modes might exist and might be coupled. From isotropic mhd wave theory (e.g., Jeffrey and Taniuti (1964)) it is well known that 3 modes would then propagate: (1) the fast magneto acoustic mode, which reduces to the "fast" magneto acoustic wave discussed above for propagation normal to B, (2) The Alfven mode, and (3) the slow magneto acoustic mode, which reduces to the ion acoustic mode for propagation along B. The dispersion equation for an anisotropic medium is very complicated (It is given in Lüst, 1959), but gives the same qualitative features as that for an isotropic medium. The surfaces of normal speeds (hodographs) are shown in Figure 16. The fast magneto acoustic mode is the one most analagous to the sound wave in gas dynamics, in the sense that it propagates in all directions. Here, however, the propagation is anisotropic. The Alfven mode cannot propagate normal to B but it does propagate in all other directions, the speed being greatest and equal to the Alfven speed for propagation along B. The slow magneto acoustic wave has characteristics of both the Alfven wave and the sound wave; it does not propagate normal to B, but it does propagate in all other directions, the speed being greatest for propagation along B.

Figure 16 shows that 3 hodographs must be distinguished, corresponding to $V_A' < c_{\|}$, $Va' < c_{\|}$ and $V_A' = c_{\|}$. Although a distribution of $V_A'/c_{\|}$ has not been published, it is clear from the measure parameters that V_A'/c is typically very close to 1. This is an important point which has not been discussed enough in the literature. In principal, one can excite all 3 modes simultaneously by an instantaneous point disturbance in the solar wind, assuming that the ion acoustic wave propagates and is coupled to other modes. It is of interest to ask what is the form of the 3 corresponding wave fronts. For the three cases corresponding to the hodographs in Figure 16 the fronts at any instant are as shown in Figure 17. At a later time the fast wave front is larger. The slow wave front also enlarges with time, and it propagates along B.

As discussed earlier, the moon can act as a source of waves which propagate away from the moon while being convected by the solar wind. If the above theory applies, these waves will form one Mach cone corresponding to the fast mode, which is analogous to the aerodynamic Mach cone and equivalent to that predicted by Whang's model, and two Mach cones corresponding to the slow modes, when $V_A' \neq c_{\|}$. (When $V_A' = c_{\|}$, there is just one Mach cone.) These can be constructed from the Friedrichs diagram as illustrated in Figure 18. Under typical solar wind conditions near 1 AU it would be very difficult to observe the slow Mach cones, and in fact they would not always exist.

There is only indirect evidence for the existence of the slow mode on the solar wind. This is the observation of slow shocks, discussed in Section V.

V. Discontinuities

The theory of discontinuities in a steady state, isotropic hydromagnetic fluid is described in many texts (e.g. Jeffrey and Taniuti, 1964) and reviews (Colburn and Sonett, 1966) but the theory for an anisotropic fluid has been developed only recently in response to solar wind measurements. Lynn (1967) has presented the theory for a single species plasma in the CGL approximation. A similar theory for shocks was given by Abraham-Shrauner (1967). A less restrictive theory for shocks was given by Chao (1970) and a similar theory including other types of discontinuities was published by Hudson (1970). Neubauer (1970) has presented a theory of shocks in an anisotropic plasma which parallels that of Chao and Hudson. Our treatment will most resemble those of Chao and Hudson.

Let the discontinuity be a plane surface which moves with speed U along its normal $\hat{n}$ relative to a fixed frame (the sun, say). Let the subscripts 1 and 2 denote the regions away from the sun and toward the sun, respectively. Let the subscript t denote components along some direction parallel to the discontinuity surface.

Assume a steady state and work in a frame moving with the discontinuity surface.

Then, applying Gauss' theorem to (3.1) shows that the mass flux normal to the surface, G, is continuous across the surface,

$$G \equiv \rho_1 (v_{1n} - U) = \rho_2 (v_{2n} - U). \tag{5.1}$$

Since $\nabla \cdot B = 0$,

$$B_n \equiv B_{1n} = B_{2n}. \tag{5.2}$$

The frozen-field condition (3.13) implies that

$$B_n (v_{1t} - v_{2t}) = B_{1t} (v_{1n} - U) - B_{2t} (v_{2n} - U) \tag{5.3}$$

The momentum flux equation (3.12) gives 2 relations, one for the change in the normal momentum flux

$$\rho (v_n - U)^2 \Big|_1^2 = \left[\left(\sum p_{kl} + \frac{B^2}{8\pi}\right) - \frac{B_n^2 \xi}{4\pi}\right] \Bigg|_2^1, \tag{5.4}$$

another for the change in the transverse momentum flux

$$\rho v_t (v_n - U) \Big|_1^2 = \frac{B_n B_t}{4\pi} \xi \Big|_2^1. \tag{5.5}$$

Using (5.3), this can be written

$$G^2 \left(\frac{B_{1t}}{\rho_1} - \frac{B_{2t}}{\rho_2}\right) = \frac{B_n^2}{4\pi} (B_{1t} \xi_1 - B_{2t} \xi_2) \tag{5.6}$$

which with (5.1) gives

$$B_{1t} \rho_1 [(v_{1n} - U)^2 - V_{A1}'^2] = B_{2t} \rho_2 [(v_{2n} - U)^2 - V_{A2}'^2], \tag{5.7}$$

where

$$V'^2_{A_{1n}} = \frac{B_n^2}{4\pi\rho_1}\xi_1$$

and (5.8)

$$V'^2_{A_{2n}} = \frac{B_n^2}{4\pi\rho_2}\xi_2$$

are the Alfven speeds along the shock normal.

Finally, the energy equation (3.22) gives the following relation for the change in the kinetic energy flux normal to the surface.

$$\frac{\rho v^2}{2}(v_n - U)\Big|_1^2 = \left[\epsilon + \sum p_{k\perp} + \frac{B_t^2}{4\pi} + \frac{B_n^2}{B^2}\sum_k (p_{k\parallel} - p_{k\perp})\right](v_n - U)\Big|_2^1 \quad (5.9)$$

$$- B_n B_t \cdot v_t \xi/(4\pi)\Big|_2^1$$

where ϵ is given by (3.18).

Equations (5.1), (5.1), (5.3), (5.4), (5.5) and (5.9) are the basic jump equations. There are 8 equations for the 9 variables $\underset{\sim}{B}$, $\underset{\sim}{v}$, ρ, $p_\perp$ and $p_\parallel$.

Using (5.1) and (5.2), equations (5.3), (5.4), (5.5) and (5.9) can be written as follows

$$G\left(\frac{B_t}{\rho}\right)\Big|_1^2 = B_n (v_t)\Big|_1^2 \quad (5.10)$$

which with (5.1) gives

$$G \left. \frac{\mathcal{B}}{\rho} \right|_1^2 = \mathcal{B}_n (v) \Big|_1^2 ; \tag{5.11}$$

$$G^2 \left(\frac{1}{\rho} \right) \Bigg|_1^2 = \mathcal{B}_n^2 \left(\frac{\xi}{4\pi} \right) \Bigg|_1^2 + \left(\sum p_{k\perp} + \frac{\mathcal{B}^2}{8\pi} \right) \Bigg|_2^1 \tag{5.12}$$

$$G (v_t) \Big|_1^2 = \mathcal{B}_n \left(\frac{\mathcal{B}_t \xi}{4\pi} \right) \Big|_1^2 ; \tag{5.13}$$

and

$$G \left[\frac{v^2}{2} + \frac{\epsilon}{\rho} + \sum p_{k\perp} / \rho + \frac{\mathcal{B}_t^2}{4\pi\rho} \right] \Bigg|_1^2 = G \mathcal{B}_n^2 \sum \frac{(p_{k\parallel} - p_{k\perp})}{\mathcal{B}^2 \rho} \Bigg|_2^1 - \mathcal{B}_n \left(\frac{\xi \underset{\sim}{\mathcal{B}}_t \cdot \underset{\sim}{v}_t}{4\pi} \right) \Bigg|_2^1 . \tag{5.14}$$

Two general classes of discontinuities can be distinguished:

(1) Stationary discontinuities ($G = 0$)

(2) Shocks ($G \neq 0$)

B. Stationary Discontinuities. Since by definition $G = 0$ for a stationary discontinuity, $v_{n_1} = v_{n_2} = U$, which implies that the surface does not move relative to the plasma. There are two types of such discontinuities, corresponding to $\mathcal{B}_n = 0$ and $\mathcal{B}_n \neq 0$. These are called tangential discontinuities and contact discontinuities, respectively.

1. Tangential Discontinuities ($G = 0$, $\mathcal{B}_n = 0$). There are several necessary conditions for a tangential discontinuity:

(a) Since G = 0, it is non-propagating, i.e., the speed of the discontinuity surface relative to the solar wind in the direction of its normal is zero.

(b) $B_n = 0$ implies that $\underset{\sim}{B}_1$ and $\underset{\sim}{B}_2$ are parallel to the discontinuity surface (see Figure 19); hence the normal is

$$\hat{n} = B_1 \times B_2 / |B_1 \times B_2| \tag{5.15}$$

(c) Since there is no change on v_n, $\underset{\sim}{v}_1$ and $\underset{\sim}{v}_2$ are parallel to the surface; hence

$$\hat{n} = v_1 \times v_2 / |v_1 \times v_2| . \tag{5.16}$$

(d) The equation for the normal momentum flux (5.12) gives

$$\left(\sum p_{k\perp} + \frac{B^2}{8\pi} \right) \Bigg|_1^2 = 0, \tag{5.17}$$

which says that the pressure perpendicular to the surface is the same on both sides of the surface. Since $p_{k\perp} = n_k \kappa T_{\perp k}$, this may be written

$$\left(\sum n_k \kappa T_{\perp k} + \frac{B^2}{8\pi} \right) \Bigg|_1^2 = 0. \tag{5.18}$$

The equations for the transverse momentum flux and the energy flux, (5.13) and (5.14) are identically satisfied.

To positively identify a tangential discontinuity, one must show that all of the above conditions are satisfied, which requires simultaneous magnetic field data ($\vec{B}$ (t)) and plasma data (n, $T_\perp$, and $\vec{v}$ for protons, α's and electrons) and the arrival times at 4 spacecraft (to get the speed and orientation). Such a definitive measurement is still well beyond the scope of the observations, but there are several somewhat less complete results that are consistent with these conditions and leave little doubt about the existence of tangential discontinuities in the solar wind.

Figure 20, from Burlaga (1968), shows a region with at least 3 discontinuities which were observed by the spacecraft Pioneer 6. The discontinuity surfaces are moving past the spacecraft, nearly radially away from the sun with a speed $\sim$400 km/sec. They are seen as abrupt decreases in the magnetic field intensity (from Ness' magnetometer experiment) and simultaneous increases in the proton density (from the MIT plasma detector). The change in B occurs in $\lesssim$ 30 sec, implying a thickness $\lesssim$12,000 km $\approx 10^{-4}$ AU, assuming V $\approx$ 460 km/sec, which is indeed discontinuous on a scale of 1 AU. If the region in Figure 20 was isothermal and if $n_\alpha = a n_p$ there, then the total pressure is constant throughout the region if and only if $n \sim B^2$, since

$$8\pi \left[\sum p_{k\perp} + B^2/(8\pi) \right] = c\, n + B^2, \quad \text{where} \quad c = \kappa \left(T_{p\perp} + a\, T_{\alpha\perp} + (1 + 2a)\, T_e \right)$$

Figure 20 shows that in fact n is proportional to B^2 for the observations between 0630 and 0730. Thus the data are consistent with a constant pressure across each of the discontinuities, in agreement with (5.17).

Condition (5.15) can be tested only for discontinuities across which there is a significant change in the direction of $\underset{\sim}{B}$. Burlaga (1969a) has introduced the terms "directional discontinuity" for discontinuities across which the field direction changes by $> 30°$ in $\leq$ 30 sec. Figure 21 (from Ness et. al., 1966) shows 2 directional discontinuities, one seen at Pioneer 6, the other seen at Explorer 33.

Computing the orientation of the discontinuity surface from (5.15) and using the measured solar wind speed 400 km/sec, Burlaga and Ness (1969) computed that the discontinuity should have arrived at IMP 3 57.5 min after it was seen at Pioneer 6. The observed transit time was 53 min. Thus, the observations are consistent with the assumptions that $\underset{\sim}{B}$ was parallel to the surface and that the surface was convected with the solar wind speed, as required for a tangential discontinuity.

Burlaga and Ness (1969) used simultaneous magnetic field measurements from 3 spacecraft (Explorers 33, 34, and 35) to identify 6 directional discontinuities whose orientations determined from measured time delays and solar wind speeds, are consistent with those computed from (5.15). These results are shown in Figure 22. Consider panel A in this figure. A discontinuity was

observed first by the spacecraft at the point marked 1. Using the magnetic field data from that spacecraft, the surface normal was computed assuming (5.15) and the intersection of that surface with the ecliptic plane was computed and is shown by the line passing through point 1. A few minutes later, the same discontinuity was seen at another spacecraft at the point marked 2. The surface intersection was similarly computed using data from the second spacecraft at position 2. Minutes later it arrived at the spacecraft at point 3. Each of the panels refers to a different discontinuity surface and has a similar interpretation. If the surfaces are tangential discontinuities and if they are plane, the lines through points 1, 2, and 3 on each panel should be parallel. This is the case in A, D, E, and F, but in B and C the surfaces seem to be appreciably curved on a scale of 50 R_E. Note that the order of arrival of the surfaces at the different S/C depends on the surface orientation computed from (5.15). In every case, the arrival order is consistent with the assumption that the surfaces are tangential discontinuities with orientations given by (5.15). In this connection, D, E, and F are particularly noteworthy. Burlaga and Ness (1969) have shown that the actual surface orientations determined from the delay times and the measured solar wind speeds, are in very good agreement with the theoretical orientations shown in Figure 22. They also showed that (5.15) is satisfied for these discontinuities.

Equation 5.10 shows that $\underset{\sim}{v}_{1t}$, and $\underset{\sim}{v}_{2t}$ are arbitrary for a tangential discontinuity, since $G = 0$ and $B_n = 0$. (This does not consider the effect of instabilities which

might arise). In particular, since $v_{1n} = v_{2n}$, $|v_{1t}| \neq |v_{2t}|$ implies that one may have $|v_1| \neq |v_2|$. Such changes in the bulk speed do occur at directional discontinuities (Burlaga, 1968). Burlaga (1969) and Siscoe et al. (1969) have found discontinuities across which the bulk speed changed by 60 km/sec or more in less than ~3 min.

Siscoe et al. (1969) pointed out that in addition to conditions (5.15) to (5.18), a tangential discontinuity must satisfy the condition

$$\tan \psi = \frac{\Delta v_T}{\Delta v_k} \equiv \tan \psi_p \tag{5.19}$$

where the quantities ψ, Δv_T and Δv_k are as defined in Figure 23a. This simply says that a unit volume element initially adjacent to a tangential discontinuity surface always moves parallel to this surface as the surface moves away from the sun. If a discontinuity is tangential, ψ can be computed from (5.15) using measurements of $\underset{\sim}{B}$, and it can be computed independently from (5.19) using measurements of v. Siscoe et al. (1969) did this for 12 discontinuities in the Pioneer 6 data and found the results shown in Figure 23b. There is considerable scatter because of the relatively large errors in measuring the flow direction; in fact the error bars (not shown) are so large that only 1 point deviates significantly from the line $\psi = \psi_p$. Siscoe et al. concluded that the discontinuities were tangential.

We have been discussing discontinuities as if they have zero thickness, i.e. true discontinuities in the mathematical sense. Physically, of course, the surface has some structure. This has lead to some confusion. Figure 24 shows the "thickness" distribution of "discontinuities" in the magnetic field, studied by Siscoe et al. (1968). The "thickness" is here measured by the time for the surface to pass the spacecraft, which is on the order of the actual thickness divided by the solar wind speed. The shape of the distribution is very important, for it shows that these discontinuities are indeed a distinct class of thin structures and not simply the tail end of the distribution of fluctuations seen in space. Since the directional discontinuities studied by Burlaga (1969a) has the same statistical properties as those studied by Siscoe et al. (1968), they probably have the same kind of thickness distribution. The discontinuities studied recently by Smith et al., (1970) and Turner and Siscoe (1971) have $T \geq 300$ sec, which puts them far to the right of Figure 24 and may indicate that they are a different class of objects.

It is not clear whether the structure of tangential discontinuity surfaces in the solar wind can be analyzed within the framework of magnetohydrodynamics. In any case, it has not yet been done. One expects the fluid theory to be applicable on scales appreciably greater than the proton gyro radius, corresponding to $T \gg 1$ sec, which seems to be the case for most of the surfaces in Figure 24. Two types of structures have been identified in the magnetic field: (1) a laminar current sheet, in which $\mathbf{B}$ rotates more or less uniformly in the plane of the discontinuity surface as shown in Figure 25 (Siscoe et al. (1968), Burlaga and Ness

(1969)) and (2) a "turbulent" structure, as shown in Figure 26 from Burlaga (1969b). The study of such structures is still in an early stage.

Northrop and Birmingham (1970) studied the stability of discontinuity surfaces of finite thickness. Using an MHD energy principal due to Grad and Rebhan (1969), they gave an elegant proof that such surfaces are stable if $v_{1t} = v_{2t}$.

In addition to the structure of the current sheets associated with tangential discontinuities, illustrated in Figure 26, there is another type of structure which Burlaga and Ness (1968) called D-sheets. Two particularly noteworthy examples are shown in Figure 27, from Burlaga (1968). These are characterized by a dip in the intensity of B over an interval of a few minutes associated with a discontinuity in the direction of B. Several other examples are shown in Figure 28 from Burlaga and Ness (1968). The physical significance is not understood. If the dip were caused by the annihilation of the antiparallel components of B_1 and B_2, then one expects the minimum field to be related to the angle ω between B_1 and B_2, by the relation $B_{min}/B = \cos \omega/2$, if $B_1 = B_2$. Figure 29 (bottom) from Burlaga (1968) shows that this is the case for the D-sheets discontinuities in Figure 28 (top). It is not certain that the discontinuities with $B_1 = B_2$ are tangential. Figure 27 shows one D sheet associated with a large change in B and n, which is almost certainly a tangential discontinuity; here too, B_{min} is consistent with the annihilation hypothesis.

2. Contact discontinuity. In this case $G = 0$ but $B_n \neq 0$. It is convected, but (5.10) shows that in this case one must have $v_{1t} = v_{2t}$, i.e., there can be no relative motions along the discontinuity surface. This is because $\mathcal{B}$ is frozen to the plasma; a shear when $B_n \neq 0$ is impossible without breaking lines of force. In an isotropic plasma, conservation of transverse momentum (5.13) requires that $\underset{\sim}{B}_{1t} = \underset{\sim}{B}_{2t}$. So there is no change in $\underset{\sim}{B}$ across a contact discontinuity in an isotropic plasma— no change in the magnitude, no change in direction (see Figure 29). In an anisotropic plasma, however, one can have $\underset{\sim}{B}_{1t} \neq \underset{\sim}{B}_{2t}$ if $\xi_1 \neq \xi_2$ (see (5.13)). Thus, in an anisotropic plasma one can have a change in the magnitude and direction of $\underset{\sim}{B}$ across a contact discontinuity, but here as in the isotropic plasma $v_{1t} = v_{2t}$.

The pressure balance (normal momentum flux) condition (5.12) is

$$\left[\sum P_{kl} + \frac{B^2}{8\pi} - \frac{B_n^2}{B^2} \sum (P_{k\parallel} - P_{kl})\right]\Bigg|_1^2 = 0 \tag{5.20}$$

This has a simple geometrical interpretation. Let θ be the angle between $\mathcal{B}$ and $\hat{n}$. Then the pressure normal to the surface is

$$P_n = P_{\parallel_n} + P_{\perp_n} = P_{\parallel} \cos^2\theta + \left(P_{\perp} + \frac{B^2}{8\pi}\right) \sin^2\theta, \tag{5.21}$$

where

$$\cos\theta = \frac{B_n}{B},$$

Setting $p_{n1} = p_{n2}$ gives (5.20). Contact discontinuities have not been observed in the solar wind. It is widely believed that they will not be observed because they would rapidly broaden into a smooth transition.

C. Shocks

1. Introduction. A discontinuity is called a shock if $G \neq 0$. In aerodynamics there is basically just one kind of shock, and it correspond to the one type of wave in an ordinary gas, the sound wave. Gas enters an aerodynamic shock at a speed greater than the sound speed and leaves at a speed less than the sound speed. The energy is lost from the streaming goes into heating the gas. In magneto-gas-dynamics there are 3 basic wave modes, as discussed in Section IV and there is a corresponding variety of shocks. More complicated energy transfers are possible because of the presence of the magnetic sink.

We shall consider first the simple cases of shocks moving parallel to $\mathbf{B}$ or perpendicular to $\mathbf{B}$. Then we consider shocks more generally, shocks moving in arbitrary directions with respect to $\mathbf{B}$. Some special types of shocks will be discussed at the end of this section, together with a classification scheme. A detailed analytical theory of hydromagnetic shocks can be found in Jeffrey and Taniuti (1964).

In principle, a shock in the solar wind can move either away from the sun or toward it. Shocks moving away from the sun are called forward shocks, while shocks moving toward the sun are called reverse shocks.

Physically, there is no difference between a forward shock and a reverse shock, but there is probably a difference in the origin of the forward and reverse shocks that are observed in the solar wind. The origin of the observed reverse shocks, described below, is still a mystery.

2. Parallel Shocks. A parallel shock is one whose normal is parallel to $\mathbf{B}$. (See Figure 30). Two waves can propagate along $\mathbf{B}$, the acoustic wave and the Alfven wave. So immediately the question arises, "with respect to which of these modes is the shock supersonic?" The answer is somewhat complicated. We shall just present the results of Jeffrey and Taniuti (1964, p. 246).

If the sound speed is greater than the Alfven speed ahead of the shock, then the sound speed is dominant and one has an ordinary aerodynamic shock with gas entering faster than the sound speed $c_{\|}$ and leaving at a speed less than $c_{\|}$. The flow is super-Alfvenic on both sides of the shock and the sound speed exceeds the Alfven speed on both sides.

If the Alfven speed is larger than the sound speed ahead of the shock, there are 3 possibilities. The obvious one, with gas entering super-Alfvenically and leaving sub-Alfvenically probably does not occur in nature (Jeffrey and Taniuti 1964). Another possibility, with gas entering supersonically (and super-Alfvenically) and leaving subsonically (but still super-Alfvenically), is allowed and might be observed. Finally, gas might enter supersonically (but subalfvenically and leave at a speed which is either sub Alfvenic or subsonic.

For parallel shocks, (5.10) implies that $v_{1t} = v_{2t}$. There is no requirement that v_1, v_2, and $\hat{n}$ be coplamar. The magnetic field drops out of the Rankine Hugoniot equations, which become identical to those for aerodynamic shocks, except that they include both $p_\perp$ and $p_\parallel$ in the expression for internal energy, ϵ. These equations provide no insight concerning the possible change in anisotropy (distribution of internal energy) across a parallel shock.

There are no observations of parallel shocks in the solar wind. Such observations would be of special interest.

3. Perpendicular Shock. A shock is called a perpendicular shock if the shock normal is perpendicular to $\mathbf{B}$. In this case $B_n = 0$ and the magnetic field is parallel to the shock surface on both sides of the shock, as shown in Figure 31.

The only wave that propagates perpendicular to $\mathbf{B}$ is the magneto acoustic wave, whose speed is $V_M^2 = V_A^2 + c_\perp^2$. The flow enters a perpendicular shock at a speed greater than V_M and leaves at a speed less than V_M. Thus, this shock propagates supermagnetoacoustically.

For a perpendicular shock, the mass flux and frozen field equations (5.11) give

$$\frac{B_1}{\rho_1} = \frac{B_2}{\rho_2}, \tag{5.22}$$

which states that (a) the magnetic field direction does not change across the shock, and (b), its intensity changes in the same ratio as the density, $B_1/B_2 = \rho_1/\rho_2$.

Equation 5.13 shows that there is no change in the transverse momentum flux across a shock when $B_n = 0$, so $v_{1t} = v_{2t}$. This implies that $v_2 - v_1 = (v_{2n} - v_{1n})\hat{n}$, so that $\hat{n}$ is parallel to $v_1 - v_2$ for a perpendicular shock.

The normal momentum flux equation (5.4), gives

$$\rho (v_n - U)^2 \Big|_1^2 = \left(\sum p_{kl} + \frac{B^2}{8\pi}\right)\Big|_2^1, \tag{5.24}$$

i.e. the change in the normal momentum flux is balanced by a change in the pressure. This is the same as for an ordinary gas dynamic shock, except that here the magnetic field pressure adds to the particle pressure.

Equation (5.9) shows that the change in the kinetic energy flux normal to the surface is

$$\frac{\rho v^2}{2}(v_n - U)\Big|_1^2 = \left[\epsilon + \left(\sum p_{kl} + \frac{B^2}{8\pi}\right)\right]\Big|_2^1, \tag{5.25}$$

which is likewise the familiar gas dynamic result with the addition of the magnetic pressure to the thermal pressure.

Note that the parallel pressure does not appear in the Rankine-Hugoniot equations.

4. Reverse Perpendicular Shock. As we have said, a reverse shock is one which propagates toward the sun relative to a frame moving with the plasma.

Since the solar wind speed is usually higher than the shock speeds, the shock can actually move away from the sun while propagating toward the sun. In this case, a spacecraft sees the "back," high entropy, side first and then the "front." This means that the density, temperature, and magnetic field intensity should be seen to decrease simultaneously as the shock is carried past the spacecraft. As always, the speed behind the shock is lower than that ahead of the shock, so in the case of a reverse shock $(v_{n1} - \underset{\sim}{U})$ $(v_{n2} - \underset{\sim}{U})$, since the subscript 1 refers to the side away from the sun. Thus, $v_{n2} > v_{n1}$ and an observer at a fixed spacecraft would see the bulk speed increase.

While a reverse shock looks different in the data in the sense just discussed, it satisfies the same equations as the forward shock (taking proper account of the sign of U, of course).

A perpendicular shock was found in the solar wind by Ogilive and Burlaga (1969) using Explorer 34 magnetic field and plasma data. It passed the spacecraft at 1732 UT on Aug. 29, 1967. As shown in Table III, the bulk speed, density, temperature and magnetic field intensity all increased simultaneously, but there was no change on the direction of the magnetic field. The shock surface moved past 3 spacecraft, each carrying one of Ness' magnetometers. The transit times were measured, and using these the orientation of the shock surface was computed with the result shown in Figure 32. The shock normal determined in this way is $\hat{n}$ (-.93, -.33, 1.5) in solar ecliptic coordinates i.e., $\theta_n = 9°$, $\phi_n = 200°$.

Table III

1732 UT, Aug. 29, 1967 Shock

	V (km/sec)	n(cm^{-3})	T(°K)	B(γ)	θ.	φ
Before	418	2.6	6.5×10^4	5.5	51°	295°
After	452	3.7	12×10^4	7.2	51°	296°

This is essentially normal to the magnetic field, B_1 and B_2, as required for a perpendicular shock.

From the multi spacecraft measurements, the speed of the surface was found to be U = (436 ± 110) km/sec. This compares favorably with the value obtained from the mass flux conservation condition (5.1), viz U = 496 km/sec.

Equation (5.22), which is a consequence of the frozen field condition, is satisfied since (a) the field direction did not change, and (b) the measured ratio $B_1/n_1 = 2.0$ equals the ratio $B_2/n_2 = 1.9$ within the experimental errors.

The change in the momentum flux, $\rho (V_n - U)^2 \Big|_2^1$, was 1.4×10^{-10} dynes/cm^3, which is equal to the change in pressure

$$\left[\sum P_{kl} + \frac{B^2}{8\pi}\right] \Bigg|_1^2 = 1.5 \times 10^{-10} \text{ dynes/cm}^2$$

(The pressure here was computed assuming that $T_{e1} = T_{e2} = 1.5 \times 10^5$ °K and that the contribution of the α's is negligible.) Thus (5.24) is satisfied.

Finally, the change in the kinetic energy flux given by the LHS of (5.25) was consistent with the observed change in the RHS of (5.25) within the errors.

Burlaga (1970) identified a reverse perpendicular shock in the Explorer 34 plasma and magnetic field data of Ogilvie and Ness. The observations are

Table IV

Sept. 28, 1967

	V (km/sec)	n (cm^{-3})	T (°K)	B(γ)	θ	φ
Before	540	10	4.5×10^5	12	40°	130°
After	585	5.5	2.6×10^5	8	43°	125°

shown in Figure 33 where the decrease in n, T, and B_t and the increase in V required for a reverse perpendicular shock are clearly seen. Table IV shows the magnitude of these changes together with the magnetic field directions. The magnetic field direction did not change, within the measurement uncertainties ($\approx \pm 5°$), as required for a perpendicular shock (Equation (5.22)).

The shock surface moved past 3 spacecraft, each carrying one of Ness' magnetometers, just as the forward perpendicular shock discussed in the previous section. The shock normal was found to be $\hat{n} = (-.70, -.69, .18)$, i.e., $\theta_n = 10°$, $\phi_n = 225°$. This is essentially normal to the magnetic field ($\cos^{-1}(\hat{n} \cdot \hat{B}) = 87°$), as required for a perpendicular shock.

Using the multispacecraft magnetometer measurements of Ness and the conservation of mass flux equation (5.1), the shock surface was found to be moving at a speed U = 270 km/sec. in the sunward direction. Since this speed is less than the component of the solar wind speed along the normal, the shock was carried away from the sun despite its motion toward the sun relative to the moving plasma. The speed on the sun-ward side of the shock (i.e., ahead of the shock) was $V_{2n} - U = 141$ km/sec. This is greater than the magneto-acoustic speed $V_{M1} = 95$ km/sec. On the opposite side it was $(V_{N1} - U) = 76$ km/sec which is less than the magneto-acoustic speed $V_{M2} = 110$ km/sec. Thus the normal speed relative the surface shock did decrease, as required for a shock and the flow was supermagneto-acoustic ahead of the shock and submagneto-acoustic

behind it. The component of v tangent to the surface was found to be 414 km/sec on side 1 and 416 km/sec on side 2, consistent with the requirement that $v_{1t} = v_{2t}$. The condition $B_1/n_1 = B_2/n_2$, from the frozen-field condition, is satisfied within the errors for this shock, for Table IV gives

$$B_1/n_1 = 1.2 \pm .2, \quad \text{and} \quad B_2/n_2 = 1.5 \pm .1$$

The change in the momentum flux was $\rho v_n^2 \Big|_1^2 = 8.6 \times 10^{-10}$ ergs/cm^2. This was balanced by a change in the pressure

$$p \Big|_2^1 \equiv \sum p_\perp + \frac{B^2}{8\pi} = 8.0 \times 10^{-10} \text{ ergs/cm}^2$$

(computed as for the forward perpendicular shock in the preceding section), as required by (5.24).)

Similarly the change in the normal kinetic energy flux, 7.1×10^{13} (cm/sec)^2 was found to agree with the change in the RHS of (5.25), 5.5×10^{13}(cm/sec)^2, within the experimental errors.

Thus, all of the conditions for a reverse perpendicular shock were satisfied.

5. Fast Shock. Two kinds of shocks can propagate at an angle with respect to the magnetic field. These correspond to the 2 kinds of magneto acoustic wave, the fast wave and the slow wave. Gas enters the fast shock at a speed greater than

the speed of the fast wave in the direction of the shock normal and leaves at a speed less than this. Thus, the flow is superfast ahead of the fast shock and subfast behind it, but the flow is super-Alfvenic on both sides of the shock (Jeffrey and Taniuti, 1964). The fast shock is the most frequently observed type of shock in the solar wind, perhaps because of the similarity of the fast magneto-acoustic wave with the acoustic wave in aerodynamics.

Since the fast shock normal is not parallel to B, B_n and B_t are both non-zero (See Figure 34) Equation shows that B_{1t} is parallel to B_{2t} at a fast shock; hence B_1, B_2 and $\hat{n}$ are coplanar. Equation 5.10 shows that $v_{1t} - v_{2t}$ is parallel to $B_{1t} - B_{2t}$, and is thus parallel to B_{1t} and B_{2t} and coplanar with $\hat{n}$. Then $v_1 - v_2$ and $\hat{n}$ are also coplanar. Summarizing, $\hat{n}$, B_1, B_2, and $v_1 - v_2$ are coplanar. This was demonstrated for an anisotropic plasma by Chao (1970) and independently by Hudson (1970) and Neubauer (1970).

The shock normal can be calculated from B_1 and B_2 as follows. Since B_1, B_2 and $\hat{n}$ are coplanar, $B_1 \times B_2$ is in the plane of the shock. It was shown that $B_1 - B_2$ is also in the shock plane. Thus $\hat{n}$ is normal to both $B_1 \times B_2$ and $B_1 - B_2$,

$$\hat{n} = (\overline{B}_1 - \overline{B}_2) \times (\overline{B}_1 \times \overline{B}_2) / |(\overline{B}_1 - \overline{B}_2) \times (\overline{B}_1 \times \overline{B}_2)| \qquad (5.26)$$

Note that the formula does not give a normal for parallel or perpendicular shocks. It can be used to determine $\hat{n}$ for fast shocks only if the angle ω between

$\overline{B}_1$ and $\overline{B}_2$, is larger than the uncertainties in B_1 and B_2. Since ω is generally less than 15° for shocks in the solar wind and since the uncertainties in $\overline{B}_1$ and $\overline{B}_2$ are commonly ~ 5° or more, the errors in $\hat{n}$ determined this way may be very large, sometimes so large that $\hat{n}$ is meaningless. Clearly, more accurate normals can be obtained by reducing the uncertainties in B_1 and B_2. Lepping and Argentiero (1971) accomplished this by developing a "least-squares" technique which gives the best estimate values of B_1 and B_2 by requiring that the observations of v_1, v_2, B_1, B_2, ρ_1 and ρ_2 satisfy (5.1), (5.10), (5.13) with $\xi = 1$ and $[B_n]_1^2 = 0$. As an example, consider the shock seen by Ness' (Pioneer 7) magnetometer on Aug. 29, 1966. Using mean values of B in (5.26) gives an error cone for $\hat{n}$ of 25°. The Lepping-Argentiero method gives an error cone of only 6°. (The error cone is here defined such that there is a 95% confidence that the normal is within it.) Chao (1970) introduced another method for obtaining best estimates of $\underset{\sim}{B}$, an iterative trial and error procedure, which is simpler than the Lepping-Argentiero method, but does not always give as much accuracy. The accurate determination of shock normals is essential for studies of shock geometry an and the interactions of shock with discontinuities.

Other methods for determining $\hat{n}$ can be used for shocks that are identified at 2 or more spacecraft, if one can assume that the shock surface is plane over distances equal to the spacecraft separations. Sonett et al. (1964) used such a method to determine $\hat{n}$ for the shock on Oct. 7, 1962. Chao (1970) gives the formula $\hat{n} = [B_1 \times (v_2 - v_1)] \times U / |[B_1 \times (v_2 - v_1)] \times U|$ where $U = R/T -$

$(\rho_2 v_2 - \rho_2 v_2)/(\rho_2 - \rho_1)$, $\underset{\sim}{R}$ and T being the vector displacement and time delay between the spacecraft. Ogilvie and Burlaga (1969, erratum, 1970) introduced a method for calculating $\hat{n}$ using simultaneous measurements from 3 spacecraft, the four parameters $\hat{n}, U$ were determined from the 3 arrival times and the condition that $B_2 - B_1$ must lie in the shock plane.

Greenstadt et al. (1970) used onset times from 3 spacecraft and certain limits on the shock speed to obtain limits on $\hat{n}$ for the 7 July 1966 shock. These limits were narrowed using the time of the associated sudden commencement. Their basic result, that the shock normal pointed 65° to 70° below the ecliptic, is surprising. It should be noted that the 3 spacecraft which they used were all close to the ecliptic plane, so the most important component of $\hat{n}$, n_{2z}, was the least accurately determined. If one uses the intercept of shock surface with the ecliptic ($\hat{T}$ = (.276, .961, 0)) which was determined by Greenstadt et al. (which is quite accurately determined by their method since the spacecraft were widely separated in the ecliptic plane) and if one uses the value $B_1 - B_2$ = (-2.0, 6.4, 4.4) which they give, then the method of Ogilive and Burlaga (1969) gives $\hat{n} = \hat{\underset{\sim}{I}} \times (B_1 - B_2)/|\hat{T} \times (B_1 - B_2)|$ = (.96 - .275, - .04), which implies an inclination θ_n = - 40°. This smaller value of θ_n (i.e., shock normal closer to the ecliptic plane) is more consistent with other values that have been published (Chao, 1970, Ogilvie and Burlaga, 1969), and agrees closely with the value θ_n = - 37° obtained from (5.26) by Greenstadt et al.

Another method of determining shock normals was given by Burlaga (1970) who used onset times from 3 spacecraft, the measured solar wind speed, and (5.1) to calculate $\hat{n}$ and U by means of an iteration scheme. In his equations (13) and (14), tan θ should be replaced by tan θ sec ϕ.

Given the shock orientation and a complete set of measurements, one can easily determine whether the momentum flux and energy flux equations are satisfied. However, in practice one cannot measure all of the quantities in these equations. The magnetic field is known more precisely than the plasma parameters, so it is convenient to replace these equations by expressions for the jumps n_2/n_1, $T_{\parallel 2}/T_{\parallel 1}$, $T_{\perp 2}/T_{\perp 1}$ as functions of the magnetic field parameters and the upstream Alfven Mach number. Using frozen-field conditions (5.3), the transverse momentum flux equation (5.5) can be written

$$\frac{\rho_1}{\rho_2} = \left(\frac{\xi_2}{\xi_1} - \frac{B_{1t}}{B_{2t}}\right) M_{A1}^2 \xi_1 + \frac{B_{1t}}{B_{2t}} \tag{5.27}$$

This is equivalent to (5.6). Chao (1970) has used a form of this equation to study the variation of n_1/n_2 versus ξ_2 for various values of the other parameters. When $\xi_1 = \xi_2 = 1$ (5.27) reduces to an equation derived by Wilkerson (1969).

For a gas consisting of protons and electrons the normal momentum flux equation (5.4) can be written

$$\frac{T_{\perp 2}^{+} + T_{\perp 2}^{-}}{T_{\perp 1}^{+} + T_{\perp 1}^{+}} = \frac{n_1}{n_2}\left\{1 - r_0\left(1 - \frac{n_1}{n_2}\right) + \beta_{\perp 1}^{-1}\left(1 - \frac{B_2^2}{B_1^2}\right) + C\left(1 - \frac{\xi_2}{\xi_1}\right)\right\} \tag{5.28}$$

where

$$r_0 \equiv \frac{\rho_1 (V_{1n} - U)^2}{n_i k (T_{\perp 1}^+ + T_{\perp 1}^-)}$$

and

$$\beta_{\perp 1}^{-1} = \frac{B_1^2}{8 \pi n_1 k (T_{\perp 1}^+ + T_{\perp 1}^-)}$$

$$C = \frac{B_n^2 \xi_1}{4 \pi n_1 k (T_{\perp 1}^+ + T_{\perp 1}^-)}$$

This also reduces to an equation derived by Wilkerson (1969) when $\xi_1 = \xi_2 = 1$.

Now let us turn briefly to the observations of fast shocks. Numerous fast forward shocks have been identified in the solar wind, the first by Sonett et al. (1964). A list of fast shocks and the corresponding references may be found in Hundhausen (1970). We shall give just one example, the shock of Aug. 29, 1966.

Plasma data from the MIT probe on Pioneer 7 and simultaneous magnetic field from Ness' magnetometer are summarized in Figure 35 from Chao (1970) together with Chao's "best fit" to the Rankine-Hugoniot equations with $\xi_1 = \xi_2$. Table IV gives the somewhat better "best fit" values of Lepping and Argenterio (1970). Clearly, the R-H equations are approximately satisfied. Lepping and Argentiero, using the method described above, found that the shock normal was $\phi_n = 197°$, $\theta_n = 19°$, within an error cone of 6°. Using this value for $\hat{n}$ and the time 48.5 min that it took for the shock to move from Explorer 33 to Pioneer 7, which were separated by the vector $\underset{\sim}{R} = (1.29, .59, .16) \times 10^6$ km/sec, (See Figure 36). The shock speed was found to be 471 km/sec. This compares well with the value 467 km/sec obtained by Lepping and Argentiero from the Rankine Hugoniot equations.

The observation of a reverse fast shock was recently reported by Chao and Binsack (1971). The earth's bow shock is a stationary reverse fast shock which propagates toward the sun at a speed just equal to the solar wind speed. It has been extensively studied, and the results are summarized in recent reviews by Spreiter and Alksne (1969) and by Wolfe and Intriligator (1970).

$n_1 = n_2$ shocks. The above discussion assumes that $n_1 \neq n_2$ for the fast shocks. Formally, one can set $n_1 = n_2$ and still have $v_n \neq 0$. In this case, $v_{1n} = v_{2n}$. Now if $V'_{A1} \neq V'_{A2}$, then (5.7) shows that B_{1t} and B_{2t} are colinear, as for a fast shock. Solving (5.7) for $V_n - U$ gives

$$(v_{1n} - U)^2 = \frac{V'^2_{A1} B_{1t} - V'^2_{A2} B_{2t}}{B_{1t} - B_{2t}} \tag{5.29}$$

Introducing the definition of V'_A and ξ, gives

$$(v_{1n} - U) = \left\{ \frac{B_n^2 \left[(B_{1t} - B_{2t}) B_1^2 B_2^2 + 4\pi B_{2t} (p_{\parallel 1} - p_{\perp 2}) B_1^2 - 4\pi B_{1t} B_2^2 (p_{\parallel 1} - p_{\parallel 2}) \right]}{4\pi \rho (B_{1t} - B_{2t}) B_1^2 B_2^2} \right\}^{1/2} \tag{5.30}$$

Clearly, $B_1 \neq B_2$ for these discontinuities.

Shocks of this sort were predicted by Ivanov (1970) who called them "rotational discontinuities" because in the limit of zero anisotropy the shock speed goes to V_A. This name is somewhat misleading, however, since an essential property is the colinearity of B_{1t} and B_{2t}, which makes it more like a fast shock than

a rotational discontinuity. (Ordinary rotational discontinuities derived their name from the characteristic that B_t rotates across the plane of the discontinuity so that B_{2t} and B_{1t} are generally not parallel.) It is true that

$$v_t \Big|_1^2 = B_t \Big|_1^2 \frac{v_n}{B_n}$$

for both Ivanov's discontinuities and Alfven shocks, but this follows directly from (5.5) and the assumption that $\rho_1 = \rho_2$. Since B_{1t} and B_{2t} are colinear, the coplanarity theorem applies to $n_1 = n_2$ discontinuities (but not to Alfven shocks), and the normal is given by (5.26).

Ivanov (1970) suggested that 10 out of 11 of the large velocity discontinuities in Burlaga (1969b) are shocks with $n_1 = n_2$. However, additional data presented by Burlaga (1971) show that this cannot be correct, since in the cases where the orientation of the surfaces can be determined directly, it is not that which is predicted by Ivanov. Further evidence in Burlaga and Chao (1971) shows that discontinuous changes in B are accompanied by density changes at least 95% of the time, which indicates that $n_1 = n_2$ shocks are seldom, if ever, present.

6. Slow Shocks. The slow shock propagates at an angle with respect to B (see Figure 37) and corresponds to the slow magneto-acoustic wave mode. Gas enters at a superslow speed and leaves at a subslow speed. The flow is sub-alfvenic on both sides of the shock. An important and distinctive characteristic of a slow shock is that the magnetic field intensity is lower behind the shock

than ahead of it; magnetic energy is lost, presumably by conversion to thermal energy or possibly to wave energy. The fractional change in B_t, $-[B_t]/B_1$, is a measure of the shock strength.

The Rankine-Hugoniot equations for slow shocks are essentially the same as for fast shocks.

Slow shocks were first identified in the solar wind by Chao and Olbert (1970) using Mariner 5 plasma and magnetic field data. The observations of the 2 slow shocks discussed by Chao and Olbert are shown in Figure 38. It is clear that these slow shocks are not as thin as fast shocks and the fluctuations near these slow shocks are larger than is usually observed at fast shocks. Nevertheless, the signature of each of these 2 discontinuities is clearly that of a slow shock (an increase in n, v and T and a decrease in B). The dashed lines in Figure 38 are "best-fits" to the Rankine-Hugoniot equations, obtained by the trial and error procedure of Chao (1970). These are not unique fits, but they do show that there is a solution of the Rankine -Hugoniot equations for an isotropic plasma which is consistent with the observations. The condition that the flow must be subalfvenic on both sides of a slow shock was satisfied for the 2 shocks in Chao and Olbert (1970). The condition that flow be superslow ahead and subslow behind the shocks was not verified directly because the electron temperature was not known; however, using the value of v_{slow} determined by their fit to the Rankine-Hugoniot equations, Chao and Olbert found $M_{slow} = 1.5$

before and .7 after the shock on July 20, 1967, and M_{slow} = 1.8 before and .6 after the shock on August 30, 1967.

Another slow shock was identified in Pioneer 6 data by Burlaga and Chao (1971). This is shown in Figure 39 together with fits to the R-H equations obtained by Chao's method. The speed normal (on RTN coordinates) and Mach numbers for this shock are shown in Table V together with the same parameters for the shocks in Chao and Olbert (1970).

A reverse slow shock was also identified in the Pioneer 6 data by Burlaga and Chao (1970). The data are shown in Figure 40 together with a fit to the Rankine Hugoniot equations using the method of Chao. The speed, orientation and Mach numbers for this shock, which occurred at 0901 UT on Jan. 19, 1966, are shown in Table V. There was only a small drop in the flow speed across the shock, from 29 km/sec to 23 km/sec, but there was a significant drop in the magnetic field intensity, from 5.2γ to 4.2γ. The loss of magnetic energy is comparable to the loss in flow energy.

The existence of slow shocks in the solar wind is strong indirect evidence for the existence of the slow magneto-acoustic wave and the ion-acoustic wave in the solar wind.

6. Alfven Shock. Strictly speaking there is no Alfven shock corresponding to the Alfven wave in the same sense that fast and slow shock correspond to

Table 5

Slow Shocks

Date	July 20, 1967	Forward Aug. 30, 1967	Jan. 20, 1966	Reverse Jan. 19, 1966
$\hat{n}$	(.38, -.80, .47)	(.01, -.09, -.99)	(.75, .30, .60)	(.85, .01, .54)
V_s (km/sec)	130	2	323	251
$M_{A,1}$	0.9	0.9	0.9	0.9
$M_{A,2}$	0.7	0.6	0.8	0.8
$M_{slow,1}$	1.5	1.8	1.3	1.2
$M_{slow,2}$	0.7	0.6	0.8	0.8

fast and slow magneto acoustic wave. This point is clear from our earlier discussion of parallel shocks. It can probably be traced to the fact that Alfven waves are not compressive. There is, however, another shock ($G \neq 0$) which is unique to magnetohydrodynamics; it is called an Alfven shock. This is illustrated in Figure 41. The flow is alfvenic on both sides of this shock ($M'_{A1} = M'_{A2} = 1$), so the discontinuity propagates at the Alfven speed, essentially like a kink in the magnetic field. For an Alfven shock $B_n \neq 0$, and (5.7) shows that B_{1t} and B_{2t} need not be parallel (see Figure 41). In fact, the Alfven shock is often called a rotational discontinuity because B_{2t} is rotated in the shock surface with respect to B_{1t}. Clearly, B_1, B_2 and $\hat{n}$ are not coplanar, in distinction to the fast and slow shocks. In this case, $B_1 \times B_2 = B_n \times (B_{2t} - B_{1t}) + B_{1t} \times B_{2t}$ is not in the shock surface, so the Alfven shock normal is not given by (5.26).

Equation (5.13) shows that the velocity change and magnetic field change are related by

$$\underset{\sim}{v}_1 - \underset{\sim}{v}_2 = \mp\left(\frac{\underset{\sim}{B}_1\,\xi_1}{\sqrt{4\pi\rho_1}} - \frac{\underset{\sim}{B}_2\,\xi_2}{\sqrt{4\pi\rho_2}}\right) \tag{5.31}$$

Since

$$G^2 = \rho^2\,(v - U)^2 = \rho^2\,V_A'^2 = \frac{B_n^2}{4\pi}\,\rho\,\xi,$$

the normal momentum flux equation (5.12) gives

$$\left[\sum p_{k\perp} + \frac{B^2}{8\pi}\right]_1^2 = 0 \tag{5.32}$$

which is the same as the condition derived for a tangential discontinuity. The energy flux equation (5.14) becomes

$$\rho^{-1}\left[\epsilon + \sum(p_{\parallel} + p_{\perp})/2 + B^2/8\pi\right]_1^2 = 0 \tag{5.33}$$

If the anisotropy does not change across an Alfven shock, $\xi_1 = \xi_2$, then the conservation of mass flux (5.1) implies that $\rho_1 = \rho_2$. Then (5.32) and (5.33) give $\epsilon_1 = \epsilon_2$ which implies that $\rho_2 = \rho_1$. Putting this into (5.32) gives $B_1 = B_2$. Thus, if $\xi_1 = \xi_2$, then $B_1 = B_2$ and $\rho_1 = \rho_2$. However, if $\xi_1 \neq \xi_2$, $B_1 \neq B_2$; this important fact was first noted by Hudson (1970).

Evidence for Alfven shocks was found by Belcher and Davis (1971) in the Mariner 5 plasma data of Bridge, Lazarus, and Snyder and the magnetic field data of Coleman, Jones and Smith. This is shown in Figure 42,

where it is seen that (5.31) with $\xi_1 = \xi_2 = 1$ is satisfied for at least 2 discontinuities. There was no appreciable change in n, as required for an Alfven shock with $\xi_1 = \xi_2$. No temperature measurements were given, but presumably $\Sigma T_1 = \Sigma T_2$. It was found that $B_1 = B_2$, but this result is not independent of an assumption which was made to obtain the spacecraft field.

Alfven shocks may be pictured as propagating "kinks" in the interplanetary magnetic field. Parker (1963) was the first to suggest that they are present and indicated that they might be important as cosmic ray scattering centers. Quenby et al. (1970) have given this idea some experimental support. No measurement of the speed of an Alfven shock has been made.

Classification of Shocks. Here we simply note how the types of shocks discussed above can be viewed as different solutions of (5.7), which can be written

$$\underset{\sim}{B}_{1t}\, \rho_1\, V'^2_{A1}\, (1 - M'^2_{A1}) = \underset{\sim}{B}_{2t}\, \rho_2\, V'^2_{A2}\, (1 - M'^2_{A2}) \tag{5.34}$$

Parallel shock: $B_{1t} = B_{2t} = 0$

Perpendicular shock: $V'^2_{A1} = V'^2_{A2} = 0$

Alfven shock: $M'_{A1} = 1$; $M'_{A2} = 1$

Fast Shock: $M'_{A1} > 1$; $M'_{A2} > 1$

($n_1 = n_2$ shock. $\rho_1 = \rho_2$)

Slow shock: $M'_{A1} < 1$; $M'_{A2} < 1$

Other solutions are formally possible: $M'_{A1} = 1$, $M'_{A2} \neq 1$ (switch-off shock). $M'_{A1} \neq 1$, $M'_{A2} = 1$ (switch-on shock); $M'_{A1} > 1$, $M'_{A2} < 1$; $M'_{A2} < 1$, $M'_{A1} > 1$. But these are not "evolutionary", and they are not expected to be observed in the solar wind.

VI. Summary and Discussions of Problems for Future Study

We have considered the applicability of hydromagnetic theory to the study of the microstructure of the solar wind. In particular, we have presented the theory of hydromagnetic waves and discontinuities which is appropriate for the solar-wind, and we have reviewed the experimental evidence for the various waves, discontinuities and some of the instabilities which are predicted by this theory.

Nearly all of the discontinuities given by the theory have been shown to exist in the solar wind. These include tangential discontinuities, forward and reverse fast and slow shocks, perpendicular shocks, and Alfven shocks. Parallel shocks have not been found; their existence would be of special interest, since it would be clear evidence for the existence of a longitudinal wave mode and would show in the simplest form the way that the anisotropy changes across a shock. Contact discontinuities have also not been found; their discovery would tell us something about the diffusion of particles along $\underset{\sim}{B}$. The origin of all types of discontinuities (except some of the fast shocks, which are caused by solar flares) is one of the outstanding problems. The mutual interaction of discontinuities and the intersections of discontinuities is just beginning to be studied. The structure of discontinuities is an important subject which can only be studied by multiple

spacecraft observations with high time resolution instruments; it is not clear to what extent this problem can be treated by the MHD approximation.

The study of waves is in a somewhat less satisfactory state. Alfven waves have been identified with some certainty, but their propagation speed and the dispersion relation have not been measured. It is not clear whether or not an acoustic wave can propagate along $\underset{\sim}{B}$. The existence of slow shocks in the solar wind and the theory of ion acoustic waves in a collisionless plasma indicate that acoustic waves do exist in the solar wind, but they have not been measured directly and there are theories which suggest that particle motions parallel to B are not strongly coupled, in which case acoustic waves could not propagate. Sinusoidal, compressional oscillations have been observed, which may be magneto-acoustic waves, but more precise density and velocity measurements will be needed to positively identify such waves. Evidence for the fast magneto-acoustic mode, propagating anisotropically as predicted by MHD and particle orbit theory, has been found in the lunar Mach cone. However, it has not been established that the corresponding slow mode can propagate. Future studies of flow past some of the outer planets will be especially significant in this regard if the solar wind becomes transonic or subsonic there and retains its characteristics as a hydromagnetic fluid. The firehose instability has often been discussed in reference to the solar wind, but its existence has not been firmly established. It is clear, however, that the instability is not as universal as some authors have suggested. More work needs to be done in this area.

The experimental results which we have reviewed show without doubt that hydromagnetic theory is applicable to the solar wind. Many of the consequences of this theory remain to be worked out. Nonlinear theories of waves, instabilities, and interaction of discontinuities and waves are particularly needed. One would also hope for future developments and solar wind applications of the MHD theory of turbulence, boundary layers, and flows past obstacles. Experimentally, the need is for higher time resolution, greater precision and simultaneous measurements of $\underset{\sim}{B}$ and the distribution functions of protons, α's and electrons from at least 2 space probes.

ACKNOWLEDGMENTS

The author is indebted to many colleagues for helpful discussions. The discussions with Drs. Y. C. Whang and K. W. Ogilvie were particularly illuminating. Dr. Ogilvie helped in several other ways; he collaborated in many of the investigations reviewed here, he examined the details of the manuscript, and he contributed the summary of experimental results in Section II.

REFERENCES

Abraham-Shrauner, B. J.: 1967, Plasma Physics 3, 361.

Alfven, H.: 1943, Arkiv Mat. Astron. Fysik, 29B, 1.

Axford, W. I.: 1968, Space Sci. Rev. 8, 331.

Bame, S. J., Asbridge, J. R., Hundhausen, A. J., and Montgomery, M. D.: 1970, J. Geophys. Res., 75, 6360.

Belcher, J. W., and Davis, L., Jr.: 1971, J. Geophys. Res., (in press).

Belcher, J. W., Davis, L., Jr., and Smith, E. J.: 1969, J. Geophys. Res. 74, 2302.

Boyd, T. J. M., and Sanderson, J. J.: 1969, "Plasma Dynamics," Barnes and Noble, Inc., (New York).

Burgess, J. M.: 1960, in "Symposium of Plasma Dynamics," ed. F. H. Clauser, Addison-Wesley (Reading, Mass.)

Burlaga, L. F.: 1968, Solar Physics 4, 67.

Burlaga, L. F.: 1969a, Solar Physics 7, 54.

Burlaga, L. F.: 1969b: Solar Physics 7, 72.

Burlaga, L. F.: 1970, Cosmic Electrodynamics 1, 233.

Burlaga, L. F.: 1971, NASA-GSFC X-692-71-74, submitted to Solar Physics.

Burlaga, L. F., and Ness, N. F.: 1968, Canadian Journal of Physics 46, S 962.

Burlaga, L. F., and Ness, N. F.: 1969, Solar Physics 9, 467.

Burlaga, L. F., and Ogilvie, K. W.: 1970, Solar Physics 15, 61.

Burlaga, L. F., Ogilvie, K. W., and Fairfield, D. H.: 1969, Astrophys. J. 155, L171.

Burlaga, L. F., Ogilvie, K. W., Fairfield, D. H., Montgomery, M. D., and Bame, S. J.: 1971, Astrophysical J. 164 (in press).

Chandrasekhar, S.: 1960, "Plasma Physics," Notes computed by S. K. Trehan. The University of Chicago Press (Chicago).

Chao, J. K.: 1970, MIT Technical Document CSR TR-70-3 (thesis).

Chao, J. K., and Binsack, J.: 1971, submitted to J. Geophys. Res.

Chao, J. K., and Olbert, S.: 1970, J. Geophys. Res. 75, 6394.

Chew, G. F., Goldberger, M. L., and Low, F. E.: 1956, Proc. Roy. Soc. (London) A236, 112.

Colburn, D. S., and Sonett, C. P.: 1966, Space Sci. Rev. 5, 439.

Coleman, P. J., Jr.: 1966, Phys. Rev. Letters 17, 207.

Coleman, P. J., Jr.: 1967, Planet. Space Sci. 15, 953.

Eviatar, A., and Schulz, M.: 1970, Planet. Space Sci. 18, 321.

Fredericks, R. W., and Scarf, F. L.: 1965, J. Geophys. Res. 70, 4765.

Grad, H., and Rebhan, E.: 1969, Phys. Rev. Letters 22, 451.

Greenstadt, E. W., Green, I. M., Inotuye, G. T., and Sonett, C. P.: 1970, Planet. Space Sci. 18, 333.

Hudson, P. D.: 1970, Planet. Space Sci. 18, 1611.

Hundhausen, A. J.: 1968, Space Sci. Rev. 8, 690.

Hundhausen, A. J.: 1970, Reviews of Geophysics and Space Physics 8, 729.

Hundhausen, A. J., Bame, S. J., Asbridge, J. R., and Sydoriak, S. J.: 1970, J. Geophys. Res. 75, 4631.

Hundhausen, A. J., and Montgomery, M. D.: 1971, J. Geophys. Res. 76, 2236.

Ivanov, K. G.: 1970, Akademiya nauk SSSR, in press.

Jeffrey, A., and Taniuti, T.: 1964, "Non-linear Wave Propagation," Academic Press (New York).

Kawashima, N.: 1969, J. Geophys. Res. 74, 225.

Kennel, C. F., and Scarf, F. L.: 1968, J. Geophys. Res. 73, 6149.

Lepping, R. P., and Argentiero, P. D.: 1971, J. Geophys. Res., in press.

Lust, R.: 1959, Fortschritte der Physik 7, 503.

Lynn, Y. M.: 1967, Phys. Fluids 10, 2278.

Michel, F. C.: 1967, J. Geophys. Res. 72, 1917.

Ness, N. F., Scearce, C. S., and Cantarano, S.: 1966, J. Geophys. Res. 71, 3305.

Neubauer, F. M.: 1970, Z. Physik 237, 205.

Neugebauer, Marcia, and Snyder, C. W.: 1967, J. Geophys. Res., 72, 1823.

Northrop, T. G., and Birmingham, T. J.: 1970, Solar Physics 14, 226.

Ogilvie, K. W.: 1970 Summer Institute for Astronomy and Astrophysics, Stoney Brook, to be published.

Ogilvie, K. W., and Burlaga, L. F.: 1969, Solar Physics 8, 422.

Ogilvie, K. W., Burlaga, L. F., and Wilkerson, T. D.: 1968, J. Geophys. Res. 73, 6809.

Parker, E. N., 1963, Interplanetary Dynamical Processes (New York: Interscience).

Parker, E. N.: 1957, Phys. Res. 107, 924.

Quenby, J. F., and Sear, S. F.: 1970 (to appear in Planet. Space Sci.)

Robbins, D. E., Hundhausen, A. J., and Bame, S. J.: 1970, J. Geophys. Res. 75, 1178.

Scarf, F. L., Wolfe, J. H., and Silva, R. W.: 1967, J. Geophys. Res. 72, 993.

Scarf, F. L.: 1970, Space Sci. Rev. 11, 234.

Serrin, J.: 1959, Handbuch der Physic 8/1, 125. ed. S. Flugge, Springer-Verlag (Berlin).

Siscoe, G. L., Davis, L., Jr., Coleman, P. J., Jr., Smith, E. J., and Jones, D. E.: 1968, J. Geophys. Res. 73, 61.

Smith, E. J., Belcher, J., and Davis, L., Jr., and Coleman, P. J., Jr.: 1970, EOS 51, 412.

Sonnett, C. P., Colburn, D. S., Davis, L., Jr., Smith, E. J., and Coleman, P. J., Jr. 1964, Phys. Rev. Letters 13, 153.

Spreiter, J. R., and Alksne, A. Y.: 1969, Reviews of Geophysics 7, 11.

Turner, J. M., and Siscoe, G. L.: 1971, J. Geophys. Res. 76, 1816.

Unti, T. W., and Neugebauer, M.: 1968, Phys. Fluids 11, 563.

Vasyliunas, V. M.: 1971 in "Methods of Experimental Physics," 9B (Plasma Physics), ed. R. H. Lovberg, Academic Press (New York).

Whang, Y. C.: 1970, Solar Physics 14, 489.

Whang, Y. C.: 1971, Phys. Fluids (in press).

Whang, Y. C., and Ness, N. F.: 1970, J. Geophys. Res. 75, 6002.

Wilkerson, T. D.: 1969, Solar Physics 6, 44.

Wolfe, J. H., and Intrilligator, D. S.: 1970, Space Sci. Rev. 10, 511.

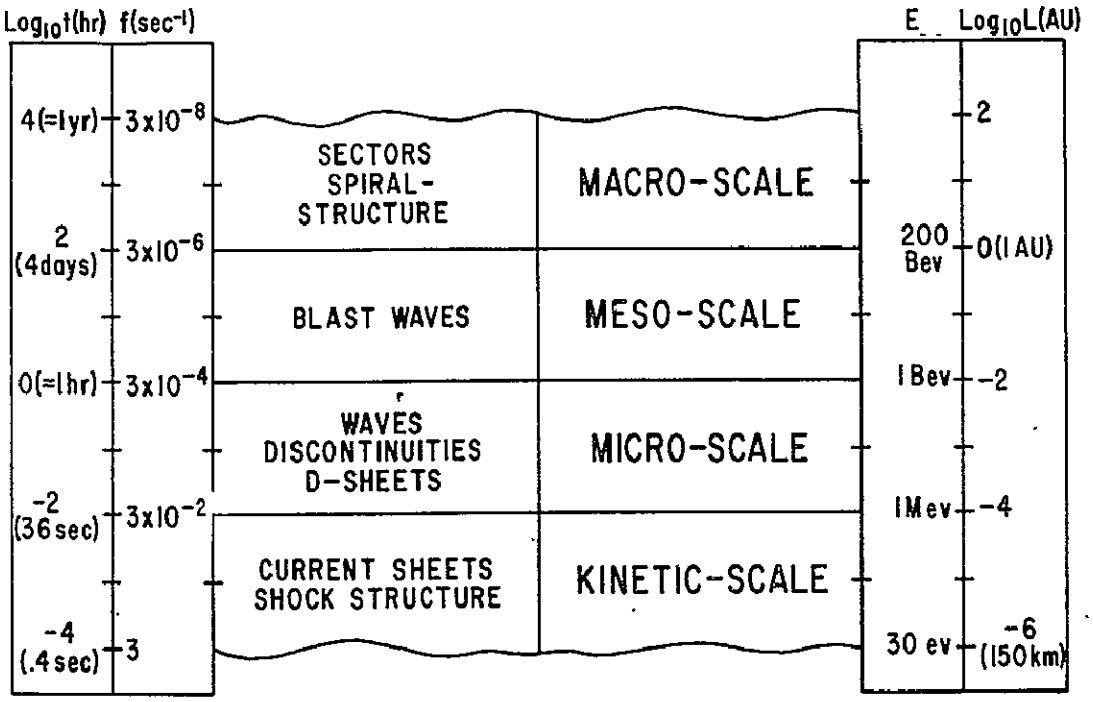

Figure 1. This defines the scales in terms of characteristic times, frequencies, and lengths. Some characteristic features seen on the different scales are shown. E is the energy of a proton whose gyro radius is the scale length in a 5 γ field.

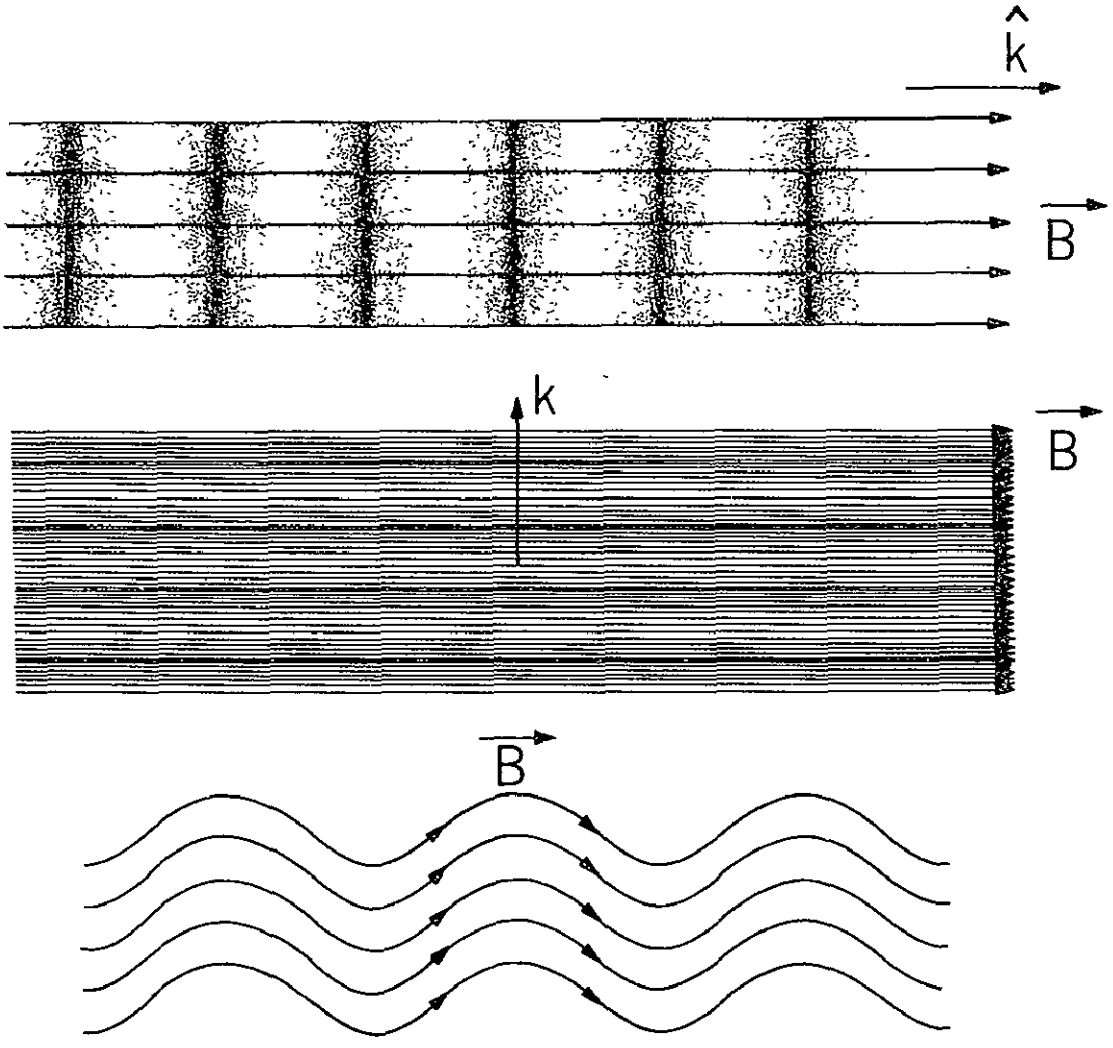

Figure 2. The 3 basic waves in a compressible, hydromagnetic fluid. Top: longitudinal, acoustic wave. Middle: magneto acoustic wave. Bottom: Alfven wave.

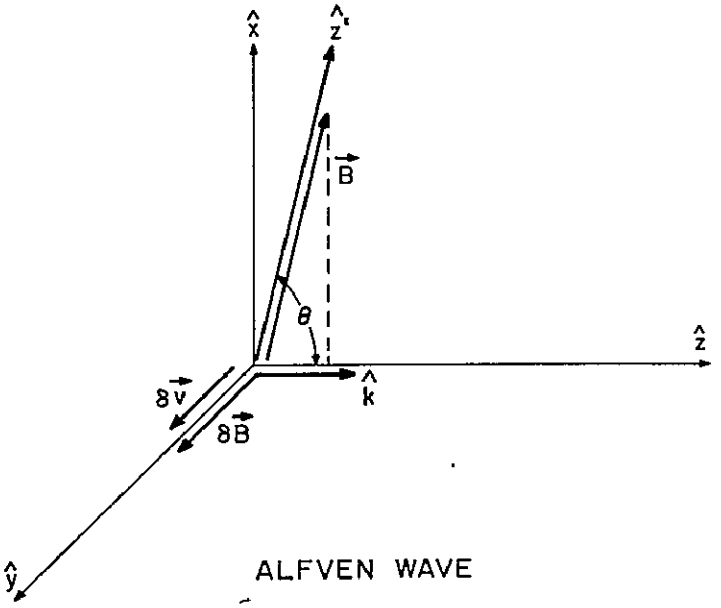

Figure 3. Alfven wave. The perturbations $\delta\underset{\sim}{v}$ and $\delta\underset{\sim}{B}$ are perpendicular to $\hat{k}$ and $\underset{\sim}{B}$

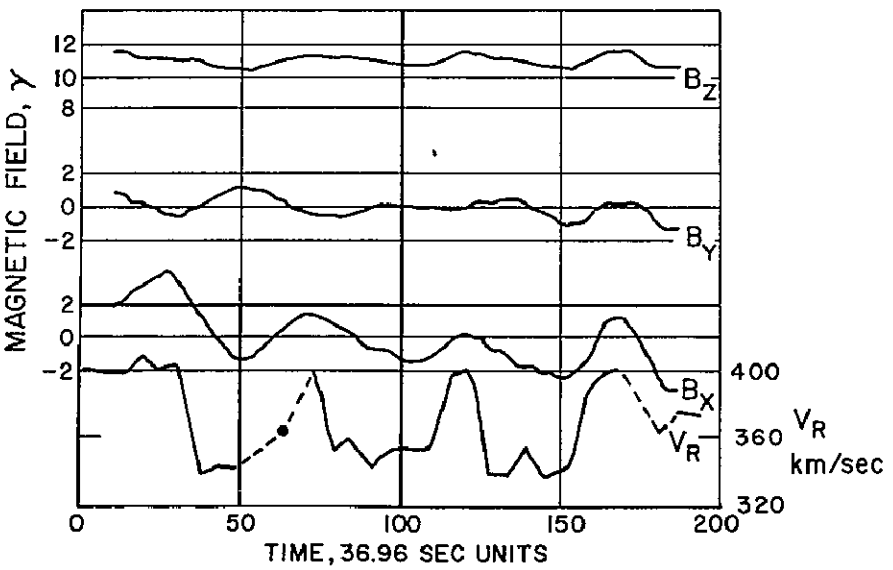

Figure 4. Observations of an Alfven wave. This shows a nearly periodic wave form with a strong correlation between the radial component of the bulk speed (V_R) and the radial component of $\underset{\sim}{B}$ (Bx).

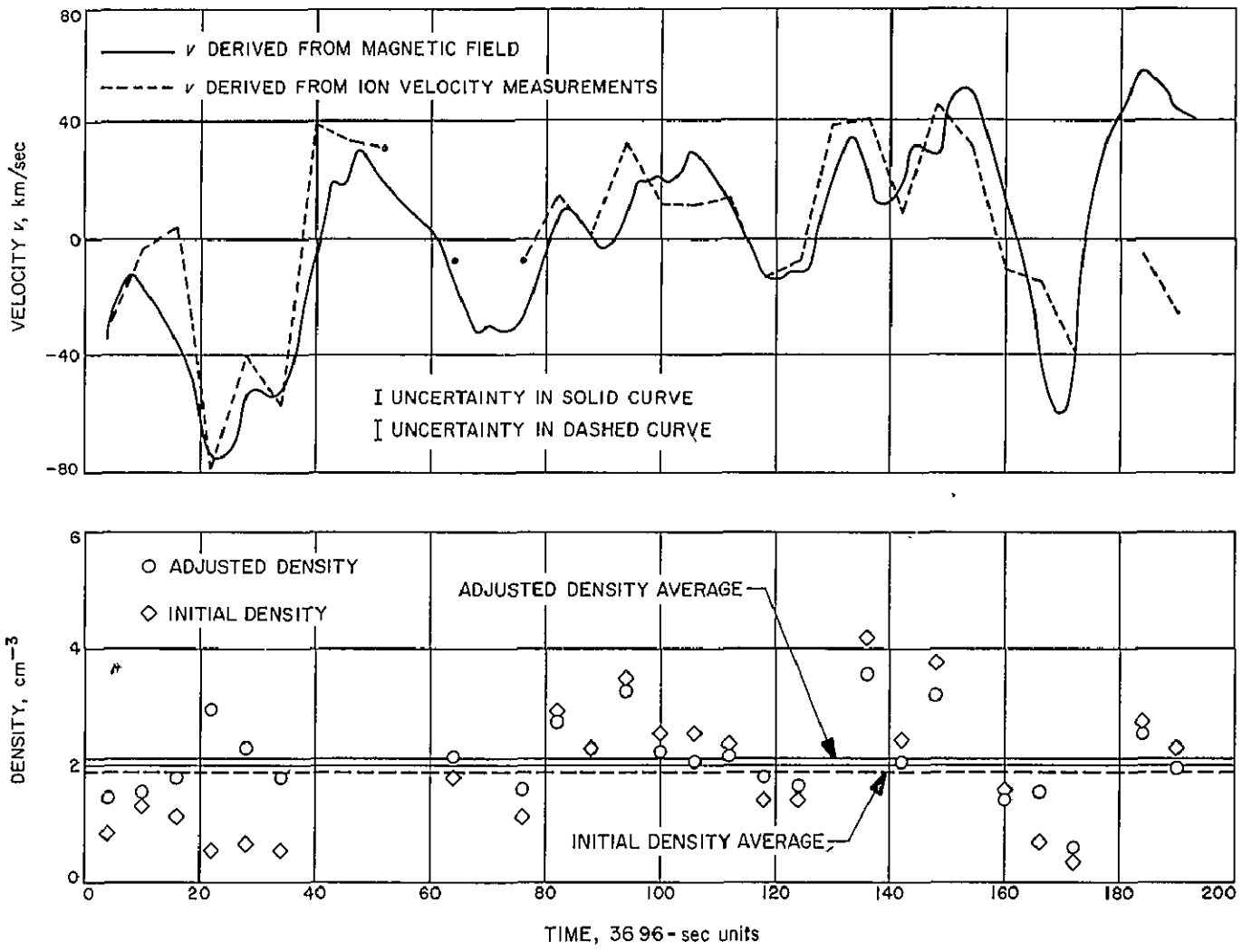

Figure 5. Alfven wave. The observed velocity and that computed from $\tilde{B}$ assuming an Alfven wave for the wave in Fig. 4 are in good agreement. The corrected density is constant, as required for an Alfven wave.

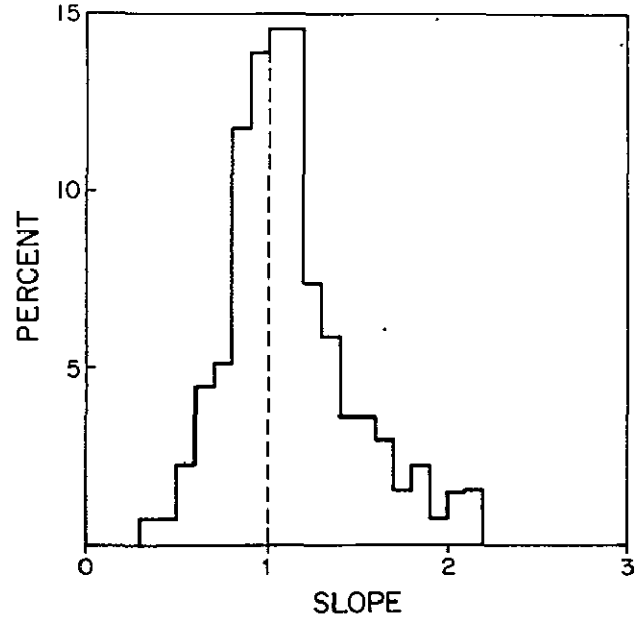

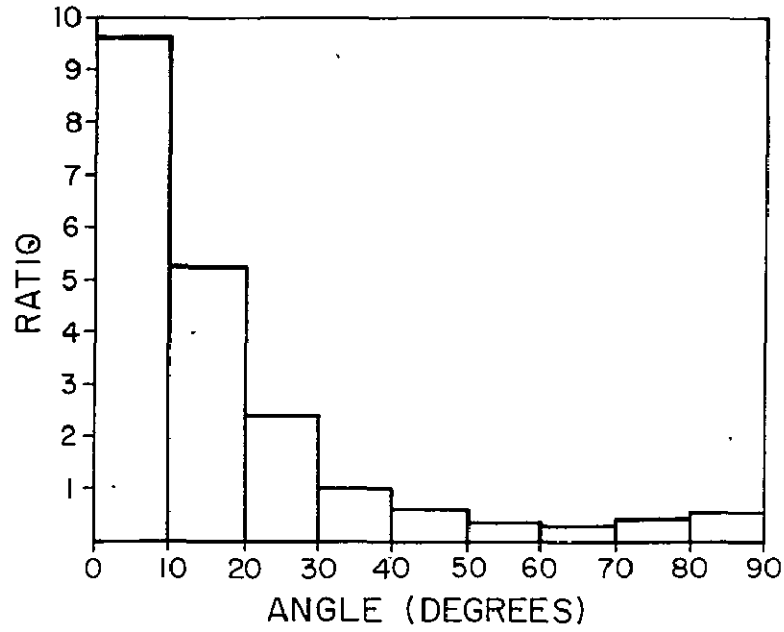

Figure 6. Observations of non-linear, a periodic Alfven waves by Belcher et al. These waves have the expected proportionality constant between $\delta \underset{\sim}{v}$ and $\delta \underset{\sim}{B}$ as indicated by the top distribution. The bottom distribution shows that they are transverse.

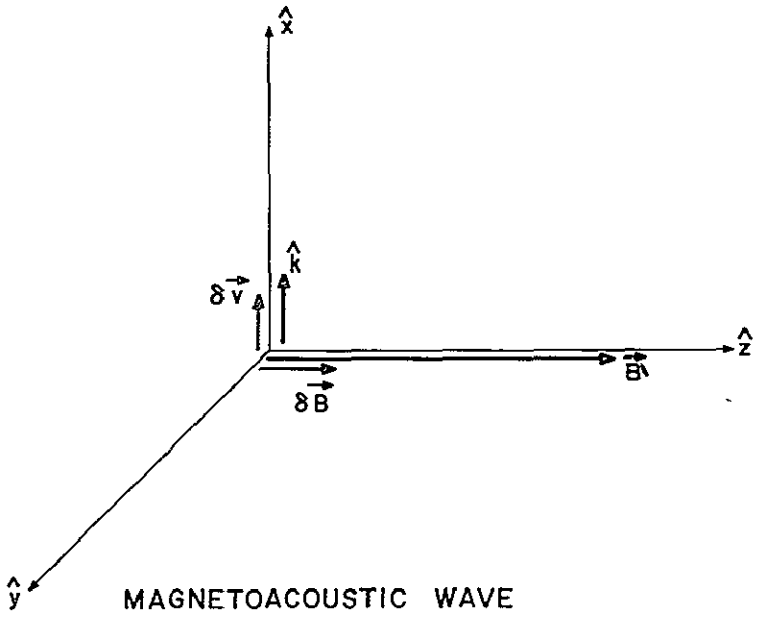

Figure 7. Magnetoacoustic Wave. This propagates normal to $\underset{\sim}{B}$. $\delta \underset{\sim}{v}$ is normal to $\underset{\sim}{B}$ and $\delta \underset{\sim}{B}$ is parallel to $\underset{\sim}{B}$.

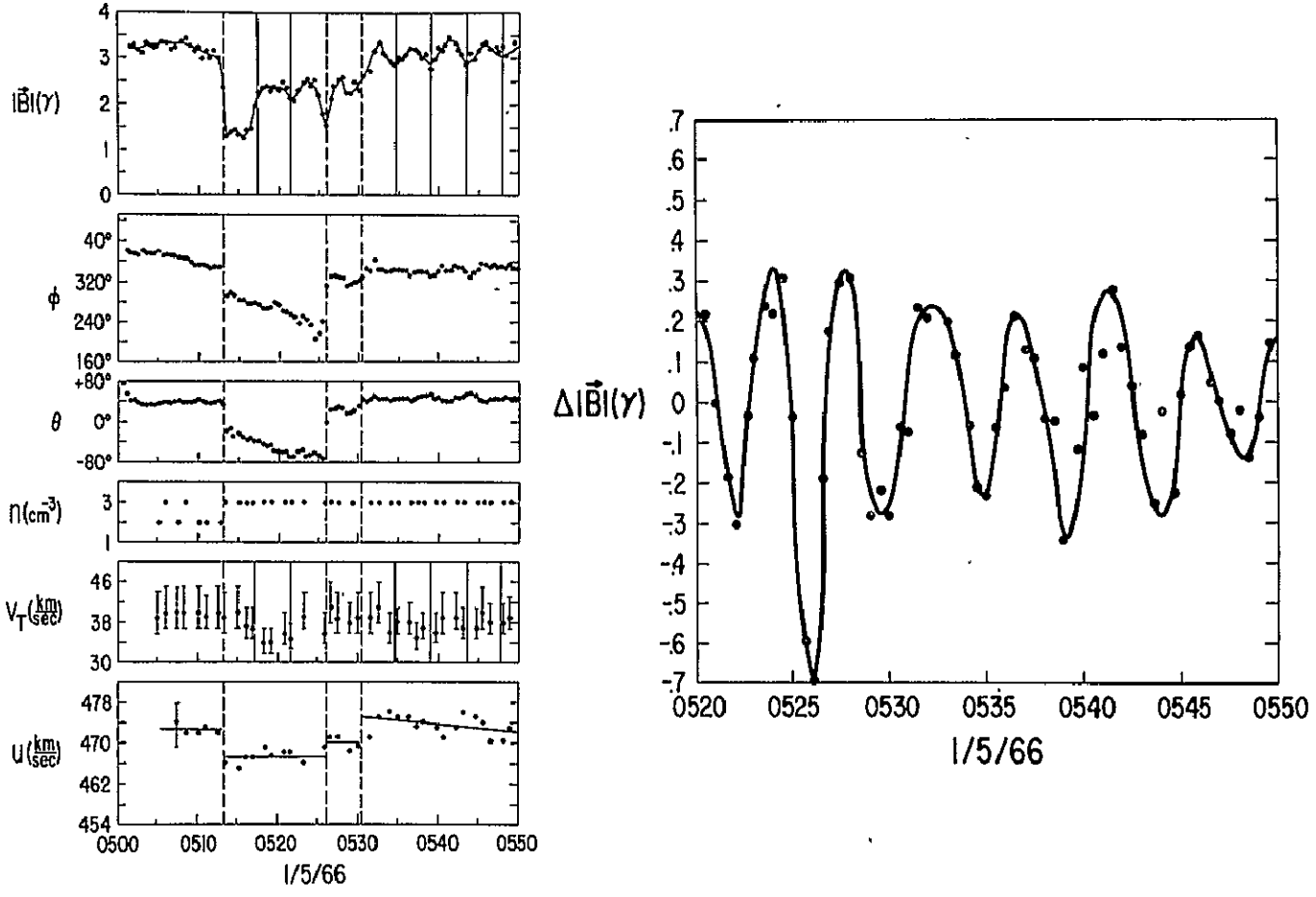

Figure 8. Observations of a compressional wave which is probably a magnetoacoustic wave. (See text).

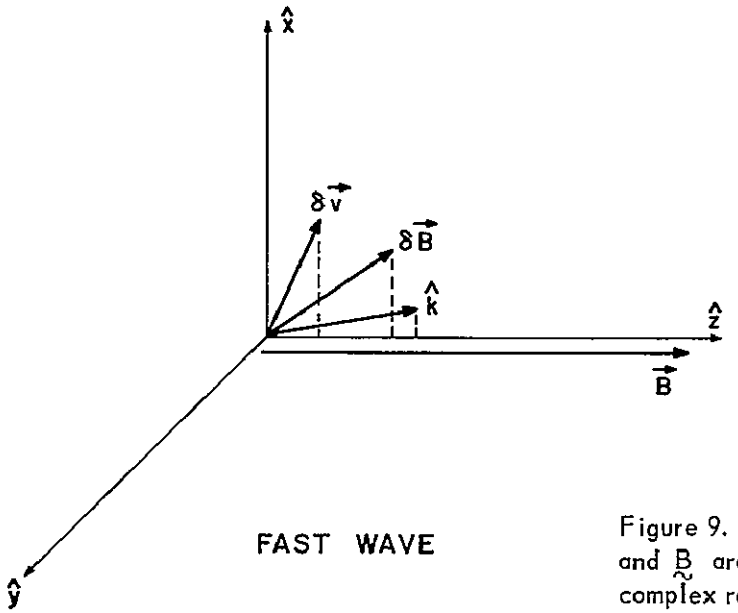

FAST WAVE

Figure 9. Fast wave. In this case, $\underset{\sim}{\delta B}$, $\delta \underset{\sim}{v}$, $\hat{k}$, and $\underset{\sim}{B}$ are coplanar, but there is generally a complex relation between them.

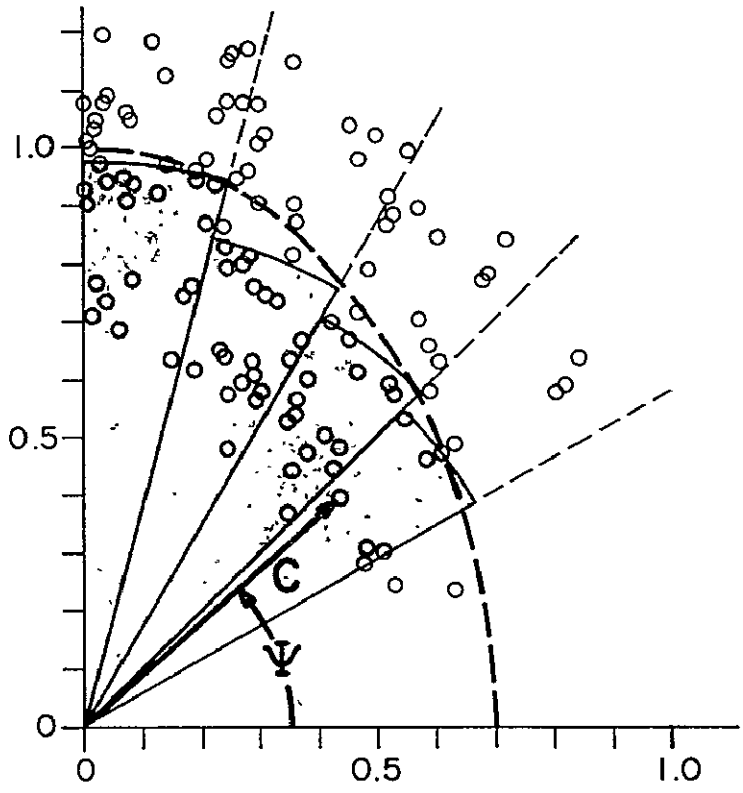

Figure 10. Observations of the fast wave. This shows the elliptical Mach cone behind the moon which is related to the fast wave (see text).

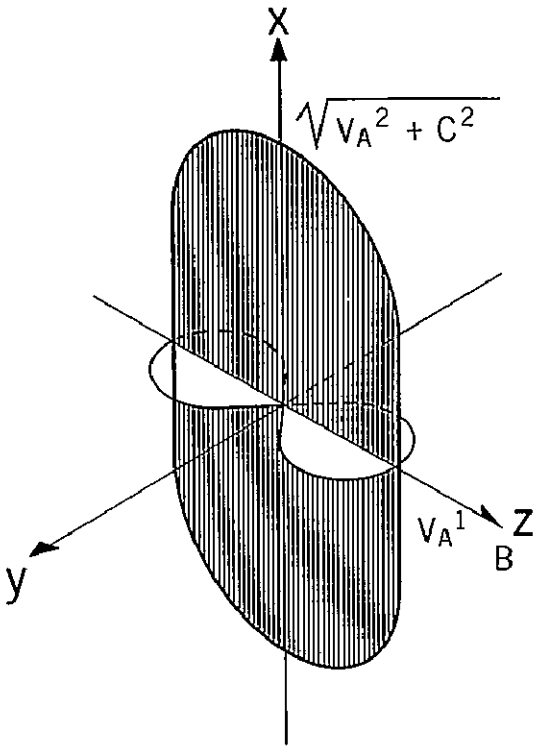

Figure 11. The elliptical fast wave and an Alfven wave.

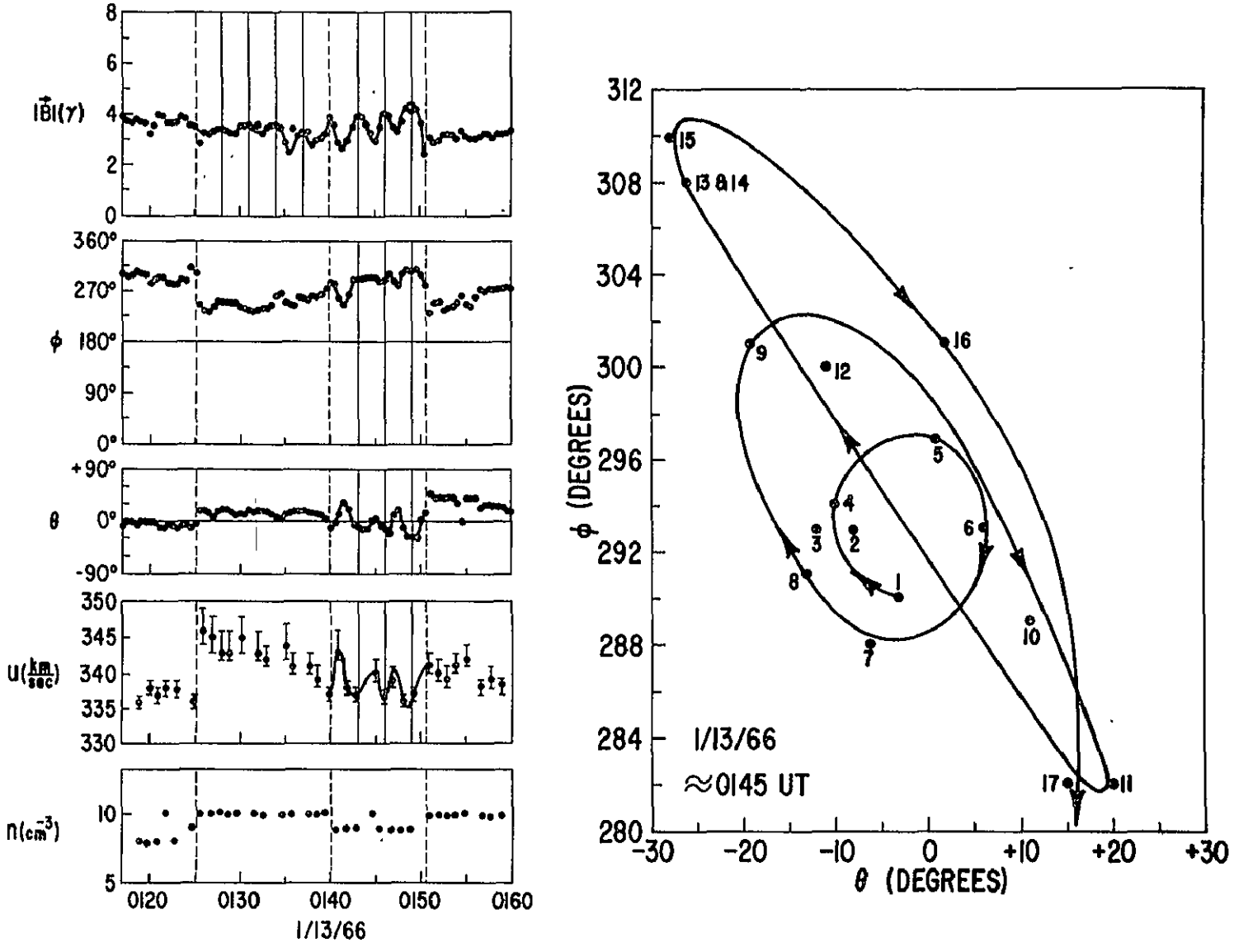

Figure 12. Observation of a fast wave. Periodic changes in both the magnitude and direction of $\underset{\sim}{B}$ are observed.

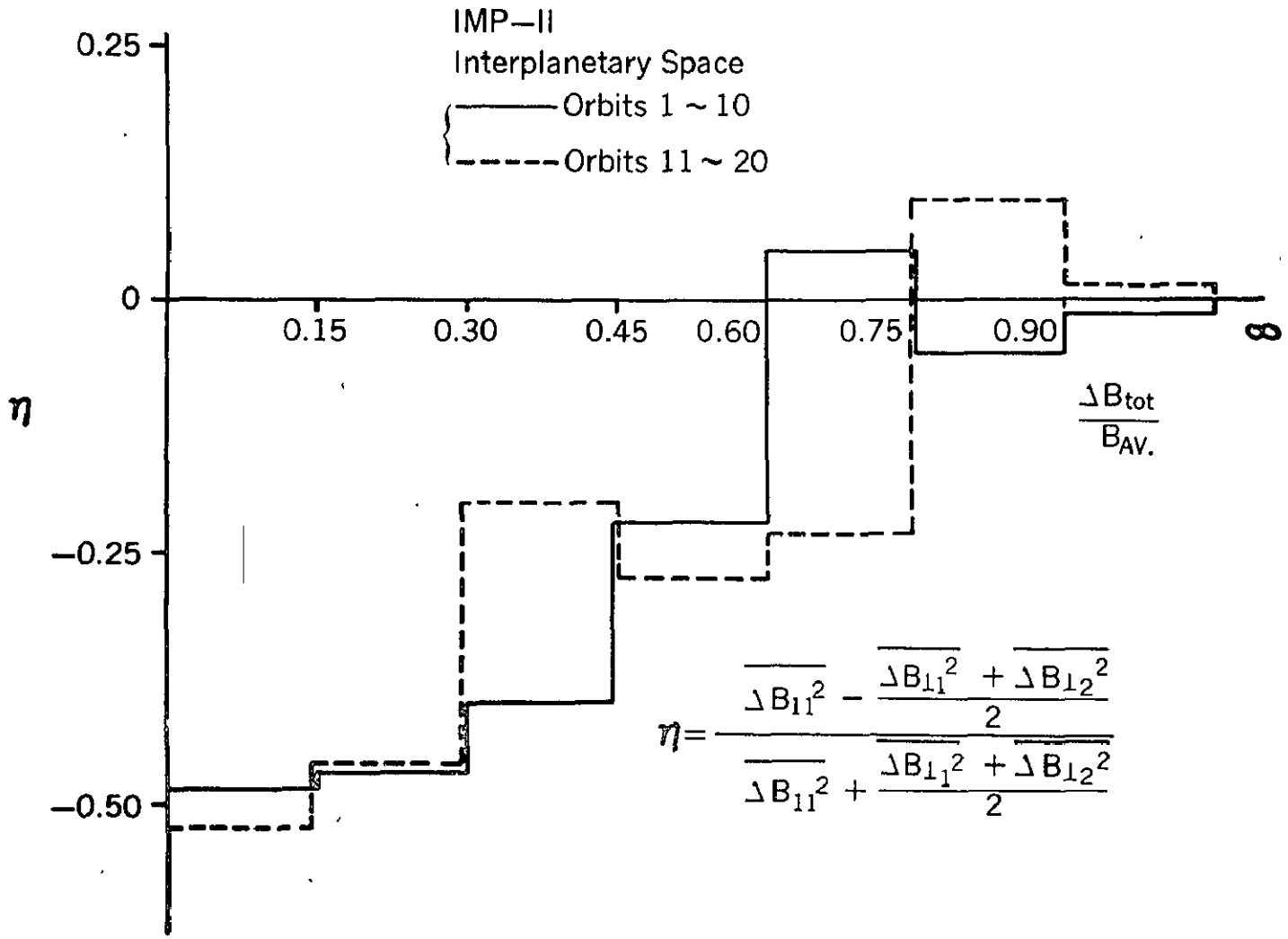

Figure 13. Evidence for coupling between fast and Alfven waves. This shows that the anisotropy of the magnetic fluctuations, measured by η, is smallest when the amplitude of the transverse and longitudinal fluctuations, measured by ΔB, is largest.

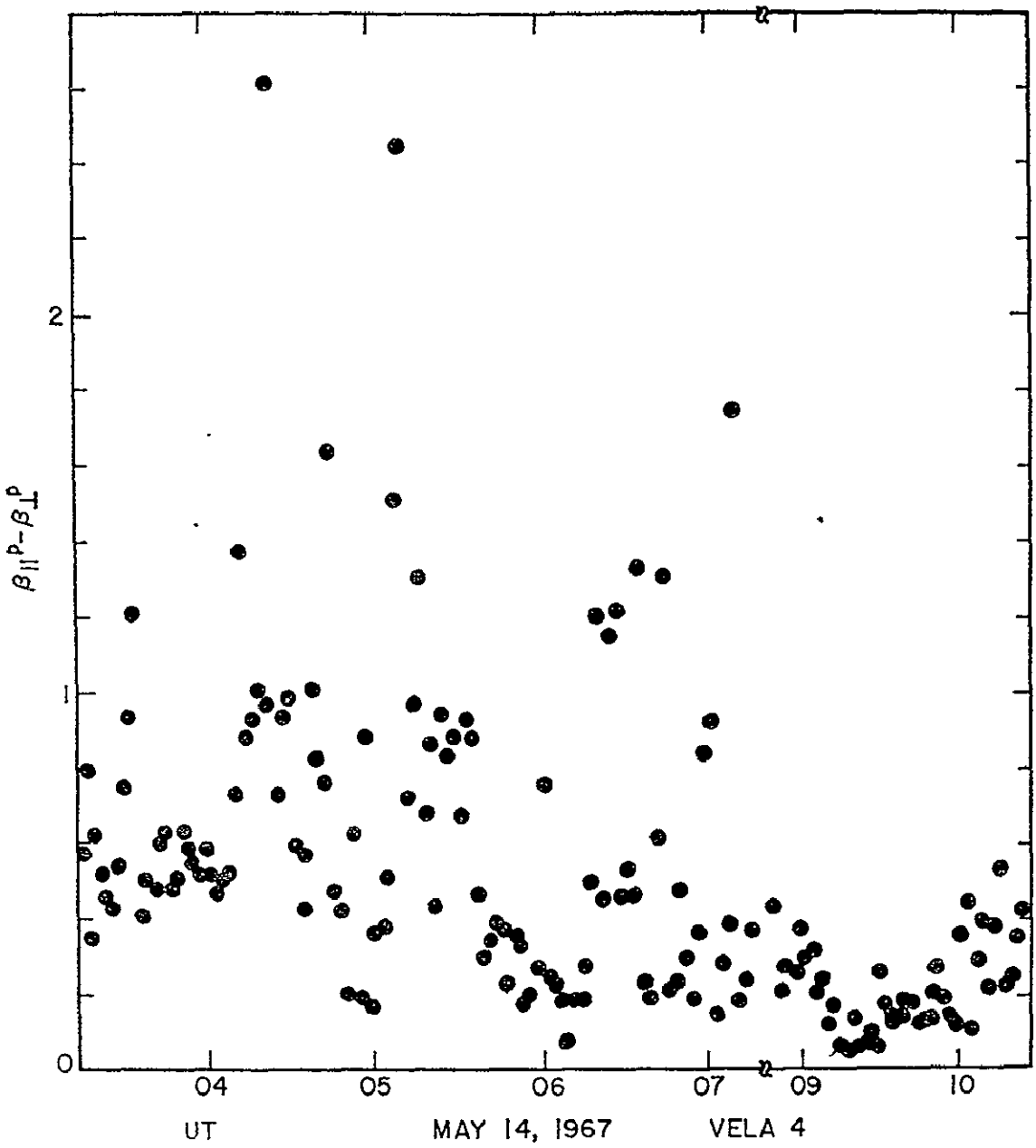

Figure 14. Test for firehose instability. The instability condition $\beta_{\parallel} - \beta_{\perp} > 2$ was not satisfied for the period shown here.

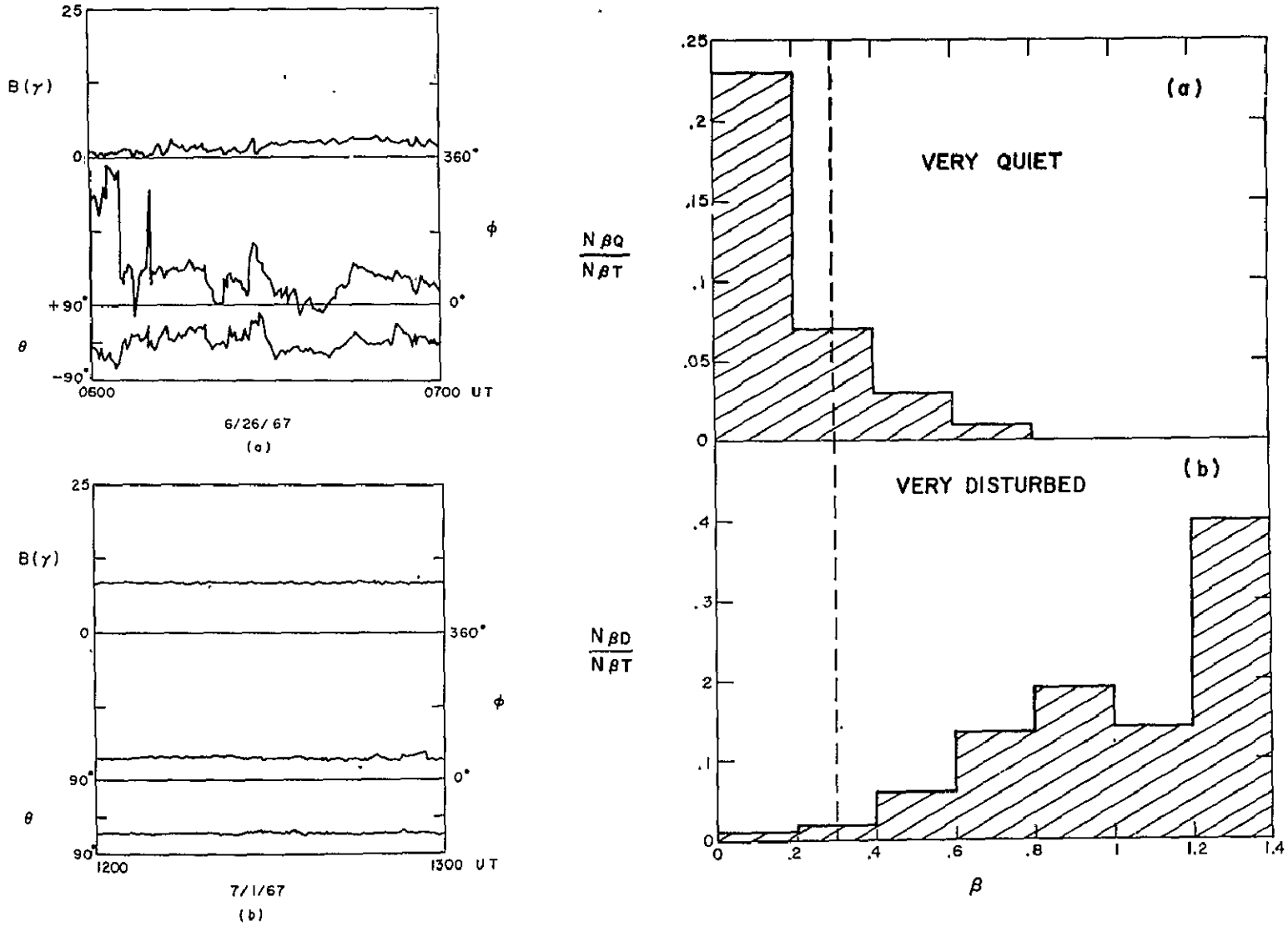

Figure 15. Microscale fluctuations (a) and a very quiet interval (b). The disturbed intervals are associated with high β, the very quiet intervals with low β.

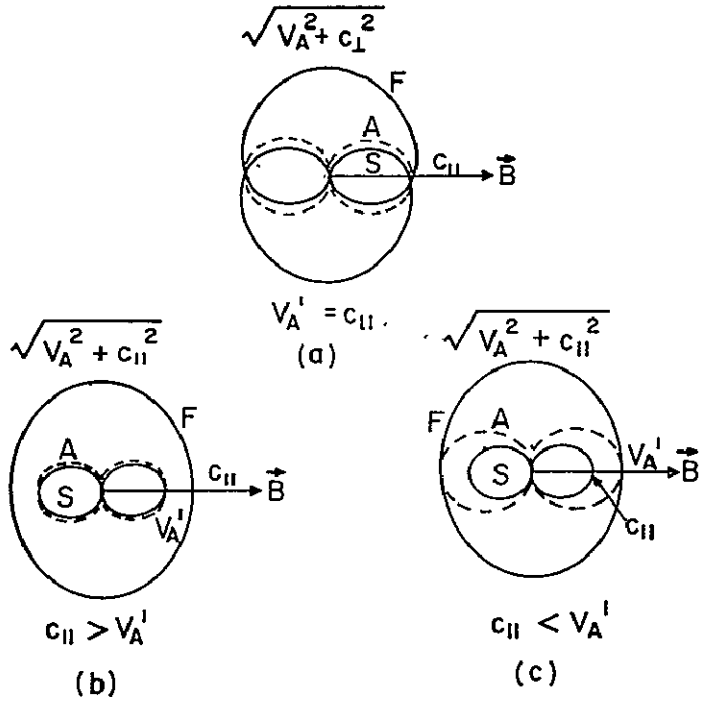

Figure 16. Surfaces of normal speeds for fast (F), slow (S) and Alfven modes (A).

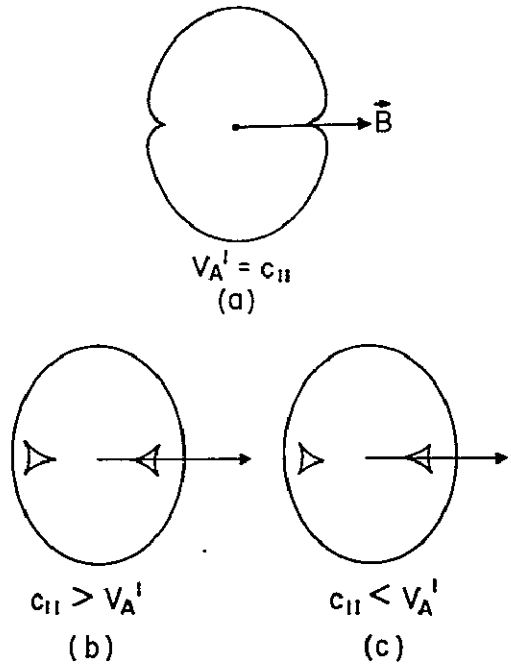

Figure 17. Wave fronts excited by a point source.

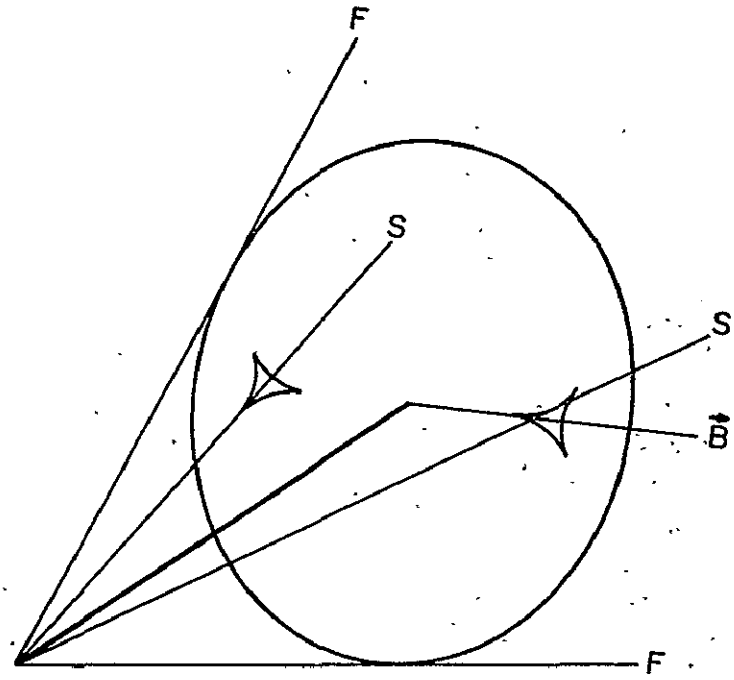

Figure 18. Construction of Mach cones. There is one cone for the fast mode and one for the slow mode. The heavy line is the fluid velocity. The "cones" are constructed by drawing tangents to the wave normal surfaces from this vector.

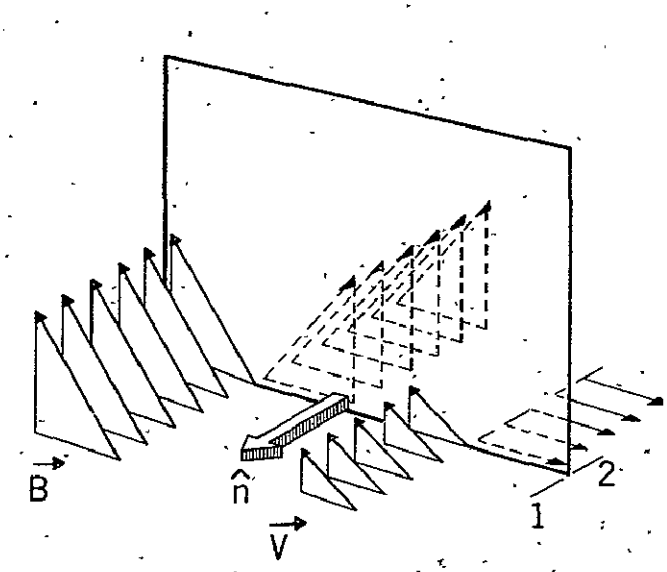

Figure 19. Tangential discontinuity. B is parallel to the surface of the discontinuity, but its direction may change across the surface.

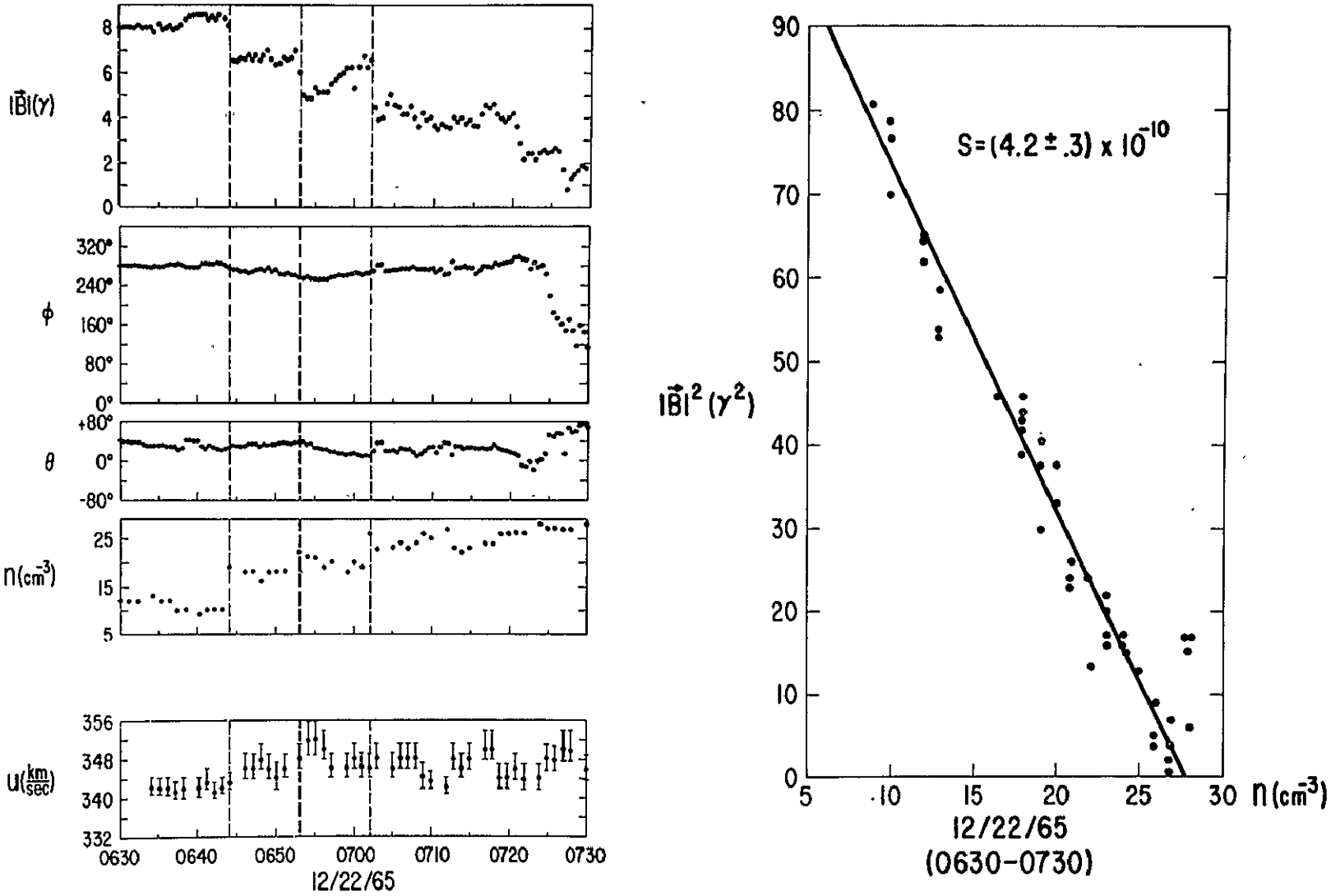

Figure 20. Observations of three tangential discontinuities. The discontinuities are indicated by the dashed lines. The proportionality between B^2 and n throughout the interval indicates that the pressure is constant and does not change across the discontinuities.

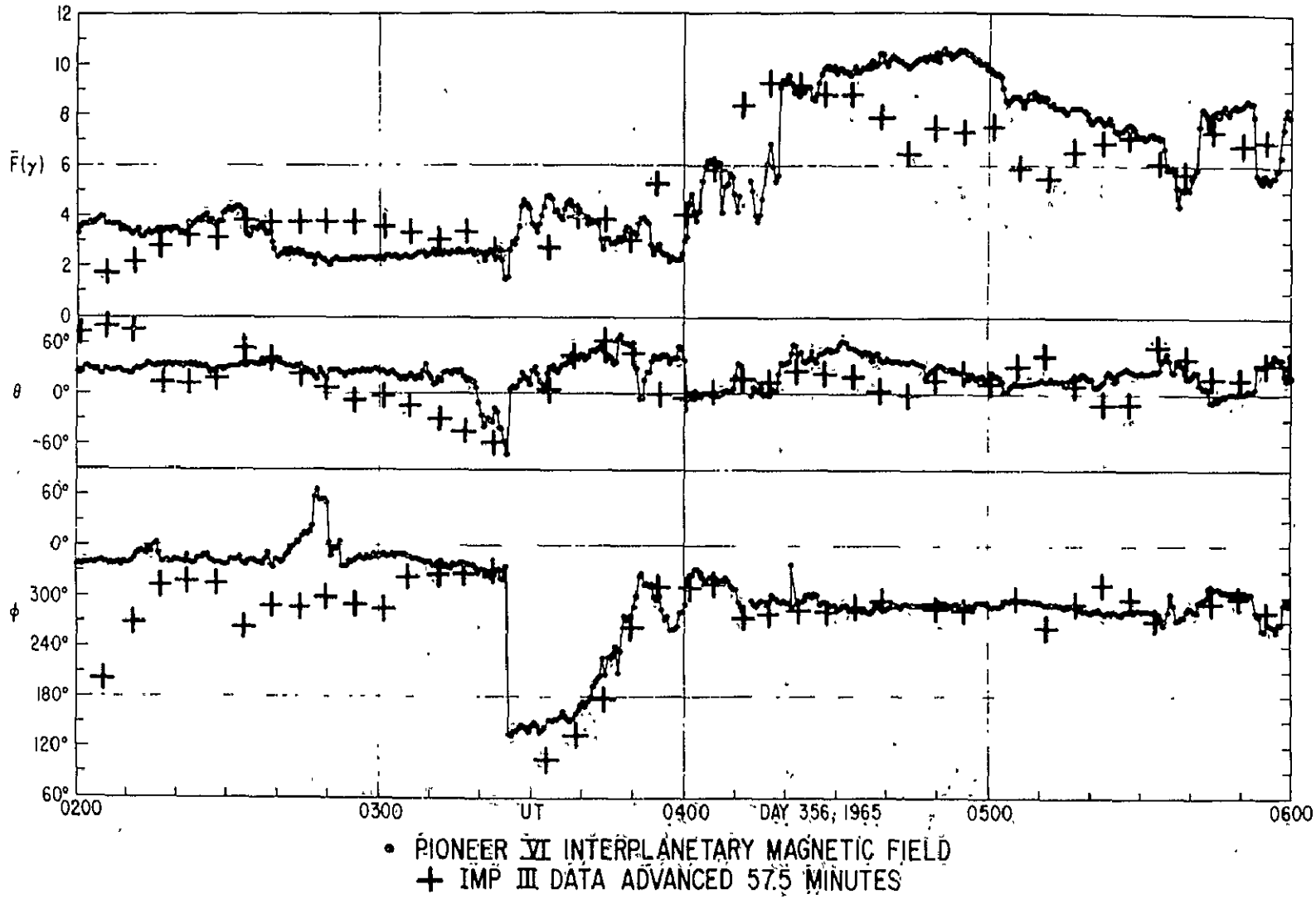

Figure 21. A tangential discontinuity observed at 2 widely separated spacecraft. One of the time series was shifted by 57.5 min, the delay predicted for the orientation computed assuming that the discontinuity at 0325 UT was tangential.

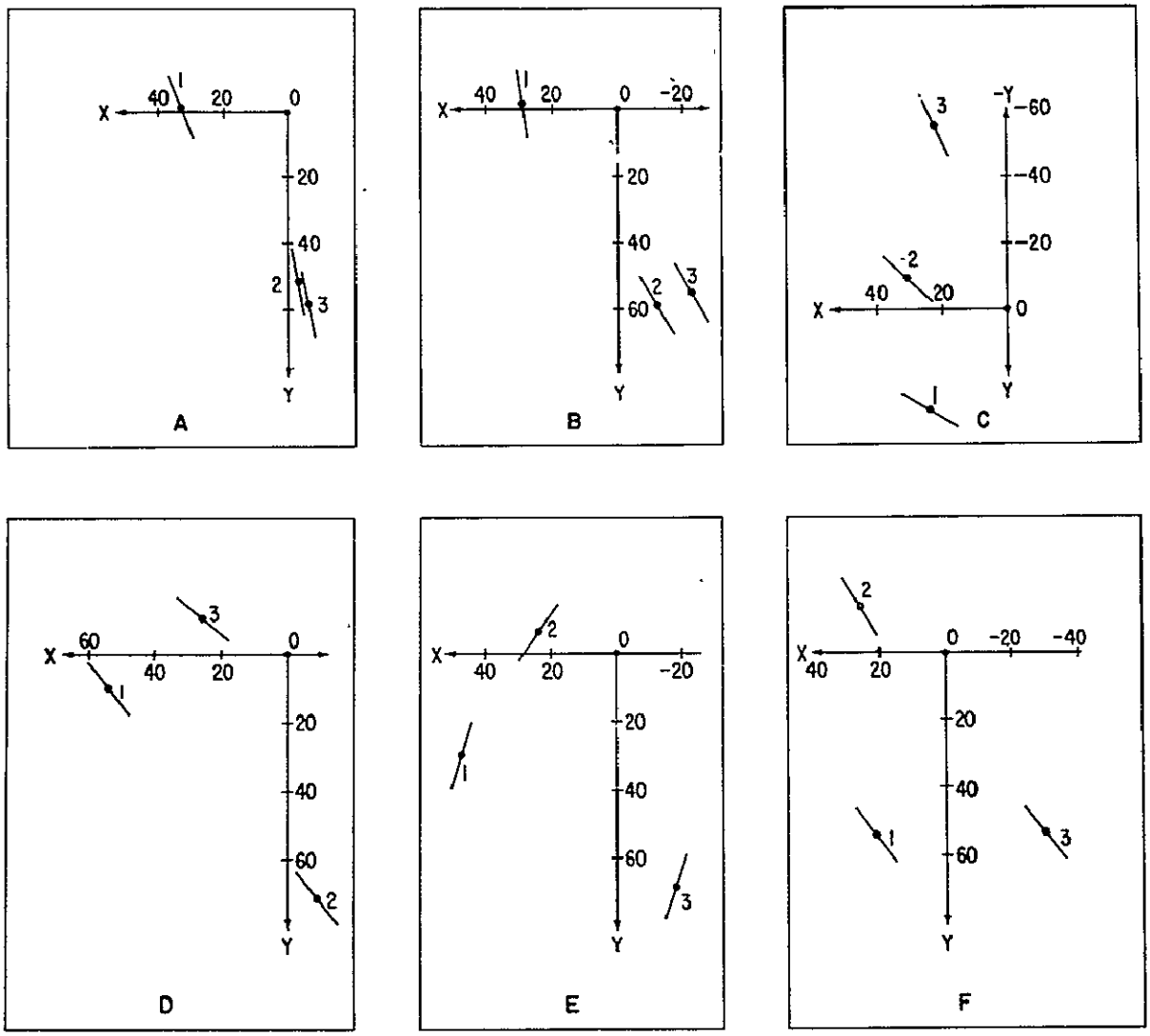

Figure 22. Multi satellite observations of discontinuities. Each panel represents one discontinuity. Each discontinuity (represented by a line segment) was seen at 3 spacecraft. The observed time delays are consistent with the orientations computed assuming that the discontinuities are tangential.

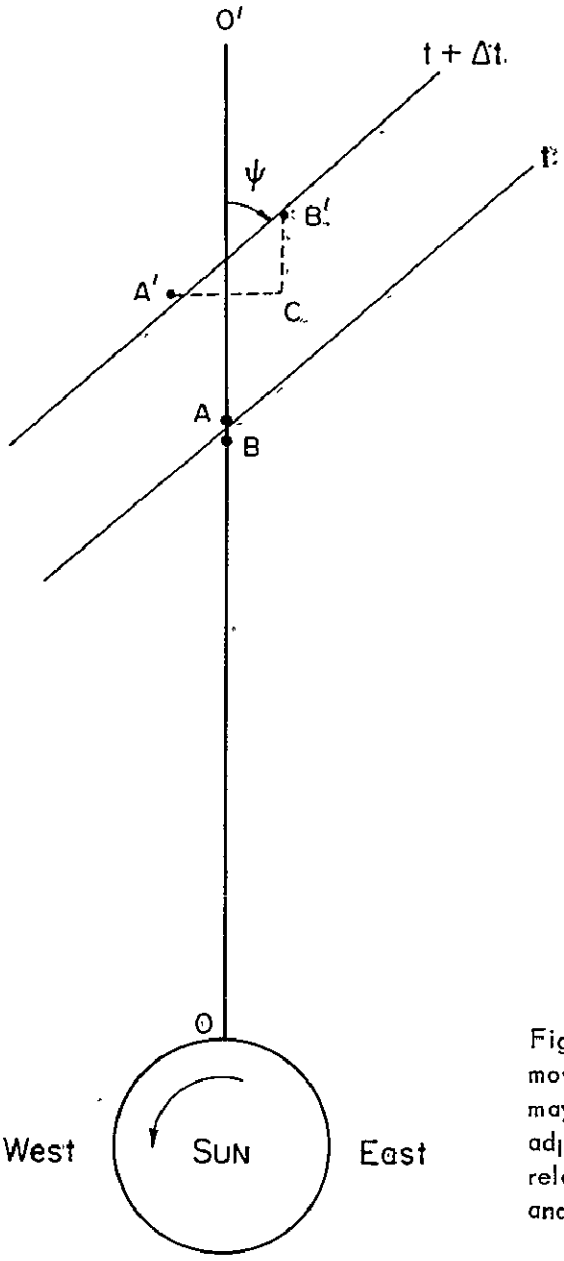

Figure 23 (a). A tangential discontinuity moves radially away from the sun. There may be a relative motion of the 2 regions adjacent to the surface, as indicated by the relative displacement of the points of A and B.

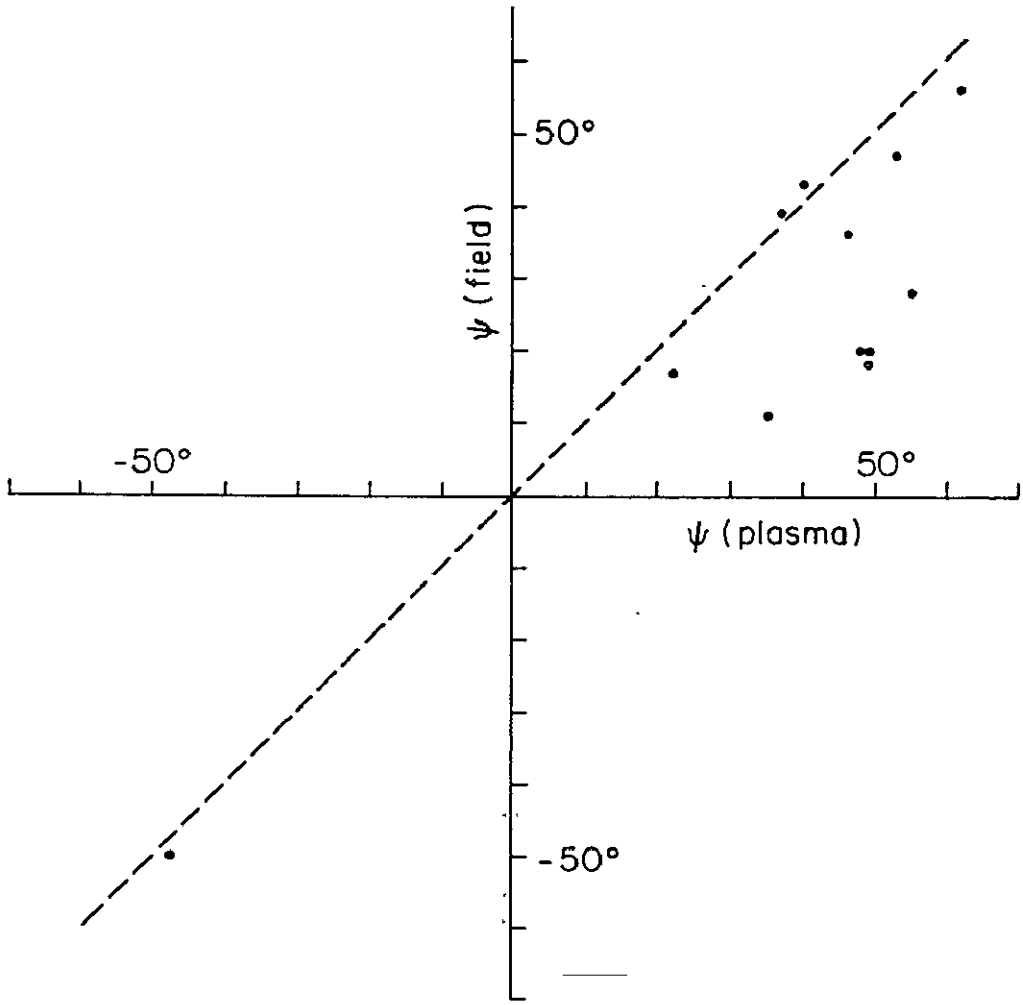

Figure 23 (b). For a tangential discontinuity the orientation may be computed from B and independently from v Observed discontinuities are shown by dots.

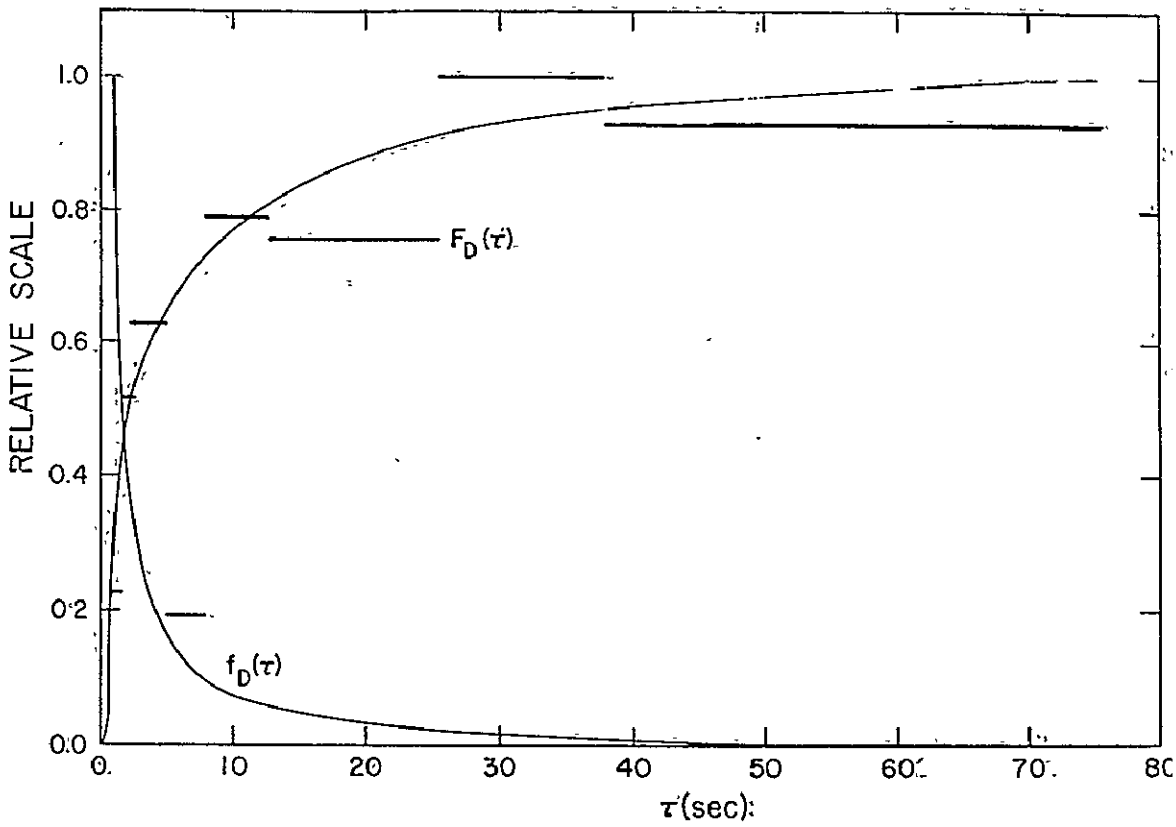

Figure 24. "Thickness" distribution ($f_D(t)$) of discontinuities. The actual thickness is on the order of the solar wind speed times τ. Most discontinuities tend to be very thin, and are distinct from waves.

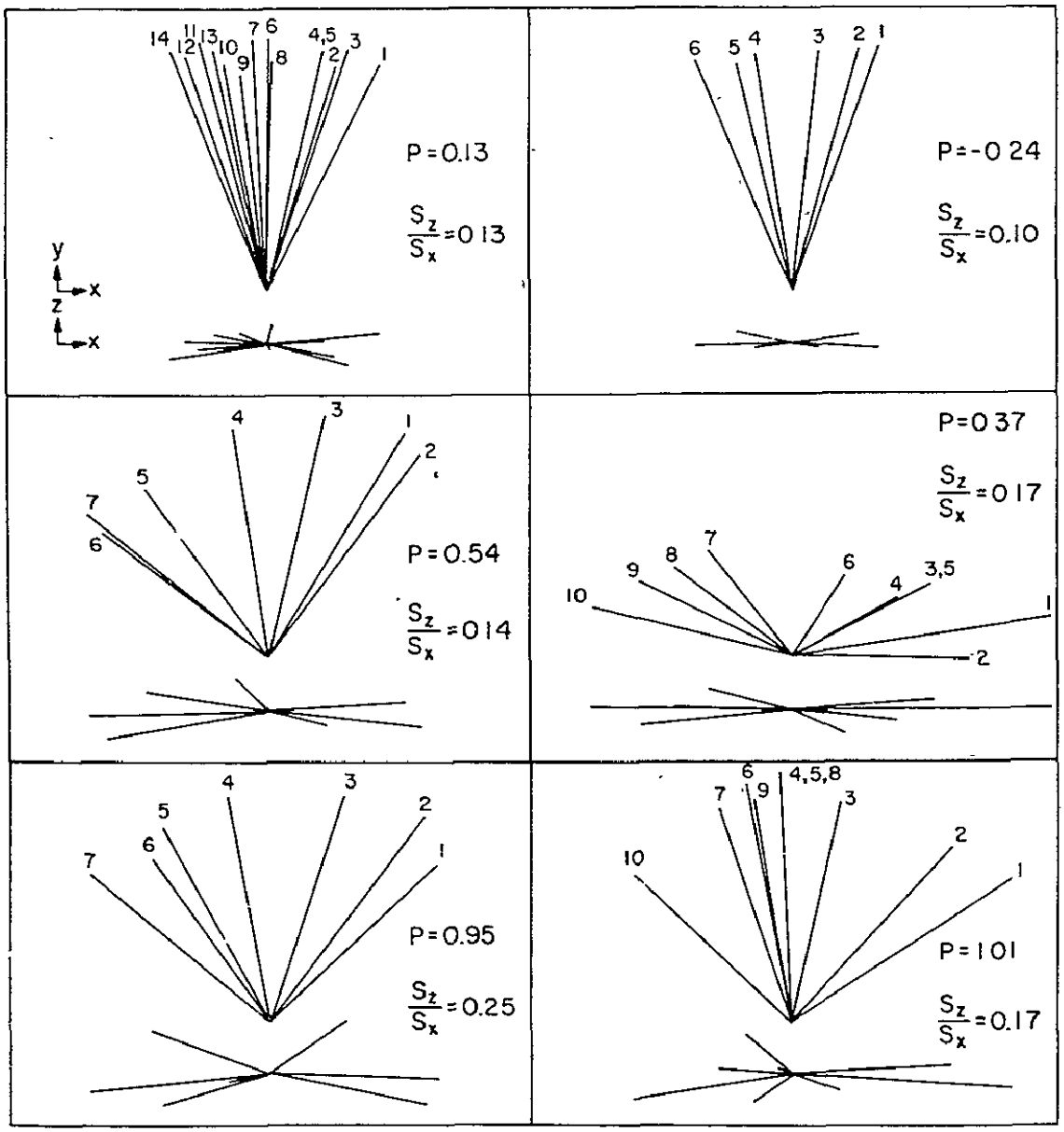

Figure 25. Current sheets associated with discontinuities. The magnetic field vectors tends to rotate in a plane as shown at the top of each panel. There are fluctuations out of this plane, as indicated at the bottom of each panel, but these are not statistically significant.

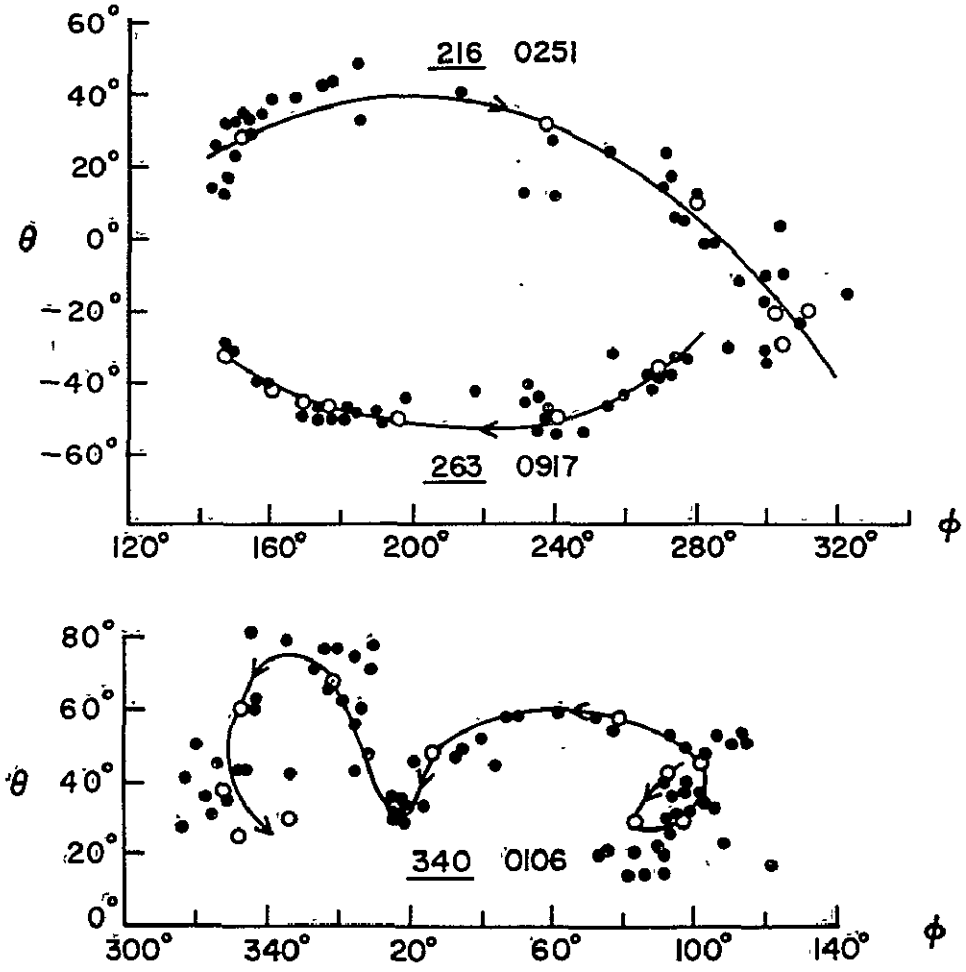

Figure 26. Laminar and "turbulent" current sheets. The top panel shows 2 current sheets on which the field rotated smoothly from its position on one side of the discontinuity to that on the other side. The bottom panel shows an irregular transition, suggesting a "turbulent" or unstable current sheet.

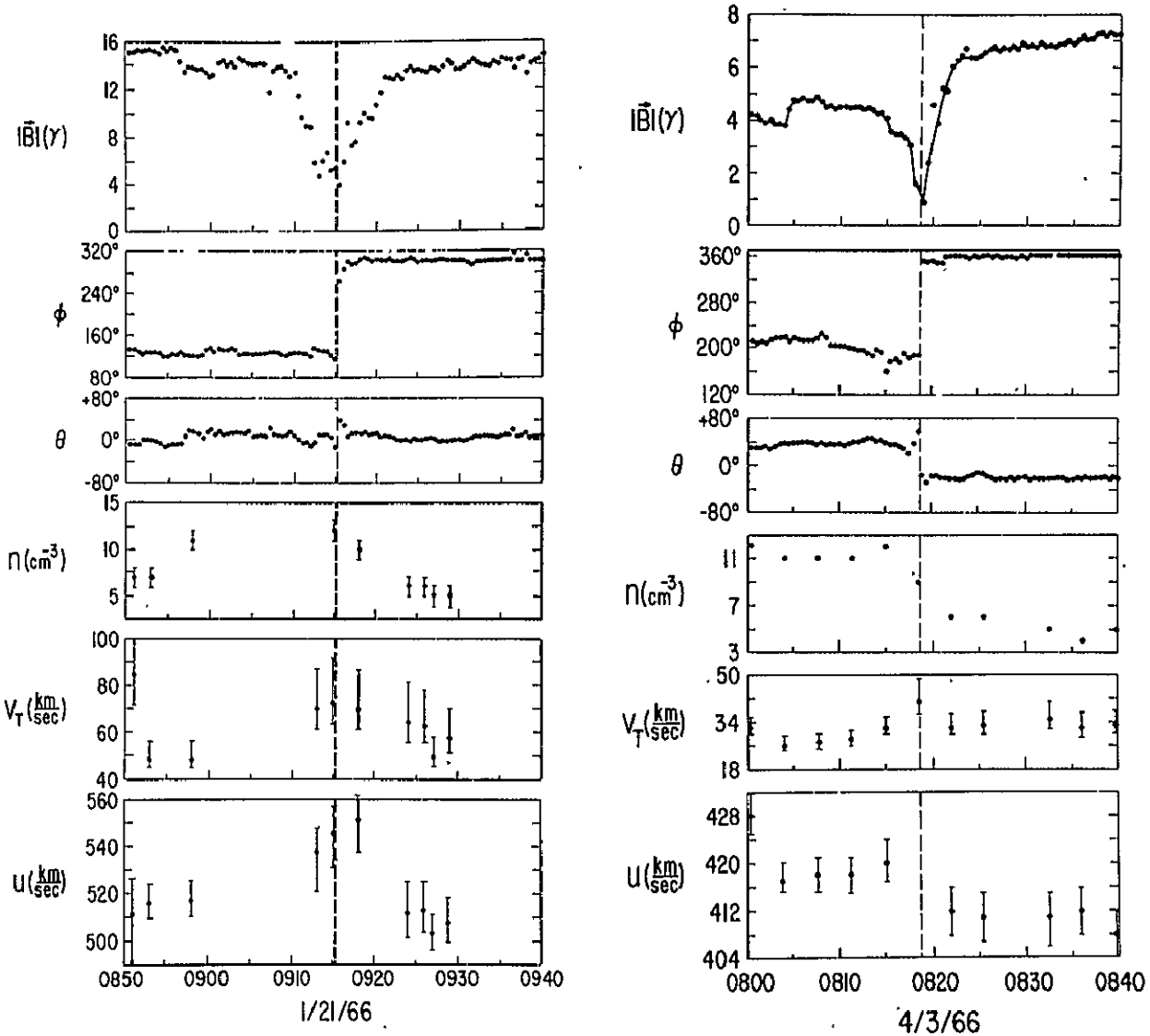

Figure 27. D sheets. In some instances the field appears to be annihilated at discontinuities as shown by the 2 cases in this Figure.

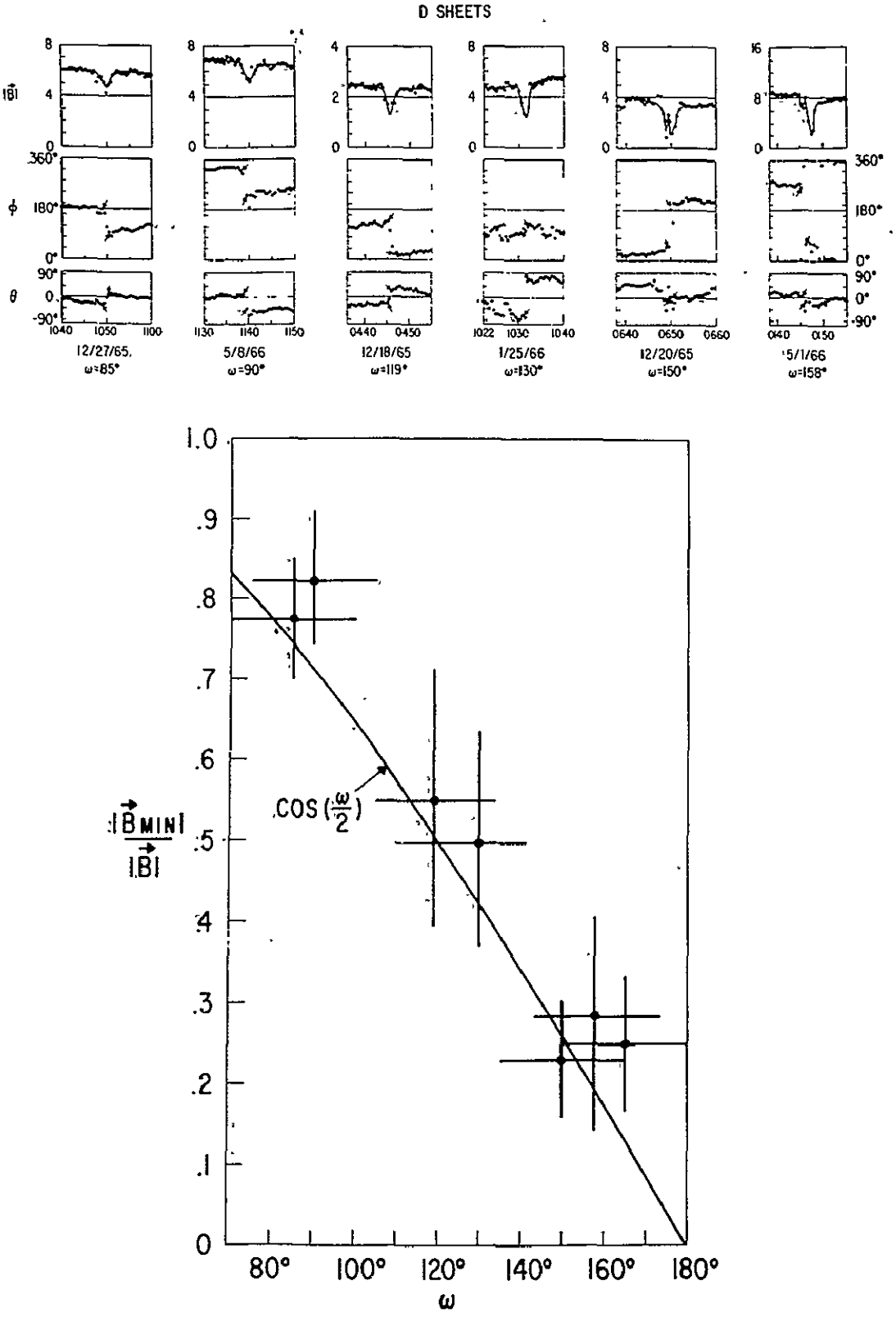

Figure 28. Annihilation at D sheets. The annihilation hypothesis implies that $B_{min}/B = \cos(\omega/2)$ where ω is the change in the field direction. This seems to be the case for the D sheets in the top of this figure.

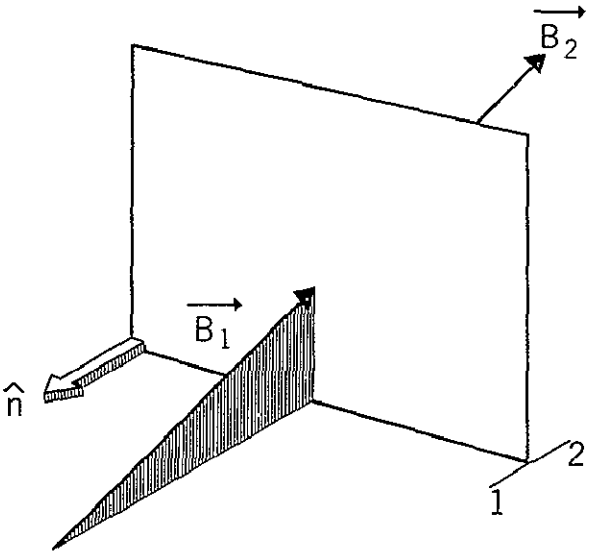

Figure 29. Contact discontinuity. Here $\underset{\sim}{B}_1 = \underset{\sim}{B}_2$, but $n_1 \neq n_2$ and $T_1 \neq T_3$.

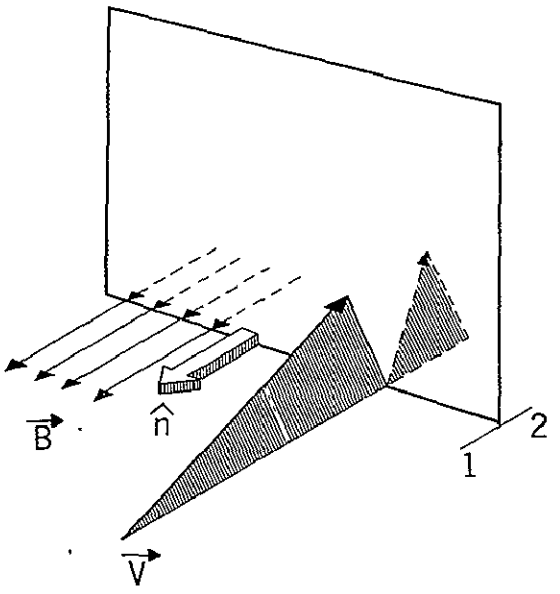

Figure 30. Parallel shock. $\underset{\sim}{B}$ is parallel to $\hat{n}$.

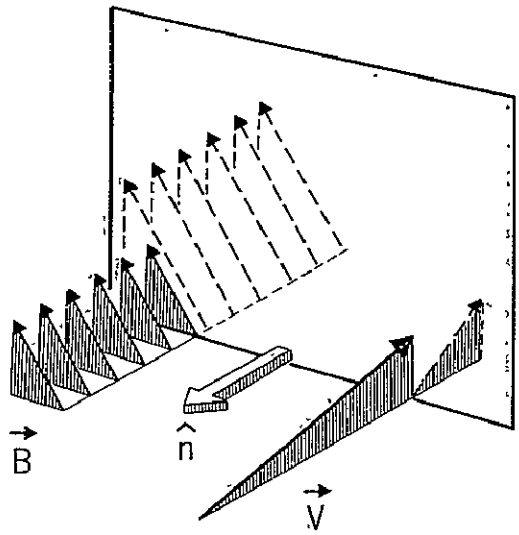

Figure 31. Perpendicular shock. $\underset{\sim}{B}$ is perpendicular to $\hat{n}$.

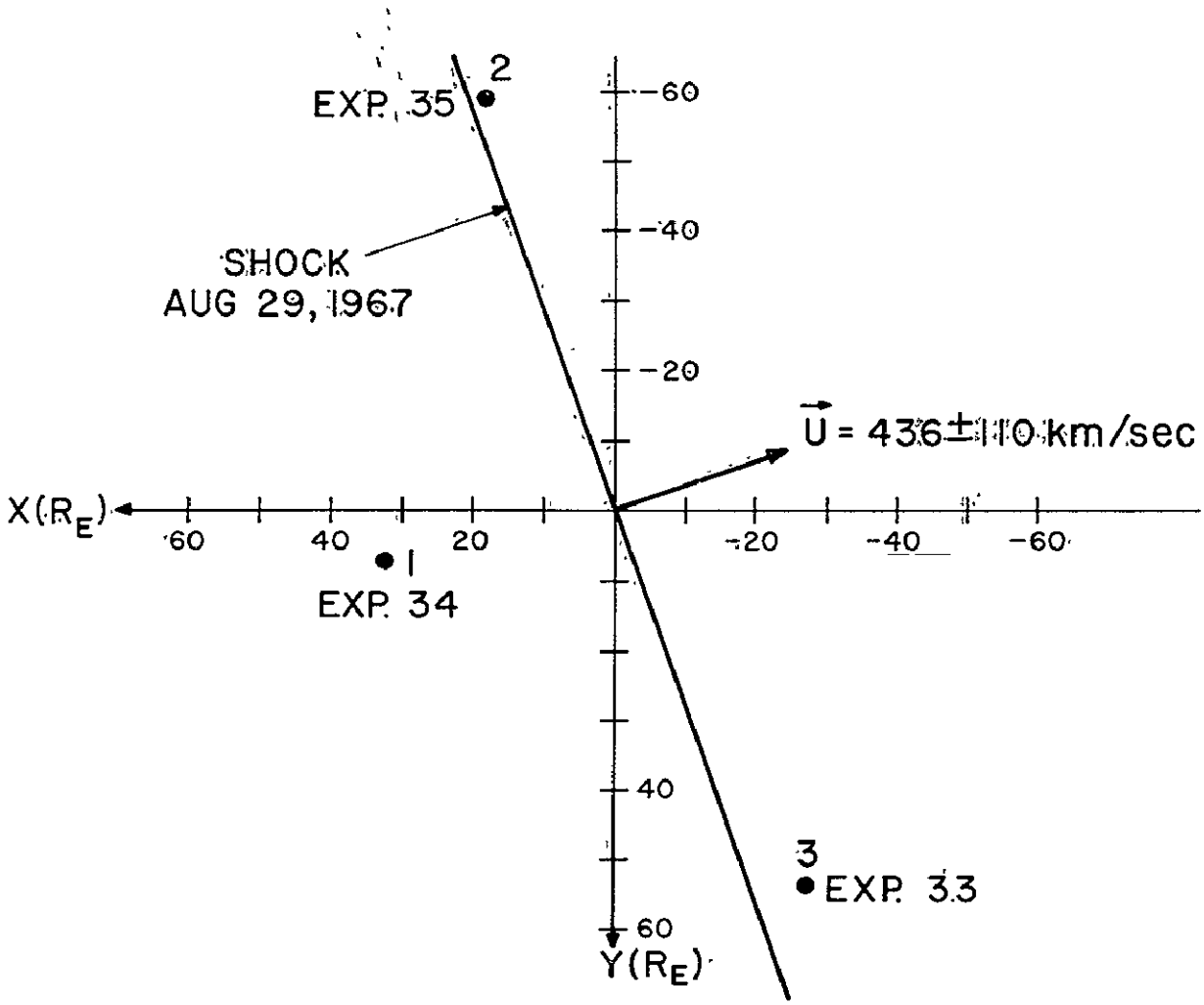

Figure 32. Observation of a perpendicular shock. The shock orientation and speed shown here were computed from the arrival times at the 3 spacecraft which are shown.

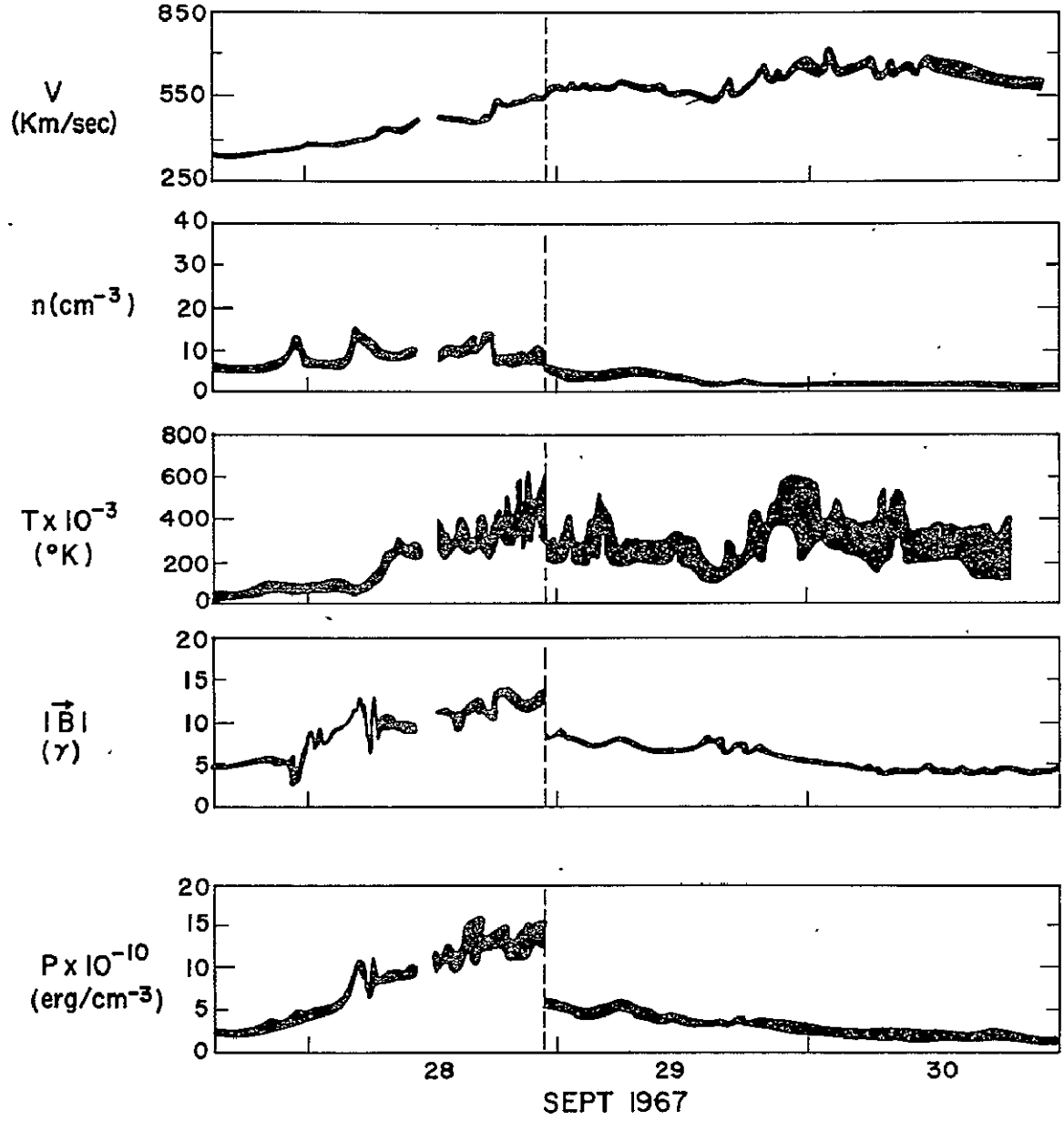

Figure 33. Observation of a reverse perpendicular shock. Note the signature and the change in the pressure across the shock.

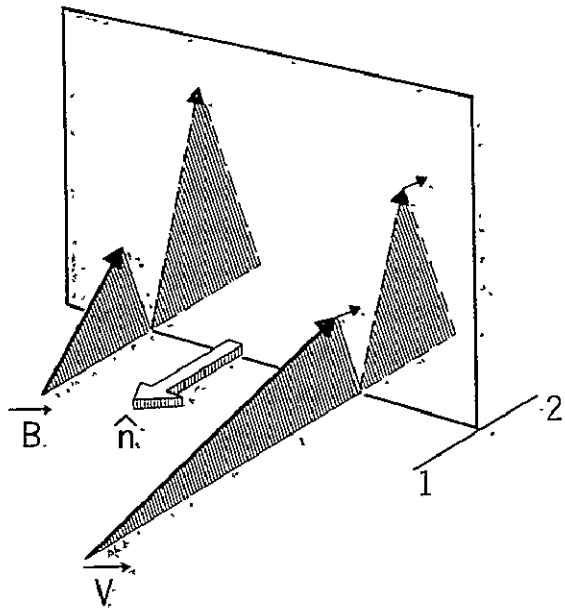

Figure 34. Fast Shock, A special case as shown for simplicity.

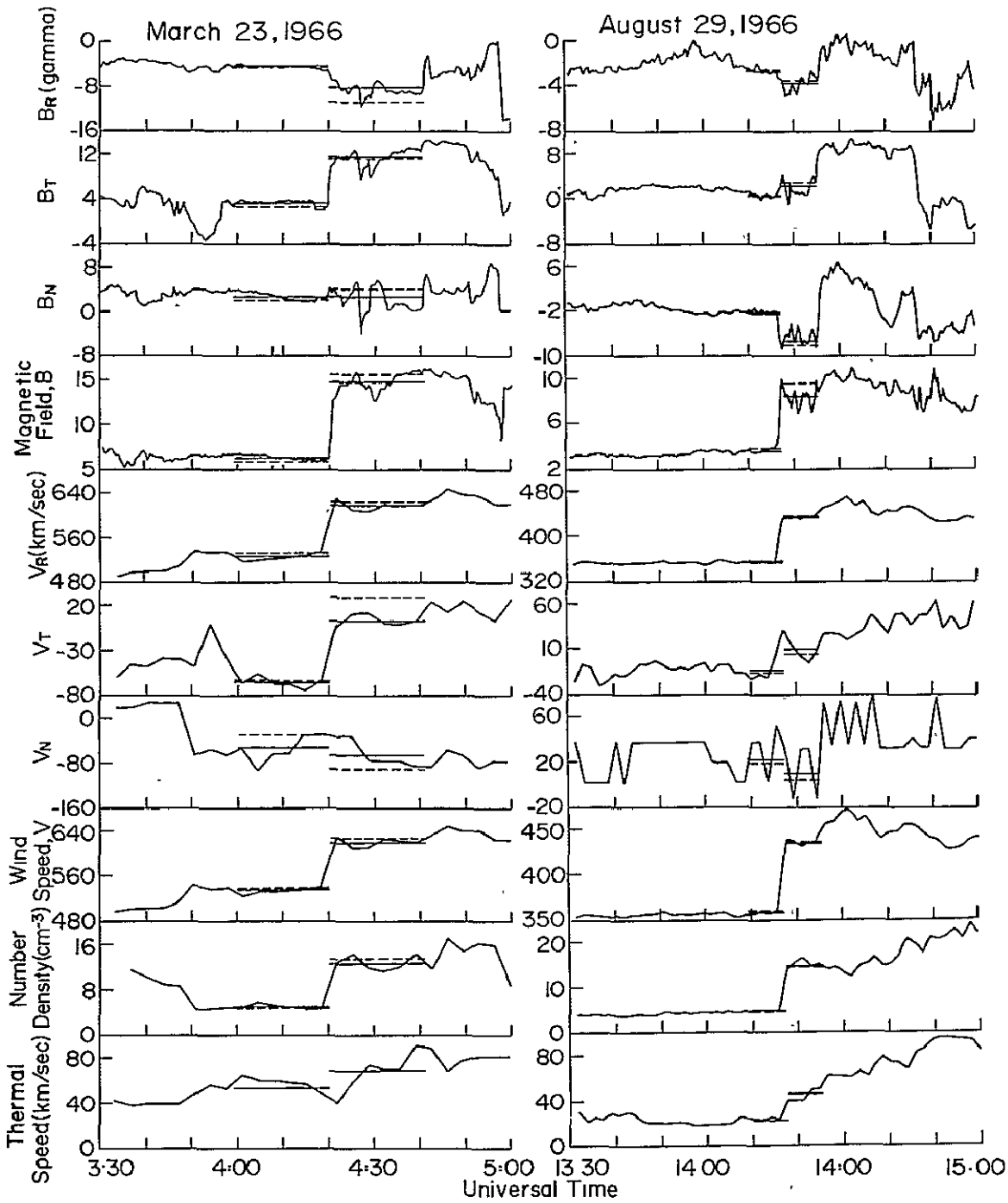

Figure 35. Observations of 2 fast shocks. The solid horizontal segments are are averages, the dashed segments are Chao's "best-fit" values.

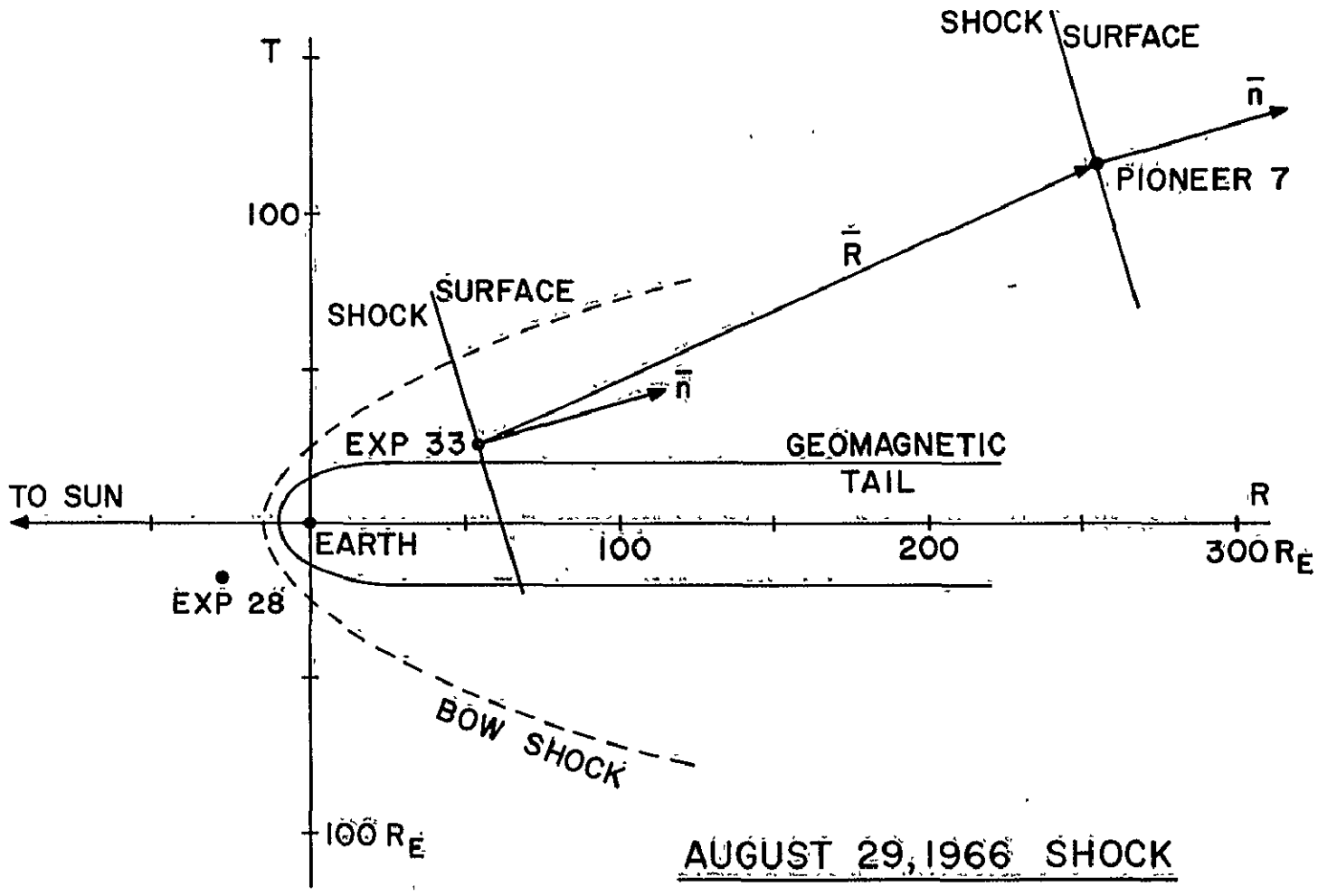

Figure 36. Observations of a fast shock by 2 spacecraft. The normals shown here were computed by Lepping and Argentiero.

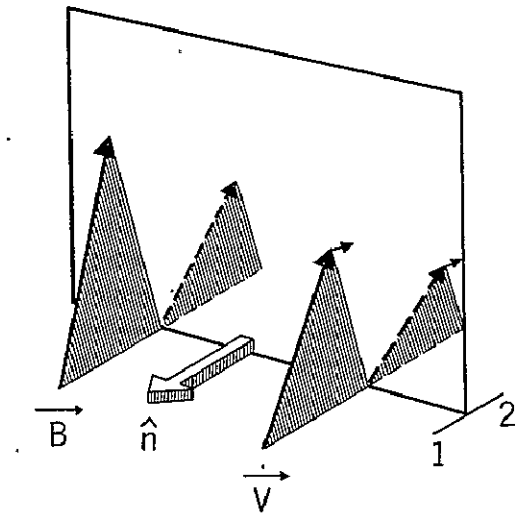

Figure 37. Slow shock. A special case is shown. In general one can add a component of V in the shock plane.

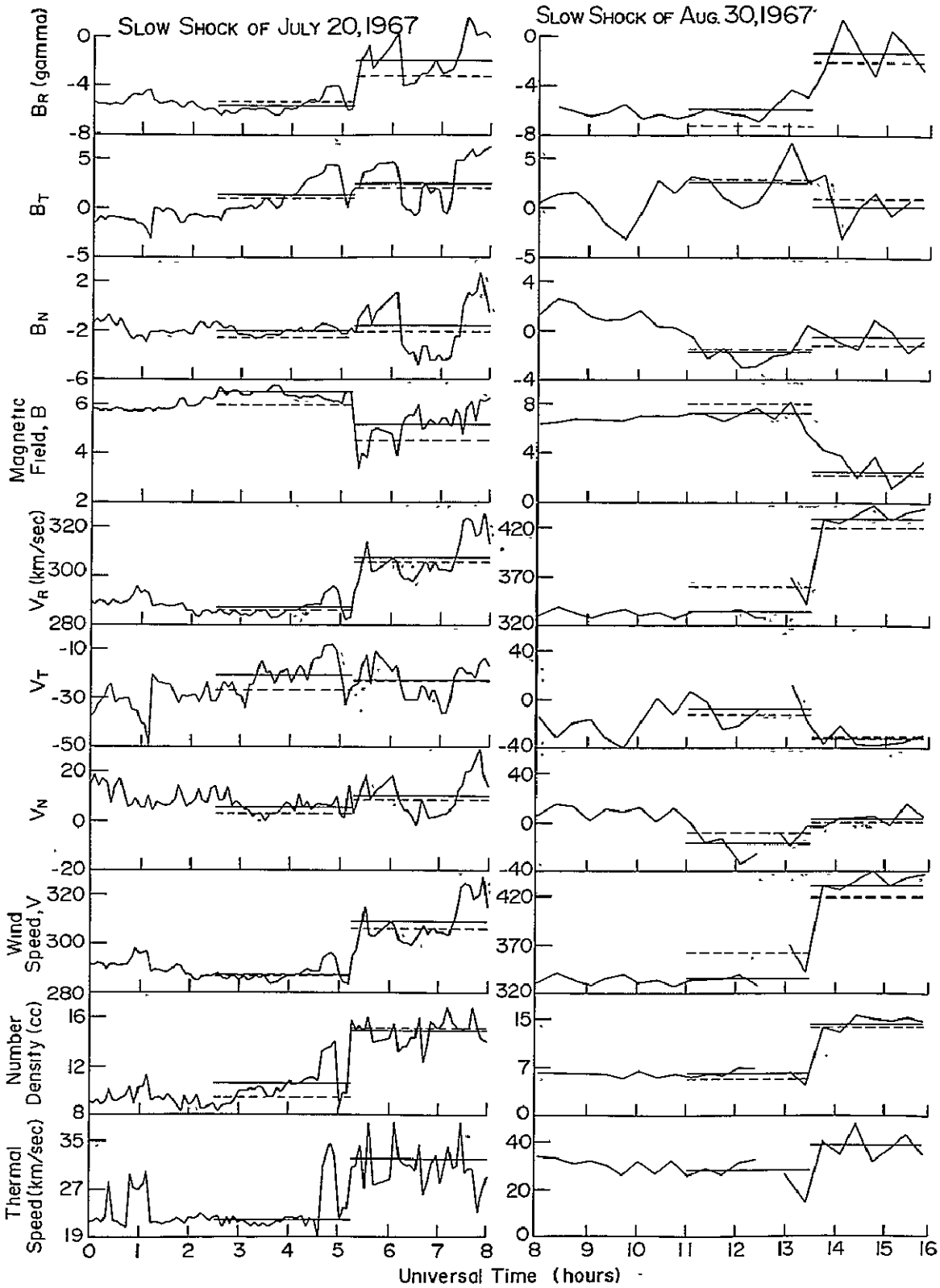

Figure 38. Observations of 2 slow shocks. Observed (solid lines) and calculated values (dashed lines) are in good agreement.

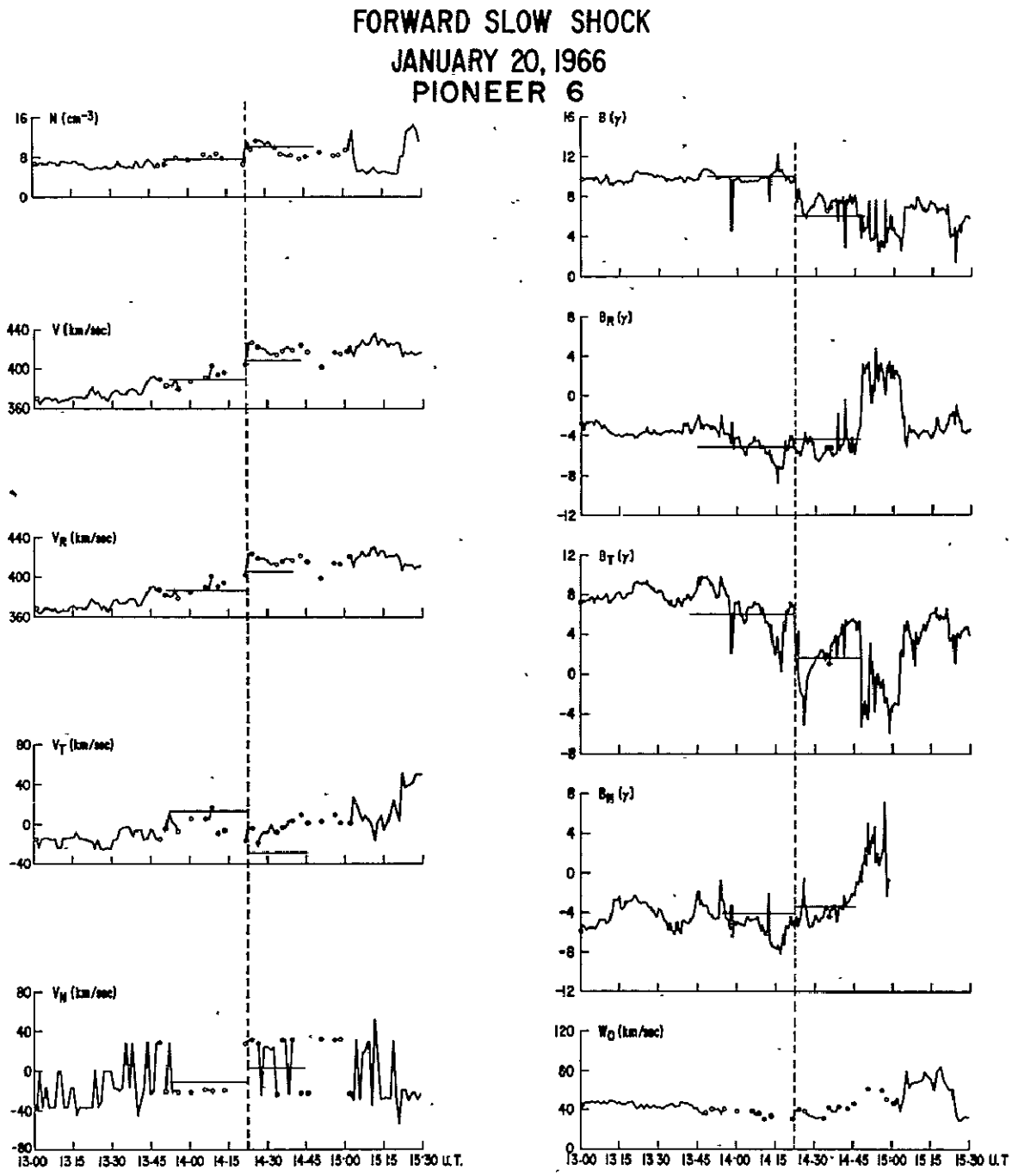

Figure 39. Observations of a forward slow shock.

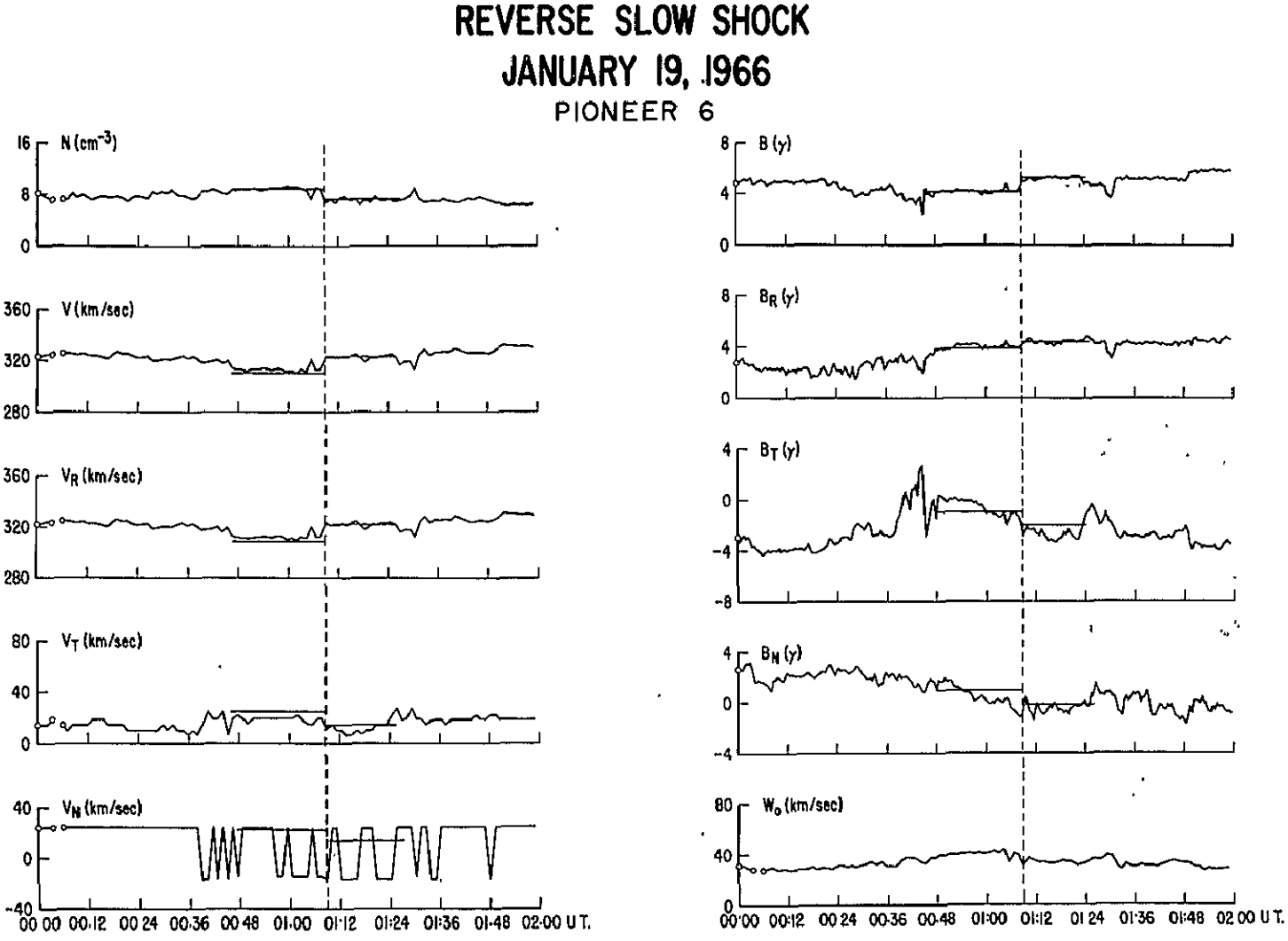

Figure 40. Observations of a reverse slow shock.

ALFVEN SHOCK
ROTATIONAL DISCONTINUITY

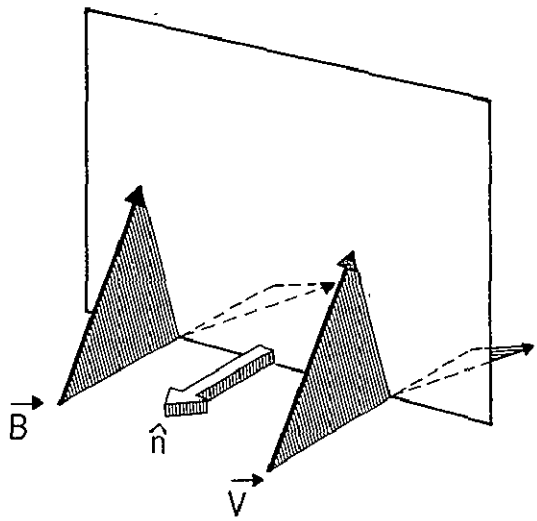

Figure 41. Alfven shock.

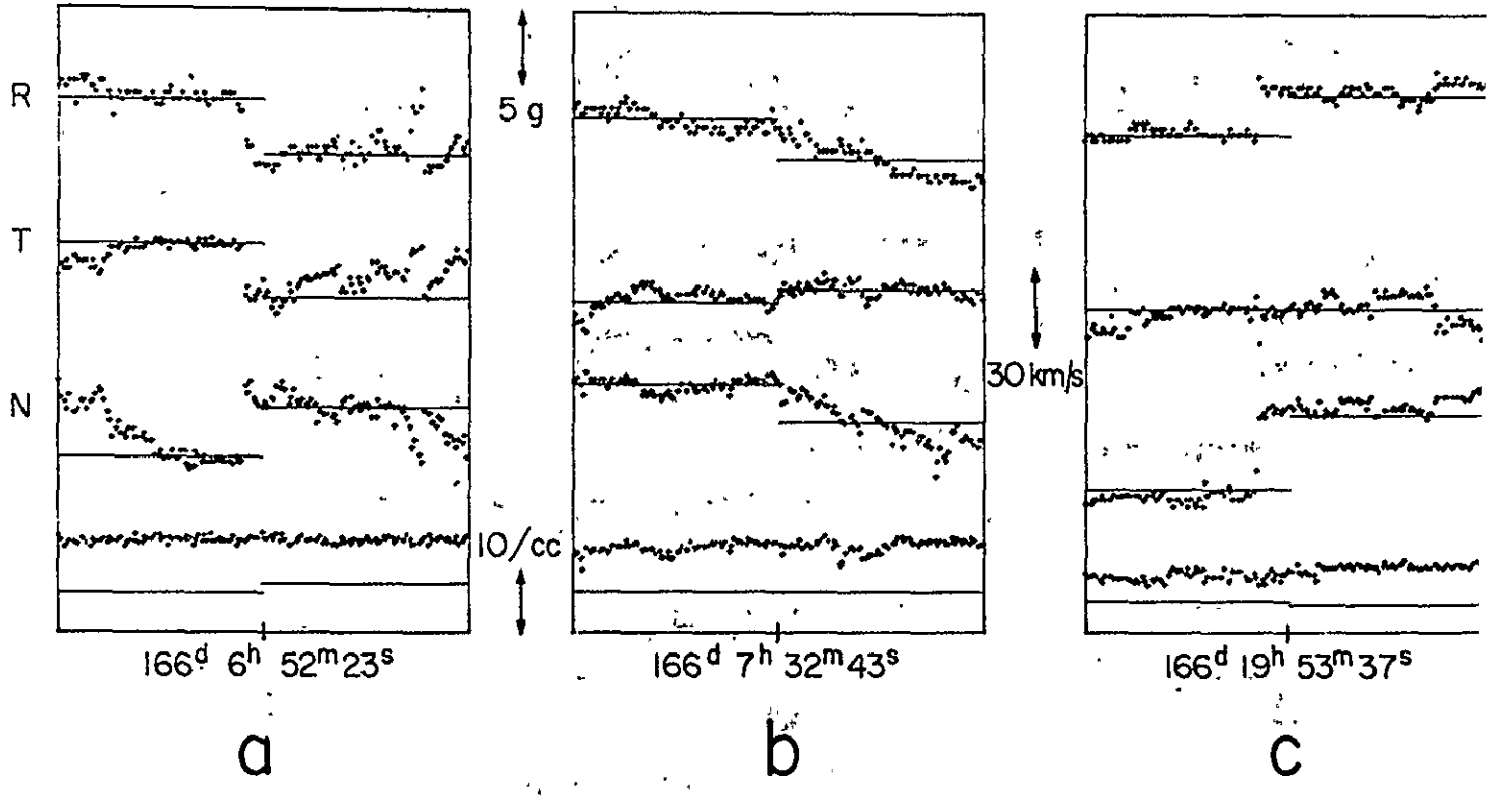

Figure 42. Observations of Alfven shocks.